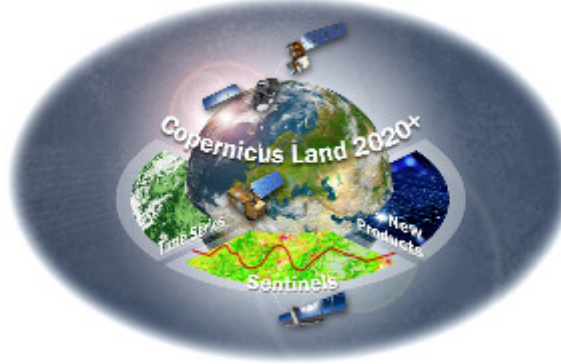

Horizon 2020

Space Call - Earth Observation: EO-3-2016: Evolution of Copernicus services
Grant Agreement No. 730008

ECoLaSS

Evolution of Copernicus Land Services based on Sentinel data



D7.1

"D32.1a – Methods Compendium: Time Series Preparation"

Issue/Rev.:1.0

Date Issued: 28.02.2018

submitted by:



in collaboration with the consortium partners:



submitted to:



European Commission – Research Executive Agency

This project has received funding from the European Union's Horizon 2020 Research and Innovation Programme, under Grant Agreement No. 730008

CONSORTIUM PARTNERS

No.	PARTICIPANT ORGANISATION NAME	SHORT NAME	CITY, COUNTRY
1	GAF AG	GAF	Munich, Germany
2	Systèmes d'Information à Référence Spatiale SAS	SIRS	Villeneuve d'Ascq, France
3	JOANNEUM RESEARCH Forschungsgesellschaft mbH	JR	Graz, Austria
4	Université catholique de Louvain, Earth and Life Institute (ELI)	UCL	Louvain-la-Neuve, Belgium
5	German Aerospace Center (DLR), German Remote Sensing Data Center (DFD), Wessling	DLR	Wessling, Germany

CONTACT:

GAF AG
Arnulfstr. 199 – D-80634 München – Germany
Phone: ++49 (0)89 121528 0 – FAX: ++49 (0)89 121528 79
E-mail: copernicus@gaf.de – Internet: www.gaf.de

DISCLAIMER:

The contents of this document are the copyright of GAF AG and Partners. It is released by GAF AG on the condition that it will not be copied in whole, in section or otherwise reproduced (whether by photographic, reprographic or any other method) and that the contents thereof shall not be divulged to any other person other than of the addressed (save to the other authorised officers of their organisation having a need to know such contents, for the purpose of which disclosure is made by GAF AG) without prior consent of GAF AG and Partners.

DOCUMENT RELEASE SHEET

	NAME, FUNCTION	DATE	SIGNATURE
Author(s):	Heinz Gallau (JR) Janik Deutscher (JR) Petra Miletich (JR) Klaus Granica (JR) Benedikt Zörfus (JR) Larissa Posch (JR) Annekatrin Metz-Marconcini (DLR) Igor Klein (DLR)	26/02/2018	
Review:	Petra Miletich (JR) Monika Kovatsch (GAF)	28/02/2018	
Approval:	Linda Moser (GAF)	28/02/2018	
Acceptance:			
Distribution:			

DISSEMINATION LEVEL

DISSEMINATION LEVEL			
PU	Public		X
CO	Confidential: only for members of the consortium (including the Commission Services)		

DOCUMENT STATUS SHEET

ISSUE/REV	DATE	PAGE(S)	DESCRIPTION / CHANGES
1.0	28.02.2018	65	First delivery of the Methods Compendium: Time Series Preparation

APPLICABLE DOCUMENTS

ID	DOCUMENT NAME / ISSUE DATE
AD01	Horizon 2020 Work Programme 2016 – 2017, 5 iii. Leadership in Enabling and Industrial Technologies – Space. Call: EO-3-2016: Evolution of Copernicus services. Issued: 13.10.2015
AD02	Guidance Document: Research Needs Of Copernicus Operational Services. Final Version issued: 30.10.2015
AD03	Proposal: Evolution of Copernicus Land Services based on Sentinel data. Proposal acronym: ECoLaSS, Proposal number: 730008. Submitted: 03.03.2016
AD04	Grant Agreement – ECoLaSS. Grant Agreement number: 730008 – ECoLaSS – H2020-EO-2016/H2020-EO-2016, Issued: 18.10.2016
AD05	D21.1a - Service Evolution Requirements Report, Issue 1.0, Issued: 09.08.2017
AD06	D4.1_D22.1a-EO_and_other_data_requirements_Report_Issue_1_M9

EXECUTIVE SUMMARY

The Horizon 2020 (H2020) project, “Evolution of Copernicus Land Services based on Sentinel data” (ECoLaSS) addresses the H2020 Work Programme 5 iii. Leadership in Enabling and Industrial technologies - Space, specifically the Topic EO-3-2016: Evolution of Copernicus services. ECoLaSS will be conducted from 2017–2019 and aims at developing and prototypically demonstrating selected innovative products and methods for future next-generation operational Copernicus Land Monitoring Service (CLMS) products of the pan-European and Global Components. This will contribute to demonstrating the operational readiness of the finally selected products, and shall allow the key CLMS stakeholders (i.e. mainly the Entrusted European Entities (EEE) EEA and JRC) to make informed decisions on potential procurement of the next generation of Copernicus Land services from 2020 onwards.

To achieve this goal, ECoLaSS will make full use of dense time series of Sentinel-2 and Sentinel-3 optical data as well as Sentinel-1 Synthetic Aperture Radar (SAR) data. Rapidly evolving scientific as well as user requirements will be analysed in support of a future pan-European roll-out of new/improved CLMS products, and the transfer to global applications.

The Deliverable “D32.1a – Methods Compendium: Time Series Preparation” analyses methods for fully automated pre-processing of Sentinel time series data streams, which are a prerequisite for all further processing tasks. The quality of the pre-processing procedure determines the thematic quality, content, and accuracy that can be achieved in any subsequent information extraction processes. In phase 1 the work of WP32 is focused on time series preparation of Sentinel-1 and Sentinel-2 data for the defined test sites. The focus of WP32 are comprehensive tests of optical as well as SAR pre-processing methods and the implementation of pre-operational processing lines which allow pre-processing of Sentinel-1 and Sentinel-2 data streams following the requirements as requested in AD06. The thematic focus of WP32 is the testing and benchmarking of existing pre-processing methods for a) atmospheric correction, b) cloud, shadow and snow masking, c) topographic normalisation and d) the geometric consistency of the products with regards to Sentinel-2 data. Furthermore, testing and benchmarking of existing pre-processing methods for Sentinel-1 data will be performed focusing on a) radiometric calibration, b) speckle noise reduction and d) interferometric coherence estimation.

However, it is expected that existing pre-processing software packages will be significantly improved in the near future, e.g. it is expected that the atmospheric correction software Sen2Cor will be further developed and improved. In phase 2 of ECoLaSS it is planned to apply the implemented processing on the demo sites. Furthermore, the fusion of Sentinel-2 and Sentinel-3 time-series will be addressed in phase 2, as in addition to the Sentinel-3A also the Sentinel-3B satellite imagery will be available which leads to the required temporal density of the Sentinel-3 time-series.

Table of Contents

1	INTRODUCTION.....	1
2	TEST SITES	2
3	STATE-OF-THE-ART.....	4
3.1	PROCESSING METHODS FOR OPTICAL TIME SERIES	4
3.1.1	<i>Atmospheric correction.....</i>	4
3.1.2	<i>Cloud, Cloud Shadow and Snow Masking.....</i>	7
3.1.3	<i>Topographic normalisation.....</i>	9
3.1.4	<i>Sentinel-2/Sentinel-3 time series fusion</i>	11
3.2	PROCESSING METHODS FOR SAR TIME SERIES.....	11
3.2.1	<i>Geometric pre-processing.....</i>	11
3.2.2	<i>Radiometric pre-processing</i>	12
3.2.3	<i>Coherence estimation.....</i>	14
3.2.4	<i>Available SAR processing software tools</i>	16
4	TESTING AND BENCHMARKING OF CANDIDATE METHODS	18
4.1	BENCHMARKING OF METHODS FOR PRE-PROCESSING OF OPTICAL TIME SERIES.....	18
4.1.1	<i>Benchmarking of candidate approaches for atmospheric correction.....</i>	18
4.1.1.1	Description of Candidate Methods	18
4.1.1.2	Benchmarking Criteria.....	19
4.1.1.3	Implementation and Results of Benchmarking	19
4.1.1.4	Summary and Conclusions	23
4.1.2	<i>Benchmarking of candidate approaches for cloud, cloud shadow and snow masking</i>	23
4.1.2.1	Description of Candidate Methods	23
4.1.2.2	Benchmarking Criteria.....	25
4.1.2.3	Implementation and Results of Benchmarking	25
4.1.2.4	Summary and Conclusions	32
4.1.3	<i>Benchmarking of candidate approaches for topographic normalisation</i>	32
4.1.3.1	Description of Candidate Methods	32
4.1.3.2	Benchmarking Criteria.....	33
4.1.3.3	Implementation and Results of Benchmarking	33
4.1.3.4	Summary and Conclusions	38
4.1.4	<i>Benchmarking of candidate approaches for Geometric consistency.....</i>	39
4.1.4.1	Description of Candidate Methods	39
4.1.4.2	Benchmarking Criteria.....	39
4.1.4.3	Implementation and Results of Benchmarking	40
4.1.4.4	Summary and Conclusions	42
4.2	BENCHMARKING OF METHODS FOR PRE-PROCESSING OF SAR TIME SERIES.....	43
4.2.1	<i>Benchmarking of candidate approaches for radiometric calibration.....</i>	43
4.2.1.1	Description of Candidate Methods	43
4.2.1.2	Benchmarking Criteria.....	43
4.2.1.3	Implementation and Results of Benchmarking	44
4.2.1.4	Summary and Conclusions	44
4.2.2	<i>Benchmarking of candidate approaches for speckle noise reduction.....</i>	44
4.2.2.1	Description of Candidate Methods	45
4.2.2.2	Benchmarking Criteria.....	45
4.2.2.3	Implementation and Results of Benchmarking	45
4.2.2.4	Summary and Conclusions	50
4.2.3	<i>Benchmarking of candidate approaches for interferometric coherence estimation.....</i>	50
4.2.3.1	Description of Candidate Methods	50
4.2.3.2	Benchmarking Criteria.....	51
4.2.3.3	Implementation and Results of Benchmarking	51
4.2.3.4	Summary and Conclusions	53
5	PRE-PROCESSING OF ECOLASS TEST SITES	54
5.1	PRE-PROCESSING OF OPTICAL DATA	54
5.2	PRE-PROCESSING OF SAR DATA	57

6 CONCLUSIONS AND OUTLOOK	60
REFERENCES.....	62

List of Figures and Tables

FIGURE 2-1: DEMONSTRATION SITES WHICH ARE PROCESSED IN TASK 4 ARE DRAWN IN BLACK, TEST SITES WHICH ARE PROCESSED IN TASK 3 ARE DRAWN IN RED.	2
FIGURE 2-2: SOUTH AFRICA	3
FIGURE 2-3: MALI.....	3
FIGURE 3-1: THEIA LEVEL-2 DATA PRODUCTION EXTENT. (17.01.2017) SOURCE: HTTP://WWW.CESBIO.UPS-TLSE.FR/MULTITEMP/?PAGE_ID=7501	9
FIGURE 3-2: LAND COVER CLASSIFICATION ACCURACIES FOR DB AND DN AND DIFFERENT PRE-PROCESSING SCENARIOS.....	12
FIGURE 3-3: DIFFERENT SAR RADIOMETRIC PROCESSING LEVELS: LEFT: BETA NAUGHT (SLANT RANGE GEOMETRY), MIDDLE: SIGMA NAUGHT (CORRECTED FOR LOCAL INCIDENCE ANGLE), RIGHT: FLATTENED GAMMA NAUGHT (TERRAIN CORRECTIONS ACCORDING TO SMALL, 2011).	13
FIGURE 3-4: EXAMPLE OF TWO SAR SPECKLE FILTERS APPLIED AT AN URBAN/RURAL TEST SITE	14
FIGURE 3-5: COMPARISON BETWEEN THREE DIFFERENT FULL RESOLUTION COHERENCE ESTIMATES OF THE SAME INTERFEROGRAM, (20090618-20090629): (A) A 5×5 WINDOW BOXCAR, (B) 11×11 WINDOW BOXCAR, AND (C) SIBLING-BASED (25 TO 100 SIBLINGS PER POINT) 41×41 SEARCH WINDOW). THE BOXCAR COHERENCE ESTIMATES MANY FALSE HIGH COHERENCE POINTS, SUCH AS IN THE FIELD OUTLINED IN RED. SOURCE: SPAANS AND HOOOPER, 2016.	15
FIGURE 4-1: COMPARISON BETWEEN THE MSI, MODIS AND OLI SENSORS. BASED ON: U.S. GEOLOGICAL SURVEY (2016), SUHET (2015), AND NASA OFFICIAL.....	21
FIGURE 4-2: MEAN REFLECTANCE - RED BAND	22
FIGURE 4-3: MEAN REFLECTANCE - NIR BAND	22
FIGURE 4-4: MEAN REFLECTANCE - SWIR BANDS.....	22
FIGURE 4-5: SEN2COR CLOUD MASK: COMPARISON BETWEEN LEVEL-1C AND LEVEL-2A PRODUCT	26
FIGURE 4-6: MAJA CLOUD MASK. SENTINEL-2_20170705T105031_31UER; 49°41'8.69"N; 4°16'55.80"E	27
FIGURE 4-7: DIFFERENCES BETWEEN THE MAJA CLOUD MASK (LEFT) AND THE SEN2COR CLOUD MASK (RIGHT).	28
FIGURE 4-8: EXAMPLE 1: CLOUD MASK COMPARISON BETWEEN MAJA AND SEN2COR. SENTINEL-2_20170725T105031_31UER; 49°41'8.69"N; 4°16'55.80"E	29
FIGURE 4-9: EXAMPLE 2: CLOUD MASKS COMPARISON BETWEEN MAJA AND SEN2COR. SENTINEL-2_20170705T105031_31UER; 49°41'8.69"N; 4°16'55.80"E	30
FIGURE 4-10: SHADOW MASK: COMPARISON BETWEEN TERRAIN AND CLOUD SHADOWS.....	31
FIGURE 4-11: EXAMPLE SHOWING THE VARIOUS IMAGES BEFORE AND AFTER TOPOGRAPHIC NORMALISATION (SEE ALSO TABLE 1).	35
FIGURE 4-12: EXAMPLE SHOWING THE REGRESSION LINE BEFORE AND AFTER TOPOGRAPHIC NORMALISATION (ON TOP 2 BEFORE AND BELOW DIAGRAM AFTER CORRECTION).	36
FIGURE 4-13: REGRESSION LINES AFTER TOPOGRAPHIC NORMALISATION USING DIFFERENT SOFTWARE PACKAGES AND DEMS.....	37
FIGURE 4-14: BAR DIAGRAMS SHOWING THE SLOPE (BETA1) OF THE REGRESSION LINE.	37
FIGURE 4-15: BAR DIAGRAMS SHOWING THE CORRELATION BETWEEN $\cos(\theta)$ AND REFLECTANCE.	38
FIGURE 4-16: GEOMETRIC ACCURACY ANALYSIS FOR SENTINEL-2 DATA AT A FLAT TERRAIN TEST SITE	40
FIGURE 4-17: GEOMETRIC ACCURACY ANALYSIS FOR SENTINEL-2 DATA AT A MOUNTAINOUS TEST SITE.....	41
FIGURE 4-18: TWO SENTINEL-2 IMAGES FROM THE MOUNTAINOUS TEST AREA AND DISPARITY IMAGES IN EAST AND NORTH BETWEEN BOTH IMAGES.....	42
FIGURE 4-19: DIFFERENT SAR RADIOMETRIC PROCESSING LEVELS: LEFT: BETA NAUGHT (SLANT RANGE GEOMETRY), MIDDLE: SIGMA NAUGHT (CORRECTED FOR LOCAL INCIDENCE ANGLE), RIGHT: FLATTENED GAMMA NAUGHT (TERRAIN CORRECTIONS ACCORDING TO SMALL, 2011).	44
FIGURE 4-20: EXAMPLES OF DIFFERENT ADAPTIVE SAR SPECKLE FILTERS	46
FIGURE 4-21: EXAMPLES OF DIFFERENT ADAPTIVE SAR SPECKLE FILTERS.	47
FIGURE 4-22: FROST FILTER WITH DIFFERENT FILTER WINDOWS.....	47
FIGURE 4-23: LAND COVER CLASSIFICATION ACCURACIES ACHIEVED WITH DIFFERENT ADAPTIVE SAR SPECKLE FILTERS.	48
FIGURE 4-24: CROSS-VALIDATION ACCURACIES FOR LAND COVER CLASSIFICATION ACHIEVED WITH DIFFERENT ADAPTIVE SAR SPECKLE FILTERS AND WINDOW SIZES.....	49
FIGURE 4-25: MEAN CROSS-VALIDATION ACCURACIES ACHIEVED WITH DIFFERENT SAR SPECKLE FILTERS, WINDOW SIZES, PROCESSING UNITS AND SPATIAL RESOLUTIONS.	49

FIGURE 4-26: LEFT: SINGLE SENTINEL-1 SCENE, UNFILTERED; RIGHT: SINGLE SENTINEL-1 SCENE FILTERED WITH MTF, 19 IMAGES, 7x7 WINDOW.....	50
FIGURE 4-27: CALCULATION OF ORTHOGONAL BASELINES FOR 6-DAY COHERENCE PAIRS (LEFT) AND FOR ALL COMMON-MASTER PAIRS (RIGHT) FOR BELGIUM TEST SITE	51
FIGURE 4-28: COHERENCE PRODUCT EXAMPLES FROM THE BELGIUM AND CENTRAL TEST SITE.....	52
FIGURE 4-29: EXAMPLES FOR VH COHERENCE DECORRELATION OVER TIME, CENTRAL TEST SITE; STACK: MARCH – JUNE 2017 (MASTER 28.04.2017).....	53
FIGURE 5-1: PRE-PROCESSING OF OPTICAL TIME SERIES - WORKFLOW.....	54
FIGURE 5-2: SENTINEL-1 PRE-PROCESSING WORKFLOW IN ECOLASS	58

TABLE 2-1: TEST SITES AND CORRESPONDING DEMO SITES	2
TABLE 4-1: CORRESPONDING BANDS REGARDING EACH SPECTRAL REGION ACROSS MSI, OLI AND MODIS.....	20
TABLE 4-2: OVERVIEW OF THE USED COMBINATIONS.....	34
TABLE 4-3: OVERVIEW OF THE USED CLASSES AND NUMBER OF SAMPLES/PIXELS.....	34
TABLE 5-1: FILE SUFFIX FOR PROCESSED PRODUCTS.....	55
TABLE 5-2: NAMING CONVENTION SENTINEL-2 IN PHASE 1.....	55
TABLE 5-3: BAND ORDER FOR ECOLASS SENTINEL-2 DATA	56
TABLE 5-4: TEST SITES – RESULTING SENTINEL-2 TIME SERIES IMAGERY.....	57
TABLE 5-5: TEST SITES – RESULTING SENTINEL-1 TIME SERIES IMAGERY.....	59

Abbreviations

ACCA	Automated-Cloud-Cover Assessment
ACIX	Atmospheric Correction Inter-comparison eXercise
AERONET	AErosol RObotic NETwork
ALE	Absolute Location Error
AOI	Area Of Interest
AOT	Aerosol Optical Thickness
APDA	Atmospheric Pre-corrected Differential Absorption
ATCOR	ATmospheric CORrection
BOA	Bottom-of-Atmosphere
BT	Brightness temperature
CADS	Calibration Annotation Data Set
CESBIO	Centre d'Etudes Spatiales de la BIOsphère
CGIAR-CSI	Consortium for Spatial Information
CLMS	Copernicus Land Monitoring Services
CNES	Centre national d'études spatiales
db	Decibel
DDV	Dark Dense Vegetation
DEM	Digital Elevation Model
DLR	Deutschen Zentrums für Luft- und Raumfahrt
DN	Digital Number
DORIS	Delft Object-Oriented Radar Interferometric software
DSM	Digital Surface Model
DU	Dobson Unit
ECoLaSS	Evolution of Copernicus Land Services based on Sentinel data
EEA	European Environment Agency
EEE	Entrusted European Entities
EO	Earth Observation
ERS	European Remote-Sensing Satellite
ESA	European Space Agency
ETM+	Enhanced Thematic Mapper Plus
EW	Extra-Wide Swath Mode
Fmask	Function of mask
FR	Full Resolution
GeoTIFF	Georeferenced Tagged Image File Format
GMES	Global Monitoring for Environment and Security
GMT(s)	Generic Mapping Tool(s)
GRD	Ground Range Detected
GUI	Graphical User Interface
HH	Horizontal transmit/Horizontal receive (polarization)
HR	High Resolution
HRL	High Resolution Layer
HV	Horizontal transmit/Vertical receive (polarization)
InSAR	Interferometric Synthetic Aperture Radar
INSPIRE	Infrastructure for Spatial Information in Europe
IW	Interferometric Wide Swath Mode
JM	Jeffries Matusita
JRC	Joint Research Centre
KML	Keyhole Markup Language
LC	Land Cover
LibRadtran	Library For Radiative Transfer

LIDAR	Light Detection And Ranging
LUTs	Look Up Tables
MACCS	Multi-sensor Atmospheric Correction and Cloud Screening
MAJA	Maccs-Atcor Joint Algorithm
MODIS	Moderate Resolution Imaging Spectroradiometer
MODTRAN	MODerate resolution atmospheric TRANSmision
MR	Medium Resolution
MSI	MultiSpectral Instrument
MTF	Modulation Transfer Function
NASA	National Aeronautics and Space Administration
NDSI	Normalized Difference Snow Index
NDVI	Normalized Difference Vegetation Index
NIR	Near-InfraRed
OLI	Operational Land Imager
QI	Quality Indicators
RSG	Remote Sensing Software Graz
SLC	Single Look Complex
SAR	Synthetic Aperture Radar
SCM	Scene Classification Map
SM	Strip Map Mode
SMAC	Simplified Method for Atmospheric Correction
SNAP	Sentinel Application Platform
SRTM	Shuttle Radar Topography Mission
SSA	Single Scattering Albedo
SWIR	Short Wavelength Infrared
TM	Thematic Mapper
TOA	Top-of-Atmosphere
URL	Uniform Resource Locator
VH	Vertical transmit/Horizontal receive (polarization)
VNIR	Visible and Near InfraRed
VV	Vertical transmit/Vertical receive (polarization)
WP	Work Package
WV	Wave

1 Introduction

The aim of WP32 – Time Series Preparation is to find robust methods for fully automated pre-processing of Sentinel time series data streams, which are a prerequisite for all further processing tasks. The quality of the pre-processing procedure determines the thematic quality, content and accuracy that can be achieved in any subsequent information extraction processes. It has to be considered to process the best possible data products in order to fulfil highest quality standards.

The generation of spatio-temporally consistent optical time series with top of atmosphere reflectance values requires substantial fully automated pre-processing including a) extraction of metadata, b) optional - atmospheric correction, c) optional - topographic normalisation, d) cloud, cloud shadow and snow masking, e) radiometric calibration, f) derivation of indices and variables, g) generation of metadata according INSPIRE directives and h) generation of quality control reports. Considering the data size and number of scenes to be processed, an automated and rapid processing chain is essential, especially for near real-time scenarios. The research related to optical time series pre-processing is therefore focusing on testing of best suited algorithms and their application in test sites and the development of new methods as well as the implementation of prototype methods for a) cloud, cloud shadow and snow masking by integrating information over time b) spatio-temporal noise reduction and gap-filling of optical time series and c) fusion of Sentinel-2/Sentinel-3 time series.

Time series analysis based of SAR data can be based on backscatter or coherence products or a combination of these. All radar data require substantial pre-processing including a) automated SAR image download, b) automated preparation of digital elevation data, c) automated update of orbit files (PRECISE; RESTITUTED for near real time processing), d) thermal noise removal (for SLC) and GRD border noise removal, e) radiometric calibration, f) multi-looking and image filtering (speckle, adaptive), g) spatio-temporal speckle filtering (compare e.g. Quegan et al., 2000), h) radiometric terrain corrections (compare e.g. Small, 2011) and i) geo-referencing. Considering the number of scenes to be processed and the resulting data size, an automated and rapid processing chain is essential, especially for near real-time scenarios. The research related to SAR time series pre-processing is, therefore, focusing on a) benchmarking of existing / currently developed algorithms and tools, b) implementation of spatio-temporal noise filtering tools optimized for Sentinel-1 time series, c) enhanced automated detection and correction of atmospheric influences, d) cluster processing to reduce processing time, e) and derivation of multi-temporal metrics.

2 Test sites

In order to conduct an in-depth analysis five test sites within different major European environmental zones and two test sites in Africa have been chosen. Pre-processing of optical and SAR time series for all test sites, as mentioned in Table 2-1 has been performed to test and identify the best suited algorithms, to develop new methods and implement prototype processing software.

Table 2-1: Test sites and corresponding demo sites

Test sites	Demo sites	Defined test site granules	Biogeographic regions
European			
Sweden	North	33VVF_33VWF	Boreal
Austria/Germany	Central	32TPT_32UPU	Alpine/Continental
Greece/Bulgaria	South-East	34TGM_35TKG	Mediterranean /Alpine/Continental
Belgium	West	31UFR_31UFS, 31UES_31UER	Atlantic/Continental
France	South-West	30TYP_31TCJ	Atlantic
African			
Mali	Mali	29PRP_30PTU	
South Africa	South Africa	35JMJ_35JNJ	

Figure 2-1 shows the five European test sites with their corresponding demonstration sites. Each demo site contains a representative test site of two granules for software and algorithm testing and development. The location of these test sites within the demonstration sites is highlighted in red colour.

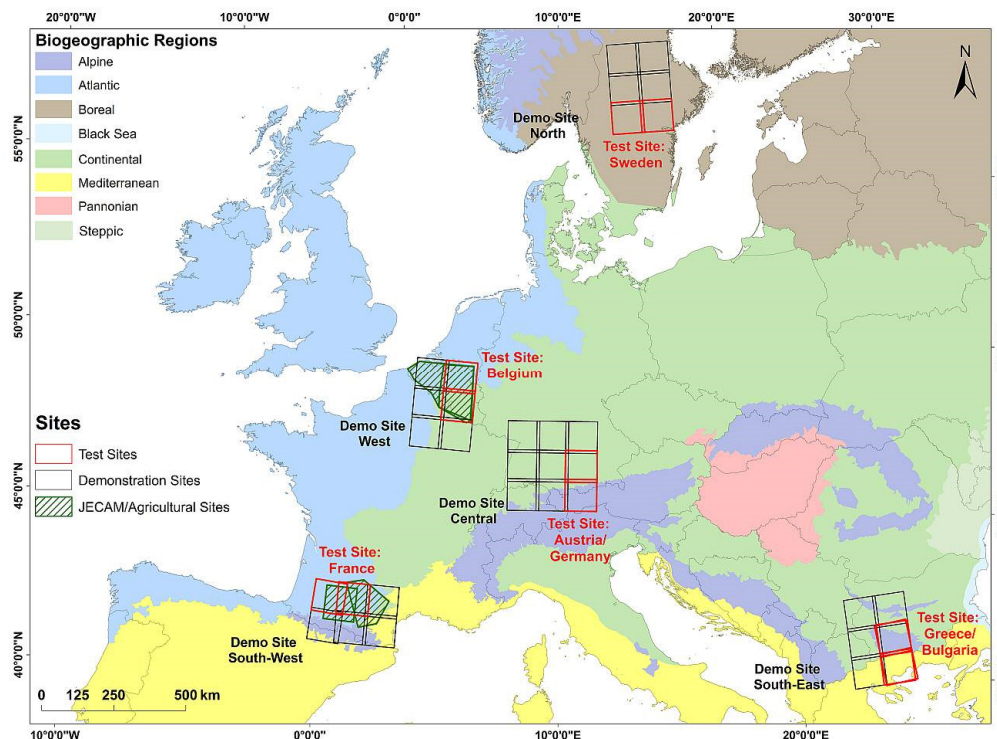


Figure 2-1: Demonstration sites which are processed in task 4 are drawn in black, test sites which are processed in task 3 are drawn in red.

The test sites in South Africa as well as in Mali are shown in Figure 2-2 and Figure 2-3, respectively.

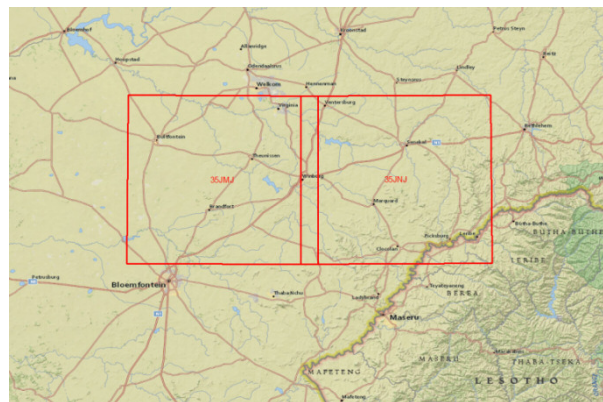


Figure 2-2: South Africa

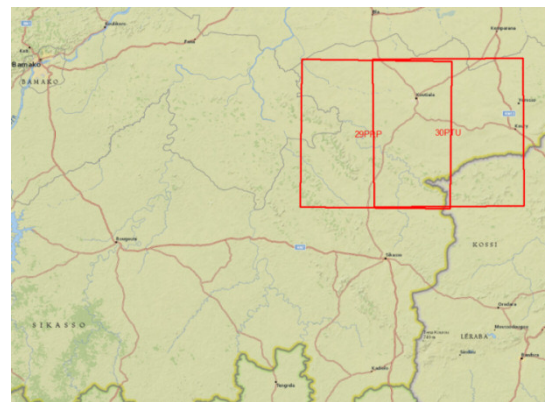


Figure 2-3: Mali

3 State-Of-The-Art

To monitor land cover and its changes, Earth observation (EO) data with a high temporal and spatial resolution are required. However, up to recently these scientific as well as user requirements could only be satisfied by dense satellite data time series on local, continental and global scale. In this context each Sentinel mission brings new opportunities and challenges for the time series data processing lines. However, robust methods for fully automated pre-processing of Sentinel time series data streams are required [AD04]. The quality of the pre-processing procedure determines the thematic quality, content, and accuracy that can be achieved in any subsequent information extraction processes. Therefore, pre-processing approaches for high volume data processing based on the high resolution satellite constellations are addressed in this chapter.

3.1 Processing methods for optical time series

The processing methods for optical time series include the generation of spatio-temporally consistent optical time series with top of atmosphere reflectance values. Therefore following pre-processing steps are available: a) extraction of metadata, b) optional - atmospheric correction, c) optional - topographic normalisation, d) cloud, cloud shadow and snow masking, e) radiometric calibration, f) derivation of indices and variables, g) generation of metadata according INSPIRE directives and h) generation of quality control reports [AD04]. Considering the data size and number of scenes within the time series, an automated and rapid processing chain is essential.

3.1.1 Atmospheric correction

In phase 1 of ECoLaSS, Sentinel-2 data are downloaded from these input data streams and spatio-temporally consistent optical time-series with Bottom-of-Atmosphere reflectances are generated. In order to obtain the Bottom-of-Atmosphere (BOA) reflectances for optical data, the two main processors are Sen2Cor and MAJA, but the latter is only available for non-commercial use.

SEN2COR

One software package for atmospheric correction is presented from ESA as Sentinel-2 Level-2 processor software named Sen2Cor, providing a set of algorithms, which are composed of several state-of-the-art techniques performing the task of correcting the reflectance values (Müller-Wilm et al., 2013).

The processor performs the atmospheric-, terrain and cirrus correction of Top-of-Atmosphere (TOA) Level-1C input data creating Bottom-of-Atmosphere (BOA) and if required terrain- and cirrus corrected reflectance images. Parameters like atmospheric visual transparency, aerosol type and the water vapour column are needed for the atmospheric correction process and derived through the associated bands (Müller-Wilm et al., 2013).

The Dense Dark Vegetation algorithm performs the task of the Optical Aerosol Thickness detection and aerosol type estimation, requiring areas of known reflectance behaviour. How the process works in detail is explained by Richter et al. (2006):

"The method is based on a stable relationship between surface reflectance ρ in the short-wave infrared (SWIR; 2100–2200nm) and reflectance in the blue (480 nm) and red (660 nm) wavelengths. It starts with the approximation $\rho_{SWIR} = \rho_{SWIR}^{TOA}$ where ρ^{TOA} is the Top-of-Atmosphere reflectance. This approximation is fairly accurate, because of the small path radiance and high atmospheric transmittance $\tau > 0.9$ in the SWIR region [...]. Then, the relationships $\rho_{blue} = \frac{\rho_{SWIR}}{4}$ and $\rho_{red} = \rho_{SWIR}/2$ are employed and the differences between the TOA apparent reflectance and the reflectance from the above relationships are used to calculate the path radiance and corresponding aerosol optical depth. The

spectral reflectance correlation between the red and SWIR wavelengths is sufficiently stable for an aerosol retrieval."

Louis et al. (2016) states after a first validation process comparing with AERONET sunphotometer measurements that the algorithm only works with dark dense vegetation pixels within each granule.

Furthermore, **Water Vapour** information is required to correct reflectance values, gathered through the Atmospheric Pre-corrected Differential Absorption (APDA) algorithm, using the bands B8a and B9. Band 8a provides reflectance values in an atmospheric window region, whose values can be seen as a reference for the water vapour. Band 9 presents reflectance values in an absorption region. The offset between those two bands is a measure for absorption depth, which dominates the lower atmosphere, assuming that the surface reflectance for B9 is the same as for the B8a. In this case, the absorption depth represents water vapour column content (Müller-Wilm et al., 2013). Louis et al. (2016) observed after a first validation process with AERONET sunphotometer measurements that the water vapour retrieval algorithm is less influenced by clouds and missing dark dense vegetation pixels than by the aerosol thickness detection results. Since the water vapour column in the upper atmosphere and the ozone absorption content cannot be estimated from image data, seasonal climatological values are included, differentiating between summer and winter atmosphere (Louis et al., 2016).

Optionally a **cirrus correction** can be performed using band 10, which is located in the 1380 nm spectral region, where the ground reflected signal is totally absorbed receiving only scattered cirrus signal at the sensor (Richter et al., 2011). The correlation between the cirrus band (B10) and other bands in NIR and SWIR leads to the cirrus contribution. This contribution can be removed from the radiance signal (Müller-Wilm et al., 2013; Louis et al., 2016). An established cirrus removal method exists for visible and near infra-red bands. The Sen2Cor processor uses an extended technique removing cirrus during the atmospheric reflectance calculation to avoid reflectance artefacts and improving the accuracy of surface reflectance retrievals. Richter et al. (2011) describe the standard cirrus removal method:

"A 'virtual' surface is defined consisting of the earth's surface and atmosphere beneath cirrus clouds. It includes the effects of surface reflection and atmospheric scattering and absorption processes. Above cirrus, there is the remaining part of the atmosphere with a residual water vapour column. [...] The cirrus reflectance in the VNIR (from 0.4 to 1 μ m) is linearly related to the cirrus reflectance at 1.38 μ m [and] [...] the cirrus single scattering albedo (SSA) is close to 1 in this part of the spectrum which means that scattering dominates. It does not hold in the SWIR spectrum (1.6 μ m, 2.2 μ m) where cirrus absorption is higher [...]."

This means that standard cirrus removal method only considers channels in NIR window regions, excluding the 0.94 μ m water vapour region. Hence, an enhanced cirrus removal method is introduced by Richter et al. (2011), accounting for the water vapour absorption above cirrus clouds, during the atmospheric correction process using band 10. "For instruments with similar channels as Sentinel-2, the water vapour is retrieved with a band in a window region (around 0.87 μ m) and one in the 0.94 μ m absorption region (Richter et al., 2011)." The transmittance between sun-cirrus and cirrus-satellite is initially unknown, therefore radiative transfer codes using climatological atmosphere profiles for different seasons and areas adopted from MODTRAN models are used (Richter et al., 2011).

Sen2Cor uses a combined approach for the atmospheric and topographic correction, eliminating the topographic effects during the BOA reflectance calculation. In order to the terrain correction processing, a digital elevation model can automatically be downloaded by the processor using the SRTM 3 arcs model. The 90m SRTM Digital Elevation Database required by the algorithm for rugged terrain will be downloaded from CGIAR-CSI. The topographic correction requires parameters like slope, aspect and hill shadow. The digital elevation model will be automatically resampled and referenced to the Sentinel scene (Main-Knorn et al., 2015; Müller-Wilm et al., 2013).

"The atmospheric model of Sen2Cor (Level-2_Atmospheric) is dependent on the calculation of radiative transfer functions for different sensor and solar geometries, ground elevations, and atmospheric parameters. [...] The processor reads the parameter in form of Look Up Tables (LUTs) pertaining to this parameter space and interpolates if required. The LUTs have been generated via libRadtran, a library for the calculation of solar and thermal radiation in the Earth's atmosphere." (Müller-Wilm, 2015) There are 24 different look-up tables provided by the processor including tables regarding rural and maritime aerosols, mid-latitude summer and winter atmosphere profiles and various types of ozone concentration, which can be configured in the Level-2 GIPP.xml file (Louis et al., 2016).

The **Aerosol-type** is selected depending on the climatology from the scene acquisition area and time. By using built-in MODTRAN aerosols, for example, rural or maritime aerosol types are differentiated. The ozone content is provided by ancillary data for each scene individually (Richter et al., 2006; Müller-Wilm et al., 2013). The ozone content concentration, measured in Dobson Units (DU), should be chosen depending on the season (summer or winter). The standard ozone content for a latitude summer atmosphere is 331 DU and in winter it is about 330 DU (Müller-Wilm, 2015).

After all required parameters for the atmospheric correction are estimated, the BOA reflectance calculation is performed using a set of the available and calculated LUTs, chosen by the user according to geographic location and climatology (Main-Knorn et al., 2015; Müller-Wilm et al., 2013). Output images are automatically resampled to a user-defined spatial resolution based on the three resolutions available in the input image. The three bands with 60m spatial resolution (Bands 1, 9 and 10) will be omitted in the level-2a output since they are not needed for land cover applications (Louis et al., 2016; Müller-Wilm et al., 2013; Fletcher K., 2012). In a first validation process again using AERONET as reference data, Louis et al. (2016) observed a high spectral agreement between several example spectra (e.g., forest, bright soil, etc.) and the Sentinel image data. The reference image has been calculated running the atmospheric correction on the Sentinel scene with an AOT constant measured by the AERONET instrument (Louis et al., 2016).

Another major output of the processor is the scene classification, which detects 12 different land cover classes (Müller-Wilm et al., 2013). "The algorithm is based on a series of threshold tests that use as input Top-of-Atmosphere reflectance from the Sentinel-2 spectral bands. In addition, thresholds are applied to band ratios and indexes like the Normalized Difference Vegetation - and Snow Index (NDVI, NDSI)" (Müller-Wilm et al., 2013). In a first validation approach, the scene classification reached an overall accuracy of 78%. Random stratified sampling points are visually interpreted as a reference, with at least 50 points per class (Louis et al., 2016).

MACCS-ATCOR JOINT ALGORITHM MAJA

MAJA is a new software package for atmospheric correction presented from CNES, DLR and CESBIO. MAJA stands for MACCS-ATCOR Joint Algorithm and represents a cloud screening and atmospheric correction software. The MAJA code uses multi-temporal and multi-spectral information to detect clouds, cloud shadows, water and snow. Moreover, the algorithm estimates the optical properties of the atmosphere (water vapour and aerosol content) and performs an atmospheric correction including adjacency and irradiance variations due to terrain (Rouquié et al., 2017).

As a first step, the algorithm detects areas covered with clouds, cloud shadows, snow and water and generates corresponding masks. In these areas, the atmospheric corrections won't provide reliable results. The mask is generated based on multitemporal data sets to improve the results. Second, two components are computed for the atmospheric correction, the atmospheric absorption and the atmospheric scattering. In the MAJA package, the atmospheric absorption correction is based on the SMAC model (Simplified Method for Atmospheric Correction) and additionally it is based on the Water Vapour Absorption knowledge derived from the corresponding band. Third, the aerosol optical thickness is computed; therefore three different methods are available within the MACCS software. The first

method is based on a multi-temporal dataset assuming that the aerosol concentration varies quickly over time but slowly in space. The second method is a spectral method assuming that the vegetation is characterized by a constant ratio of reflectance for some spectral bands. The last method represents a spectro-temporal method which combines the previous two methods. The last contribution, which will be corrected by the algorithm is the blurring due to the landscape surrounding the site imaged, i.e. the adjacency effects (Lonjou et al., 2016; Rouquié et al., 2017)

"The algorithm implemented gets its reliability from the use of the temporal dimension to improve the knowledge of the area that has been imaged and make the distinction between what is slowly changing, i.e. the landscape itself, and elements quickly varying such as clouds, clouds shadows and aerosols. In addition to the BOA reflectance for all the bands, a set of composite images at low resolution is also appended into the Level-2 product; they contain the most recent good quality surface reflectance or cloud free TOA reflectance and they are enriched date after date."(Lonjou et al., 2016)

MAJA is available as executable code for Linux RedHat/CentOS (see https://github.com/olivierhagolle/Start_maja) since October 2nd, 2017. Next versions will integrate DLR's methods for cirrus correction and an aerosol type estimation (Donadieu and L'Helguen, 2016). MAJA is freely available in a binary version for non-commercial use. The software may not be used for commercial purposes, where the following points are included under "commercial use": Sale of the software, the sale of products using the software and sale of services that have integrated the software (CNES, 2018).

3.1.2 Cloud, Cloud Shadow and Snow Masking

As a result of the correction software packages, mentioned in the last chapter, additionally, to the corrected image data, cloud, cloud shadow and snow masks can be derived. Cloud and cloud shadow detection is one of the most important pre-classification activities when dealing with optical remote sensing data as it is of high interest for most application to discriminate between clear sky pixels and pixels covered by clouds or cloud shadow. Therefore, it is among the first processing steps after pre-processing the raw data. The identification and exclusion of clouds and clouds shadows are necessary due to their influence on spectral reflectance values and characteristics of the thematic classes. Two main cloud types are differentiated: (a) Opaque clouds, which block almost all information from the surface, and (b) cirrus clouds, which are partially transparent and share spectral signatures with the land cover beneath. Since Sentinel-2 has no bands in the thermal spectrum, the cirrus band B10 (1375 nm) is introduced to the cloud detection, which is most suitable for detecting thin cirrus. Cloud pixels are characterized by lower temperature and higher reflectance than land cover pixels. Therefore, many cloud detection algorithms depend on the thermal band (Zhu et al., 2015; Hagolle et al., 2010). Zhu et al. (2015) demonstrate that the cirrus band is even more important than the thermal band for cloud detection processes, comparing LANDSAT 4-7, LANDSAT 8 and simulated Sentinel-2 images with the Fmask cloud detection algorithm.

There is a range of existing approaches which can be summarized in following groups: 1) local or aware of spatial context, 2) self-contained or dependent on external data, 3) being probabilistic or decision-based (Hollstein et al., 2016). Hollstein et al. (2016) tested several ready-to-use classification algorithms on a database of manually labelled Sentinel-2 data. They presented a detection scheme based on classical Bayesian probability estimation which provides higher accuracies compared to decision trees computed from simple band math formulas. In the following, most common cloud detection approaches for Sentinel-2 data are introduced.

SEN2COR APPROACH

The Level-1C products embed a cloud mask specifying dense and cirrus clouds at 60m spatial resolution based on band thresholding. Dense clouds, which are characterized by high reflectance in the blue spectral region, are classified by using a threshold for B2. Additionally, a threshold in B11 and B12 (SWIR)

is used to avoid misclassification with snow. Cloud reflectance is high in the SWIR, whereas snow presents a low reflectance. “At B10, there is a high atmospheric absorption band and only high altitude clouds are detected. However, this last criterion is only applied after the first detection of cloud pixel in the blue band where cirrus is transparent.” After detecting dense clouds, an algorithm for cirrus cloud discrimination is being applied based on two criteria. First, B10 corresponds to a high atmospheric absorption band. Therefore, only high altitude clouds can be detected. Secondly, cirrus cloud being semi-transparent cannot be detected in the B2 blue band. Furthermore, morphology-based operations are applied to reduce false detections. The filter performs erosion to remove isolated pixels and dilatation to fill the gaps. Using the Level-1C products, the user can use the Sentinel-2 Toolbox to generate Level-2 data including cloud probabilities. More details can be found in the ESA Sentinel Technical Guides (2017).

The Level-2 processing includes scene classification and an atmospheric correction resulting in Bottom-of-Atmosphere (BOA) reflectances, Scene Classification Map (SCM) together with Quality Indicators (QI) for cloud and snow probabilities at 60m resolution (ESA. 2017). At Level-2, the scene classification which consists of four different classes for clouds (including cirrus), together with six different classifications for shadows, cloud shadows, vegetation, soils/deserts, water and snow.

SEN2-AGRI APPROACH

The Level-2 processor of the Sen2-Agri project is based on Multi-sensor Atmospheric Correction and Cloud Screening (MACCS) chain and ATCOR Joint Algorithm (MAJA), which perform atmospheric correction and provides Bottom-of-Atmosphere reflectance values with snow, water, cloud and cloud shadow masks (Udroiu et al., 2017). The MACCS is a further development of the CNES Orfeo Toolbox Library (B Petrucci et al., 2015) and ATCOR is a DLR atmospheric and topographic correction software (Louis et al., 2016b; Richter and Schlapfer, 2016).

FMASK APPROACH

One of the most popular approaches has been developed by Zhu and Woodcock, 2012a for Landsat 4-7. The so-called Fmask (Function of mask) approach uses Top of Atmosphere (TOA) reflectance and Brightness Temperature (BT) to detect clouds and cloud shadows. This approach has been improved and a new version has been provided for Landsat-8 and Sentinel-2 data (Zhu et al., 2015a). The major input for cloud detection for Landsat data was a thermal band which does not exist for Sentinel-2. Nevertheless, the new cirrus band of Sentinel-2 has been found to be useful for cloud detection especially for thin cirrus clouds (Zhu et al., 2015a).

ACCA ALGORITHM

The Automated Cloud-Cover Assessment (ACCA) Algorithm is an unsupervised classifier for clouds, which takes advantage of known spectral properties of thick clouds, snow, bright soil, vegetation, and water but no assessment of cirrus clouds and cloud shadows. The Landsat Processing System applies ACCA on every image prior to archiving to save the cloud cover percentages for quarter scenes and full scenes within the metadata records. The scene depended approach uses the reflective and thermal signatures to detect clouds. Problems occur in regions with snow cover at high illumination angles (Irish et al., 2006a).

MACCS-ATCOR JOINT ALGORITHM MAJA

The MAJA cloud detection method is based on a number of threshold tests including the cirrus band (B10). Additionally, multi-temporal tests are carried out to detect clouds by measuring a steep increase of the blue surface reflectance. Finally, the correlation of the pixel neighbourhood with previous images is calculated to avoid over detections based on the assumption that two different clouds at the same

location on successive dates will not have the same shape. If a large correlation is observed, the pixel is excluded from the cloud mask (Lonjou et al., 2016).

The CNES MUSCATE production centre produces near-real time the Sentinel-2 Level-2 data, corrected for atmospheric effects using the MAJA software. The products are available for download at <https://theia.cnes.fr/atdistrib/rocket/#/home>. The data is acquired in large areas shown in Figure 3-1.

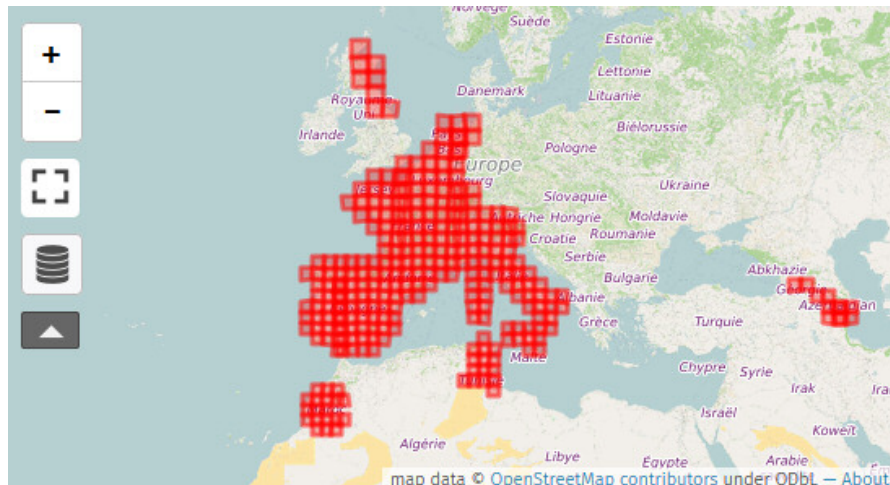


Figure 3-1: Theia Level-2 data production extent. (17.01.2017) Source: http://www.cesbio.ups-tlse.fr/multitemp/?page_id=7501

3.1.3 Topographic normalisation

A topographic correction is necessary if the test sites are characterized by mountainous terrain. The topography can significantly influence the radiometric properties of the signal received from the satellite (see Wulder and Franklin, 2012). This effect is caused by the different lighting angles resulting from the topography (cf. Gallaun, Schardt and Linser, 2007). The aim of a topographical correction is to compensate for the differences in reflectance intensity between the areas with varying slope, exposure and inclination and to obtain the radiation values that the sensor would have in the case of a flat surface. A large number of approaches have been developed to correct the topographic influence. In these algorithms, which are used for topographic normalization, the illumination conditions for each pixel are usually estimated by calculating the cosine of the sun incidence angle based on the solar position, slope and exposure of the pixel. The following formula is used to calculate the cosine of the angle of incidence (see Formula 5.1) (cf. Sola, González-Audícan und Álvarez-Mozos, 2016):

$$\cos \gamma_i = \cos \beta \cos \theta_s + \sin \beta \sin \theta_s \cos(\varphi_n - \varphi_s)$$

$\cos \beta$ is the angle of inclination, $\cos \theta_s$ is the solar zenith angle, φ_n is the aspect angle and φ_s is the solar azimuth angle, where $\cos \beta$ and φ_n are pixel-based values derived from the DEM.

According to Balthazar, Vanacker and Lambin (2012), the various topographical correction techniques developed can be divided into three types based on their complexity and requirements. The first group of procedures are simple empirical methods, such as ratio algorithms. If it is assumed that the lighting effect caused by the topography is proportional to the different bands, then the ratio of two bands can eliminate topographic effects. However, these algorithms do not produce satisfactory results because the radiometric variations caused by the topography are dependent on the wavelength and the differences between the bands are not equally proportional increasing or decreasing. This method also cuts out important image information. Since these approaches are not very successful, methods using

digital elevation models (DEMs) that provide terrain elevation, slope inclination, exposure and other information to describe surface geomorphology are often preferred (see Timothy A. Warner, 2009; Balthazar, Vanacker and Lambin, 2012).

Methods using such digital height information belong to the second group of methods, the so-called semi-empirical approaches. These include the Cosine-correction, C-correction and Minnaert models (cf. Balthazar, Vanacker and Lambin, 2012). The Cosine-correction, which Park et al., 2017 in its categorization of topographic methods does not yet rank among the semi-empirical approaches but rather among the Lambertian approaches, assumes for all wavelengths (spectral bands) that the bidirectional reflection factor is constant and independent of angle of incidence and angle of failure (cf. Park et al., 2017; Vincini and Frazzi, 2003). This type of correction is defined as follows (see formula 5.2):

$$L_n = L \cdot \frac{\cos \theta}{\cos i}$$

In the formula for Cosine-correction, L_n stands for the topographically normalized radiation, L stands for the observed radiation in uneven terrain, θ stands for the sun's angle of incidence and i for the sun's angle of elevation (cf. Vincini and Frazzi, 2003; Wulder and Franklin, 2012). The C-correction method is based on the observed empirically linear correlation between radiation L and cosine of the angle of incidence $\cos i$. It estimates the correction factor c for each band λ by forming the ratio of the regression offset $a_{1\lambda}$ to the regression slope $b_{1\lambda}$ and then applying the correction factor to the Cosine-correction (Vincini and Frazzi, 2003; Sola et al., 2016 cited after Teillet, Guindon and Goodenough, 1982)

$$L_\lambda = a_{1\lambda} + b_{1\lambda} \cdot \cos i$$

$$L_{\lambda n} = L_\lambda \cdot \frac{\cos \theta + c_\lambda}{\cos i + c_\lambda}$$

The Minnaert correction, on the other hand, changes the Cosine-correction by a constant k , which is obtained by a regression that determines how much the observed surface behaves like a diffuse Lambert lamp (see formula: 5.5). Minnaert models derive such a Minnaert constant k for each spectral band. If it has a value between 0 and 1, this means that the surface is a perfect Lambert lamp (cf. Kane et al., 2008; Hantson and Chuvieco, 2011; Vincini and Frazzi, 2003). The Minnaert correction was originally proposed by Minnaert (1941) and is defined as:

$$\log(L_\lambda \cdot \cos e) = \log L_{\lambda n} + l_\lambda \cdot \log(\cos i \cdot \cos e)$$

$$L_{\lambda n} = L_\lambda \cdot \frac{\cos^{1-k_\lambda} e}{\cos^{k_\lambda} i} \cdot \cos^k \theta$$

$$L_{\lambda n} = L_\lambda \left[\frac{\cos \theta}{\cos i} \right]^k$$

In this formula, e is the angle of precipitation angle or slope angle derived from the elevation model (cf. Kane et al., 2008; Colby, 1991). As you can see, in practice the Minnaert constant is estimated by a linear equation (cf. Hantson and Chuvieco, 2011). There are also some methods that have changed or extended the Minnaert Model (see also: Kane et al., 2008; Sola et al., 2016).

3.1.4 Sentinel-2/Sentinel-3 time series fusion

Fusion of Sentinel-2 / Sentinel-3 time series is described in detail in the deliverable report D6.1_D31.1, as this is mainly covered by WP31. In phase 1, no fusion of Sentinel-2/Sentinel-3 time series is performed, as temporal frequency of Sentinel-3 is limited, as only data from the Sentinel-3A satellite is available up to now. However, in phase 2 it is planned to perform the image fusion when Sentinel-3B time series complement the Sentinel-3A time-series.

3.2 Processing methods for SAR time series

Processing methods for SAR time series include following steps: a) automated SAR image download, b) automated preparation of digital elevation data, c) automated update of orbit files (PRECISE; RESTITUTED for near real time processing), d) thermal noise removal (for SLC) and GRD border noise removal, e) radiometric calibration, f) multi-looking and image filtering (speckle, adaptive), g) spatio-temporal speckle filtering (compare e.g. Quegan et al., 2000), h) radiometric terrain corrections (compare e.g. Small, 2011) and i) geo-referencing [AD04]. The research related to SAR time series pre-processing is, therefore, focusing on a) benchmarking of existing / currently developed algorithms and tools, b) implementation of spatio-temporal noise filtering tools optimized for Sentinel-1 time series, c) enhanced automated detection and correction of atmospheric influences, d) cluster processing to reduce processing time, e) and derivation of multi-temporal metrics [AD04].

3.2.1 Geometric pre-processing

In general, Sentinel-1 image data are accurate in terms of geometry and no additional adjustments seem to be required. A very extensive geometric location error analysis of Sentinel-1A and Sentinel-1B data has recently been published by (Schubert et al., 2017) for all Sentinel-1 data types. The mean absolute location error (ALE) for 133 Sentinel-1 GRD products, the data type which is primarily used in the ECoLaSS workflows, was found to be very small with a slant range error of 0.20m +/- 0.24, and an azimuth error of 0.31m +/- 1.31. The currently achieved geometric location accuracies for Sentinel-1, therefore, do not require any further improvements in the ECoLaSS project.

However, for Sentinel-1 GRD data processing it is essential to download the precise orbit files from ESA which are made available about 2 weeks after image acquisition at https://qc.sentinel1.eo.esa.int/aux_poeorb/. The delay of 2 weeks before precise orbits become available is a limiting factor for near-real-time applications. The ECoLaSS Sentinel-1 pre-processing workflow includes an automated co-registration of images in image geometry based on these precise orbit files. Creating a registered multi-temporal image stack is essential before applying any multi-temporal filtering. Based on the precise orbit information, all images of the same orbit are co-registered to a master scene before being filtered and orthorectified. Mean matching errors are below 1m standard deviation. Orthorectification is primarily based on the SRTM4 model which is available as a consistent layer for most of Europe. Since the SRTM model is of low spatial resolution, DEM errors related to topography are likely to occur in mountainous regions during orthorectification. However, due to unfavourable local incidence angles, most SAR information in mountain regions is in general of low accuracy and should be masked out before classification. Flat areas do not show any significant mislocation errors related to orthorectification and/or orbit information.

3.2.2 Radiometric pre-processing

Sentinel-1 Level-1 data are the generally available products intended for most data users. Level-1 products are produced as Single Look Complex (SLC) and Ground Range Detected (GRD). Most image products are available in dual-polarization mode (HH+HV or VV+VH), except older data for the African test sites which are only available as single polarization data.

Level-1 SLC products consist of focused SAR data geo-referenced using orbit and attitude data from the satellite and provided in zero-Doppler slant-range geometry. The products include a single look in each dimension using the full TX signal bandwidth and consist of complex samples preserving the phase information.

Level-1 GRD products consist of focused SAR data that has been detected, multi-looked and projected to the ground range using an Earth ellipsoid model. Phase information is lost. The resulting product has approximately square resolution pixels and square pixel spacing with reduced speckle at the cost of reduced geometric resolution. The resolution is dependent upon the amount of multi-looking performed. Level-1 GRD products are available in MR and HR for IW and EW modes, MR for WV mode and MR, HR and FR for SM mode. For the ECoLaSS project, we are mainly using Level-1 GRD products in HR and IW mode (10x10m; 5x1 look) which is the standard product. For coherence estimation, SLC data is required. The spatial resolution of SLC data is 2.7x22m to 3.5x22m and the resulting pixel spacing (the distance between adjacent pixels in an image) is 2.3x14.1m.

The standard radiometric unit of Sentinel-1 GRD data is in db. Data in db can be converted to Digital Number (DN) which is the square root of the backscatter coefficient. This reduces the file size by 50% and facilitates multi-temporal metric calculation from SAR image stacks. Previous studies have shown DN based land cover classification results to be slightly more accurate than db based classification results (Figure 3-2). For projects dealing with several terabytes of SAR data, also the file size reduction of 50% is a critical issue.

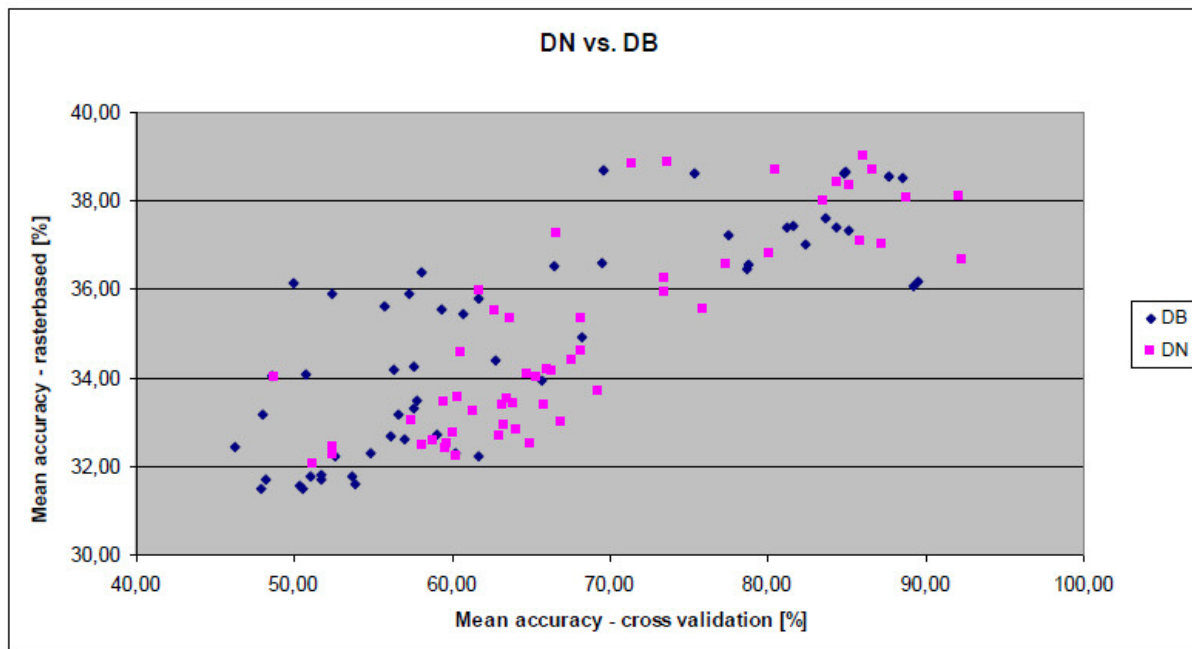


Figure 3-2: land cover classification accuracies for db and DN and different pre-processing scenarios

Radiometric calibration for Sentinel-1 data can be done simply by using the calibration Look-up Tables (LUTs) in the Calibration Annotation Data Set (CADS) delivered by ESA as part of the image metadata. The Sentinel-1 Level 1 GRD product includes several interpolated Look-Up Tables (LUTs) to convert intensity

values into beta, sigma or gamma naught values. These LUTs are used by most SAR software applications to quickly perform radiometric calibration. The calibration values can however also be calculated directly. A detailed description of the calibration equations and available metadata can be found at:

<https://sentinel.esa.int/documents/247904/685163/Sentinel-1-Radiometric-Calibration-V1.0.pdf>

In addition, radiometric terrain corrections can be applied to sigma or gamma naught data in order to minimize the terrain effects in the SAR image. RSG and SNAP Sentinel-1 Toolbox use a method for gamma naught flattening described by (Small, 2011). Ellipsoid-based or sigma naught (σ^0) based incident angle approximations fail to reproduce the effect of topographic variation in their sensor model. The gamma naught (γ^0) backscatter is converted directly from beta naught (β^0) to a newly introduced terrain-flattened γ^0 normalization convention. The interpretability of imagery treated in this manner is improved in comparison to processing based on a conventional ellipsoid or local incident angle based σ^0 normalization, but the accuracies depend on the quality of the DEM used. An example of different processing levels and a terrain flattened gamma naught image are given in Figure 3-3 below.

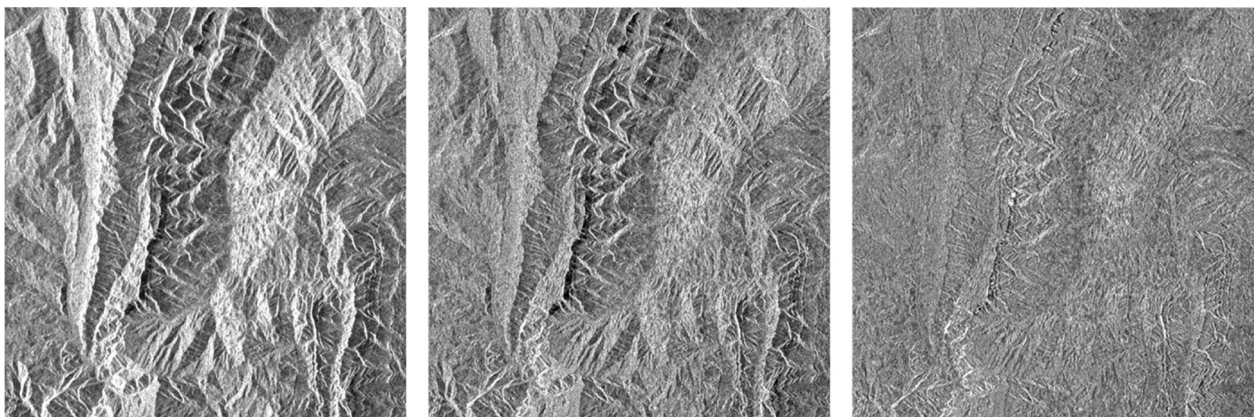


Figure 3-3: different SAR radiometric processing levels: left: beta naught (slant range geometry), middle: sigma naught (corrected for local incidence angle), right: flattened gamma naught (terrain corrections according to Small, 2011).

SAR speckle filtering and multi-looking can be applied to reduce speckle noise in SAR imagery. Common speckle filters include Lee filter, Frost filter, Kuan filter, GammaMap filter and multiresolution speckle filters (Lee et al., 1994). Figure 3-4 shows image examples filtered with the Modified-Frost and the Multiresolution filter. However, for time series of SAR data, multitemporal SAR filtering is the most widely used procedure for noise reduction (cf. Quegan et al., 2000). Input data to multitemporal filtering should not be filtered, multi-looked or orthorectified apriori.

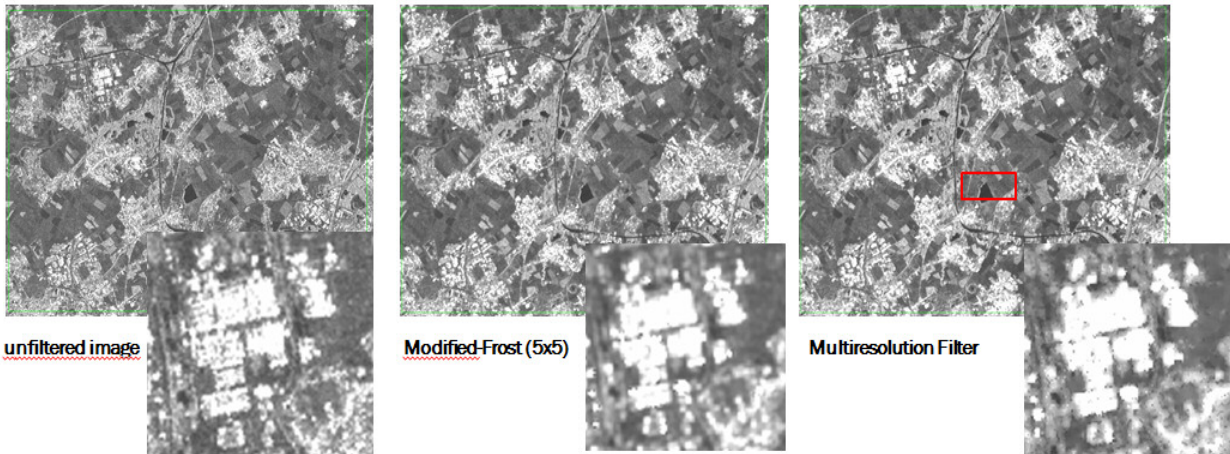


Figure 3-4: Example of two SAR speckle filters applied at an urban/rural test site

3.2.3 Coherence estimation

In the case of interferometric SAR, coherence is the normalized complex cross-correlation between two complex signals (two SAR images separated by a baseline) s_1 and s_2 and is defined as:

$$\gamma = \frac{\langle s_1 s_2^* \rangle}{\sqrt{\langle s_1 s_1^* \rangle \langle s_2 s_2^* \rangle}}, 0 \leq |\gamma| \leq 1$$

where $(..)$ denotes an average over the ensemble of pixels, usually selected by a sliding window of size (azimuth x range) in a single look complex image. Interferometric coherence is essentially a complex variable, combining both the coherence magnitude and interferometric phase. In general, the measured coherence γ can be described as a product of the following factors:

$$\gamma = \gamma_{System} \gamma_{SNR} \gamma_{Temp} \gamma_{Vol}$$

where γ_{System} combines decorrelation caused by measurement system quantization, ambiguities, relative shift of the Doppler spectra and the baseline, γ_{SNR} describes the coherence decrease caused by the finite sensitivity of the system (the signal to noise ratio), γ_{temp} accounts for changes in the target over time and γ_{Vol} describes decorrelation caused by volume scattering over vegetated areas where several scatterers at different heights contribute to scattering. The two last terms depend on target properties and have the largest dynamics when measuring natural targets.

For land cover mapping, interferometric coherence can be of great value since regions of vegetation suffer from temporal decorrelation (Zebker and Villasenor, 1992). The standard coherence estimation is based on a local complex cross-correlation and is known to over-estimate the real coherence value, especially in areas of low coherence (Touzi et al., 1999). In general, a larger window within cross-correlation provides a better, i.e., less biased, coherence estimate. Until recently, the standard procedure was to estimate the coherence over the same window used for multi looking. However, with high resolution SAR imagery, the coherence is highly over-estimated resulting in a noisy coherence image. Therefore, a decoupling of the window size of multi looking and cross-correlation was introduced.

The resulting coherence estimate uses a variable correlation window and is a trade-off between a rather unbiased coherence estimation and a locally well-defined unblurred estimate. The specific size of the correlation window needs to be empirically determined.

A new method for coherence estimation has recently been published by Spaans and Hooper, 2016. Their new algorithm calculates the coherence for each point based on an ensemble of points with similar amplitude behaviour throughout the data set. The resulting coherence estimate is superior in resolution and noise level to the commonly used boxcar method (Figure 3-5), which has three main drawbacks. First, it suffers from a resolution problem since points with high amplitude (e.g., buildings or natural ridges) dominate the coherence estimation but leads to a smearing out of these features. Second, it tends to overestimate the coherence of a large amount of fully decorrelated points because of the random signal being similar for neighbouring points by chance. Third, as the method essentially measures the variability of phase within the window, any non-constant signal biases the coherence estimation, with high-phase gradients leading to low coherence estimates. The new method is also faster to calculate and, in contrast to existing methods, can be used in near real-time applications. This method could be very promising for ECoLaSS processing and could be exploited in project phase two.



Figure 3-5: Comparison between three different full resolution coherence estimates of the same interferogram, (20090618-20090629): (a) A 5×5 window boxcar, (b) 11×11 window boxcar, and (c) sibling-based (25 to 100 siblings per point) 41×41 search window). The boxcar coherence estimates many false high coherence points, such as in the field outlined in red. Source: Spaans and Hooper, 2016.

For land cover classification and change detection, both VV and VH coherence can be used and can have advantages depending on the change detection that is required. Some recent papers analysing Sentinel-1 12-day coherence changes for agricultural applications and grassland mowing detection describe slightly higher coherence changes for VH than for VV (Zalite et al., 2014; Tamm et al, 2016). VH coherence seems to show slightly higher sensitivity for low vegetation height/density changes (e.g. grass height changes from mowing) while VV seems to be more sensitive regarding vegetation to bare soil changes. But overall differences are quite small. Some studies for built-up area detection present best results when combining VH and VV coherence. Which polarization is better suited therefore seems to be related to the application and the type of change we are looking for in ECoLaSS. It is not possible to make a general statement. This will need to be investigated in task 4. Most research studies also include soil moisture products and/or local and regional precipitation data for their coherence analysis to remove unreliable SAR images affected by soil moisture. This is beyond the scope of the ECoLaSS project as in practice this is only applicable at local/regional scale. On the pan-European level, auxiliary data would need to be harmonized which is beyond the scope of the project.

3.2.4 Available SAR processing software tools

Methods and algorithms for SAR pre-processing and coherence estimation are implemented in different software packages, of which several are shortly discussed in the following paragraphs.

ORFEO TOOLBOX

Orfeo Toolbox includes several SAR processing tools but some functionalities are limited. There are a number of pre-defined recipes for SAR processing - information can be found in the OTB Cook Book current version 6.00 (<https://www.orfeo-toolbox.org/CookBook>). These tools can handle Sentinel-1 data both at SLC level and GRD processing level. It includes different radiometric processing levels (beta, sigma, gamma) but values are only interpolated from the metadata look-up tables delivered by ESA. A speckle filter can be applied. Frost, Lee, Gamma-MAP and Kuan filters are available. Polarimetric decompositions are possible, but this tool requires full polarimetric data with at least 3 polarizations (HH, HV, VH or VV). This is not the case for Sentinel-1. A multi-temporal SAR filter is not included. There are two kinds of decompositions: coherent ones and incoherent ones. In the coherent case, only the Pauli decomposition is available. In the incoherent case, there are following decompositions available: Huynen, Barnes, and H-alpha-A. The user must provide three one-band complex images HH, HV or VH, and VV.

For SLC data, the toolbox includes a SAR debursting tool required for Sentinel-1 processing. InSAR applications include modulus and phase calculations. Coherence processing is not included in the CookBook but generally seems supported by Orfeo + Monteverdi toolboxes. No information could be found regarding the specific calculation of short-term coherence products. Parallel execution is supported. BandMath tools can be used for different types of (statistical) image analysis.

SNAP SENTINEL-1 TOOLBOX

The Sentinel-1 toolbox is a very powerful tool for processing both Sentinel-1 GRD and SLC data. However, it is tricky to integrate into cloud computing infrastructures because of many dependencies. Some tasks seem very slow (e.g. orthorectification). It supports command line processing and easy GUI based workflow generation.

A large number of SAR processing tutorials for the Sentinel-1 Toolbox can be found online at ESA:

<http://step.esa.int/main/doc/tutorials/sentinel-1-toolbox-tutorials/>

The software functionalities include:

- Data import (GRD and SLC)
- Automated orbit information update
- Specific Sentinel-1 TOPS processing tools
- Radiometric calibration (based on metadata look-up tables only)
- Radiometric terrain correction
- Multi-looking
- Speckle filtering (several filters)
- Stacking tool
- Image co-registration tools (with and without DEM)
- Multi-temporal filtering
- Linear to dB conversion
- SAR mosaicking tool
- Orthorectification
- Interferometric tools include:

- **Coherence estimation** (no time window selection – a priori stacking of relevant images needed)
- Interferogram formation
- Phase unwrapping
- InSAR filtering tools

Coherence estimation with SNAP Sentinel-1 toolbox:

This operator computes the coherence image, with or without subtraction of the reference phase. The reference phase is subtracted if there is a 2d-polynomial computed as a result of the "Compute Interferogram" operator. It is not subtracted if this information is not included within the metadata, or if the number of polynomial coefficients in "Compute Interferogram" operator is set to 0. This is a "general" coherence estimation operator and not exclusive only for InSAR applications. It can be utilized to estimate the coherence information from any stack of co-registered complex images. In order to reduce the noise, as the post-processing step, you can perform multi-looking (with Multi-look Operator). So far, there is no specific tool available for short-term coherence estimation from Sentinel-1.

DORIS

The Delft Institute of Earth Observation and Space Systems of Delft University of Technology has developed an Interferometric Synthetic Aperture Radar (InSAR) processor named Doris (Delft object-oriented radar interferometric software). The Doris software can be downloaded freely, but only for non-commercial applications (conditions). The software includes a tool for coherence estimation. More information on <http://doris.tudelft.nl/>

GMTSAR

GMTSAR is an open source (GNU General Public License) InSAR processing system designed for users familiar with Generic Mapping Tools (GMTs). The code is written in C and will compile on any computer where GMT and NETCDF are installed. The system has three main components:

1. a pre-processor for each satellite data type (ERS-1/2, Envisat, ALOS-1, TerraSAR-X, COSMOS-SkyMed, Radarsat-2, Sentinel-1A/B, and ALOS-2) to convert the native format and orbital information into a generic format;
2. an InSAR processor to focus and align stacks of images, map topography into phase, and form the complex interferogram;
3. a postprocessor, mostly based on GMT, to filter the interferogram and construct interferometric products of phase, coherence, phase gradient, and line-of-sight displacement in both radar and geographic coordinates;

GMT is used to display all the products as postscript files and KML images for Google Earth. A set of C-shell scripts has been developed for standard 2-pass processing as well as image alignment for stacking and time series.

RSG- REMOTE SENSING SOFTWARE PACKAGE GRAZ

The project partner JOANNEUM RESEARCH developed a comprehensive software package for SAR data processing. It can process most commercially available SAR sensors and image formats. The SAR software suite includes tools for automated image download, image ingestion to RSG format, radiometric processing, geometric processing (image registration), SAR speckle filtering, radiometric terrain correction, image stacking, multi-temporal stack analysis, coherence estimation (short-term and long-term) and interferometric analysis. The software is available commercially.

4 Testing and benchmarking of candidate methods

In phase 1 of ECoLaSS, the processing of high volume data processing lines mainly based on the high resolution satellite constellations is addressed. This topic is important for the pan-European component, where a large volume of satellite earth observation data at high resolution has to be processed on a continental level. The main challenges are the combination of current processing modules into high volume data processing lines, as well as upscaling from local or country level to pan-European or potentially global level in the future. Therefore, a large volume of data needs to be efficiently processed to produce data composites and derive calibrated and validated variables.

4.1 Benchmarking of methods for pre-processing of optical time series

The processing methods for optical time series include the generation of spatio-temporally consistent optical time series with Top-of-Atmosphere reflectance values. Considering the data size and number of scenes within the time series, an automated and rapid processing chain, including all necessary pre-processing steps, is essential. The following sections provide methods and benchmarking thereof, focussing on the topics of atmospheric correction, cloud, cloud shadow and snow masking, topographic normalization and geometric consistency of optical time series data. The candidate methods for pre-processing optical time series, benchmarking criteria, the implementation and results of benchmarking and resulting conclusions are described in the sub-sections of this chapter.

4.1.1 Benchmarking of candidate approaches for atmospheric correction

Applying an atmospheric correction is particularly important when dealing with multitemporal data as it cannot be assumed that lighting and atmospheric conditions are the same for all images. Differences between the images caused by atmospheric influences would influence the accuracy of the classification result. Cloud masking and land cover classification tasks require an atmospheric correction beforehand.

Sentinel-2 data sets are downloaded for the ECoLaSS test and demonstration sites, from which spatio-temporally consistent optical time-series with Bottom-of-Atmosphere reflectances are being generated. In order to obtain the Bottom-of-Atmosphere reflectances for optical data, several processors like Sen2Cor (processor for Sentinel-2 Level-2A product generation) and MAJA (Maccs-Atcor Joint Algorithm) are available in the literature. ESA and NASA are currently evaluating those algorithms among others in an inter-comparison exercise project named ACIX (Atmospheric Correction Inter-comparison eXercise) (<https://earth.esa.int/web/sppa/meetings-workshops/acix>) for understanding the different uncertainty contributors and improving the available atmospheric correction processors. The official method for the atmospheric correction of Sentinel-2 data used in the Sentinel toolbox provided by ESA is Sen2Cor.

4.1.1.1 Description of Candidate Methods

SEN2COR BY ESA

Sen2Cor presented from ESA as Sentinel-2 Level-2A processor provides a set of algorithms, which is composed of several state-of-the-art techniques performing the task of correcting atmospheric-, terrain and cirrus effects based of Top-of-Atmosphere Level-1C input data. As a result Bottom-of-Atmosphere products and if required terrain- and cirrus corrected reflectance images are created. Furthermore, parameters like the atmospheric visual transparency, the aerosol type and the water vapour column are needed for the atmospheric correction process and derived through the associated bands (Müller-Wilm et al., 2013).

MAJA BY CNES-DLR

The MAJA processor uses multi-temporal information to detect clouds, cloud shadows and to estimate the optical properties of the atmosphere (Rouquié et al., 2017). The algorithm detects areas covered with clouds, cloud shadows, snow and water based on multi-temporal data sets and generates corresponding masks. Further, two components are computed for the atmospheric correction, the atmospheric absorption and the atmospheric scattering. Another contribution which will be corrected by the algorithm is the blurring due to the landscape surrounding the site imaged, i.e. the adjacency effects (Lonjou et al., 2016; Rouquié et al., 2017).

4.1.1.2 Benchmarking Criteria

A comparative quality assessment of atmospheric correction methods can be based on following criteria, which are currently considered as standard in literature. There are three main approaches for evaluating surface reflectance products.

COMPARISON WITH GROUND TRUTH DATA

Gascon et al., 2017 and Pflug et al., 2016 used the AERONET sunphotometer measurements to validate the Sentinel-2 Bottom-of-Atmosphere product. The validation datasets have been selected for radiometric validation. They cover different land cover types, different atmospheric conditions and include different latitudes in order to cover various solar angles and seasons. The objective is to estimate the uncertainty of BOA product resulting from processing Sentinel-2 data using Level-2A processor Sen2Cor.

INTER-ORBIT SPECTRAL STABILITY

Another approach is to check the surface reflectance stability by comparing two images of the same sensor in areas from overlapping orbits. Therefore, a region in Germany has been selected, comparing two overlapping images with clear skies and observed from two different orbits on two different dates in summer 2015, which are close together.

CONSISTENCY WITH OTHER SENSORS

A third approach checks for the consistency of the Top-of-Atmosphere products derived from comparable sensors. The consistency between the different atmospheric correction approaches is needed, to better combine various products for analysis. To check the consistency of the Sentinel-2 Level-2A products derived from the Sen2Cor processor (Version 2.2.1), Sentinel-2 MSI is compared with two other sensors with similar spectral resolution (LANDSAT 8 OLI and TERRA/AQUA MODIS).

4.1.1.3 Implementation and Results of Benchmarking

COMPARISON WITH GROUND TRUTH DATA

Comparison with ground truth data was performed e.g. by Gascon et al. (2017). The validation of the surface reflectance products was thereby performed comparing Sen2Cor outputs with surface reflectance reference data generated with sunphotometer measurements by the AERONET instrument. Therefore, a 9km x 9km subset around the sunphotometer location was created and a reference BOA reflectance is generated by running the Sen2Cor atmospheric correction with a constant AOT value equal to the AOT value measured. The results are considered as “truth” regarding the surface reflectance since the greatest uncertainty in atmospheric correction comes from the aerosol characterization (Gascon et al., 2017). The comparison shows small differences in surface reflectance between both products.

Pflug et al., (2016) summarize: “*The Level-2-product is clearly improved in comparison with the L1C-product. [...] DDV-pixels are distributed over the full image. The granule contains 3.1% DDV-pixels, which is sufficient for an accurate estimation of aerosol amount. [...] Both AOT and WV averages across the subset are in good agreement with the reference value obtained from AERONET. Sen2Cor provides an AOT value at 550 nm of 0.20 with reference value from AERONET of 0.23. WV is estimated from Sen2Cor with a value of 2.46 cm with a reference value from AERONET of 2.63 cm. Several example spectra were extracted in the reference image and in the image to validate. Example spectra for dark and bright soil, for forest and for different other vegetated locations show the expected spectral dependency and agree between reference and the spectra to be validated. A difference up to 0.04 in surface reflectance between Sen2Cor-processing and reference had been found, leading to a Normalized Density Vegetation Index (NDVI) uncertainty up to 0.06*”.

INTER-ORBIT SPECTRAL STABILITY AND CONSISTENCY WITH OTHER SENSORS:

To check the consistency of the Sentinel Level-2A products derived from the Sen2Cor processor (Version 2.2.1), we compared Sentinel-2 MSI with two other sensors with similar spectral resolution (LANDSAT 8 OLI and TERRA/AQUA MODIS). Figure 4-1 highlights the different bands for all three sensors and also the differences in bandwidths for corresponding spectral bands of each sensor. It also shows which bands are comparable with each other over all three sensors. With regards to OLI, the spatial resolution of MSI is finer except regarding the bands used for the atmospheric correction. The major spectral difference between OLI and MSI is the presence of red-edge bands in MSI and the thermal bands in OLI. Regarding MODIS the spatial resolution of MSI and OLI is much finer. In order to compare the sensors, following bands are chosen and resampled to 920m, representing almost twice the MODIS resolution (see Table 4-1). MODIS and OLI sensor products adopted for this analysis are downloaded already containing reflectance values. The Sentinel-2A scenes are processed with the Sen2Cor processor.

Table 4-1: Corresponding bands regarding each spectral region across MSI, OLI and MODIS

	MSI	MODIS	OLI
RED	B4	B1	B4
NIR	B8a	B2	B5
SWIR	B11	B6	B6
Resolution	20m	463m	30m

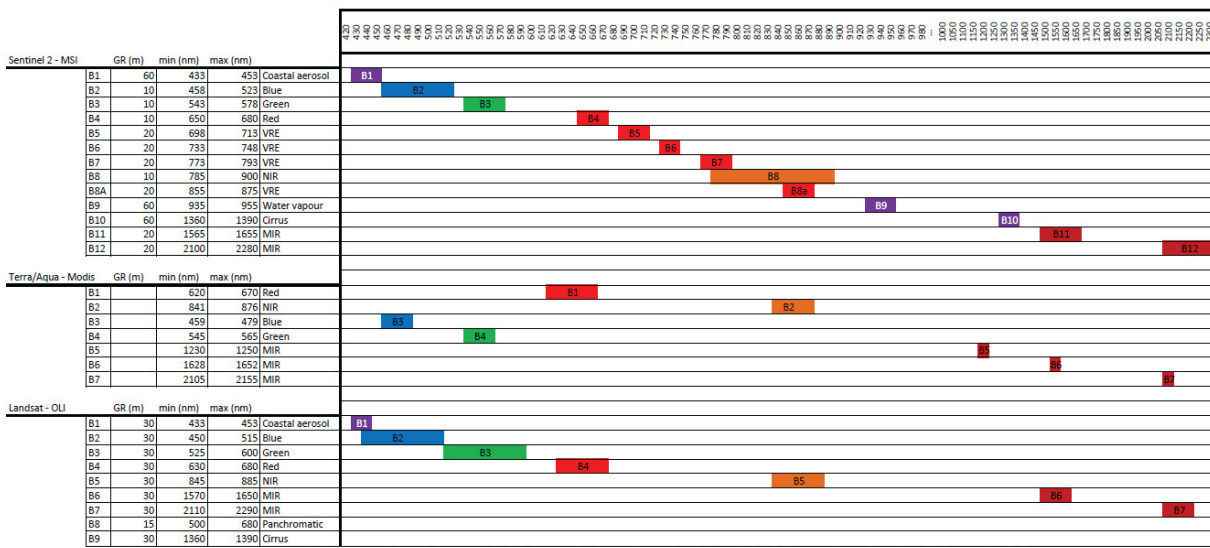


Figure 4-1: Comparison between the MSI, MODIS and OLI sensors. Based on: U.S. Geological Survey (2016), Suhet (2015), and NASA Official

First, regions of interest are defined for the thematic classes water bodies, broad-leaved forest, coniferous forest and urban area in the overlapping area of all images to be compared including Sentinel-2A MSI of 26.08.2015, Sentinel-2A MSI of 29.08.2015, TERRA/AQUA MODIS of 29.08.2015, and LANDSAT 8 OLI of 30.08.2015. One region of interest for each class is defined containing homogeneous pixels in the resampled products and centred in the land cover feature to avoid adjacent land cover pixels influencing the comparison. The chosen classes can be considered as steady and therefore changes during short time intervals can be neglected.

Figure 4-2 displays the differences between the mean reflectance values of each region in the RED channel, presenting similar results over all three sensor systems for each example area. Especially between MODIS and OLI only small differences are observed. In relation to the other sensors, the reflectance values for OLI within the water body area are twice as high. Those differences can be explained by the presence of thin cirrus clouds. Nevertheless, it should be considered that in relation to the other classes or in absolute terms the differences are minor. Regarding broadleaved and coniferous forests the MSI sensor shows slightly lower reflectance values in both scenes, indicating that the Sen2Cor processor tends to under-correct the reflectance values. However, as shown in the statistics the reflectance differences in the red region are less than one percent.

Figure 4-3 represents the differences between the mean reflectance values of each region in the NIR channel, again showing similar results across all three sensor systems with one exception. In the case of the broadleaved region, the MSI sensor (29.08.2015) displays extreme low reflectance values in relation to the other sensors and the MSI scene acquired on the 26.08.2015. A visual inspection of the images illustrates a difference between the processed granules within the Sentinel scenes. The test sites are located in two different granules. The reflectance values of the upper granule, including the broadleaved and coniferous forest test sites explain that Sen2Cor tends to under-correct due to haze within the image. Since broadleaved and coniferous forest is located in the same granule, it would be expected that the coniferous forest reflectance values would also be underestimated. Nevertheless, the reflectance values of coniferous forest are at least 20% lower than the broadleaved reflectance values; accordingly the differences are smaller.

In Figure 4-4 the differences between the mean reflectance values for the SWIR channel are represented, illustrating more and higher differences over all three sensor systems. In comparison with the RED and

NIR channels, the Sentinel scenes also seem over-corrected in relation to the other two sensors. Regarding all example spectra, the Sentinel MSI sensors shows that Sen2Cor tends to over-correct expect for the broadleaved forest area, where the LANDSAT scene seems slightly under-corrected. Nevertheless, it should be noted that the absolute reflectance differences are less than 2%.

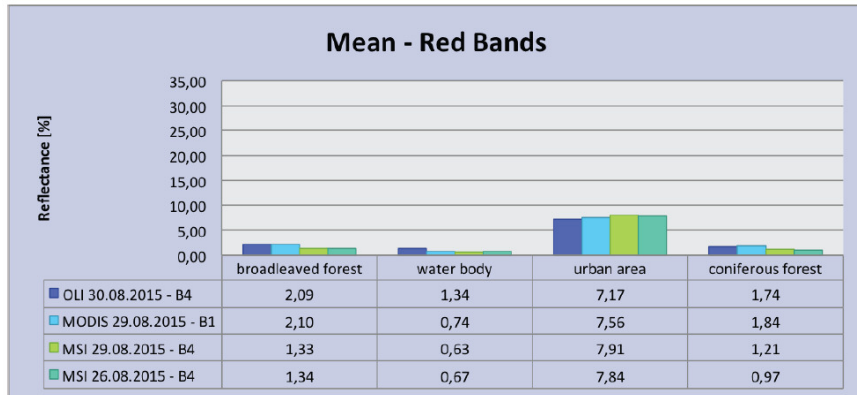


Figure 4-2: Mean reflectance - RED band

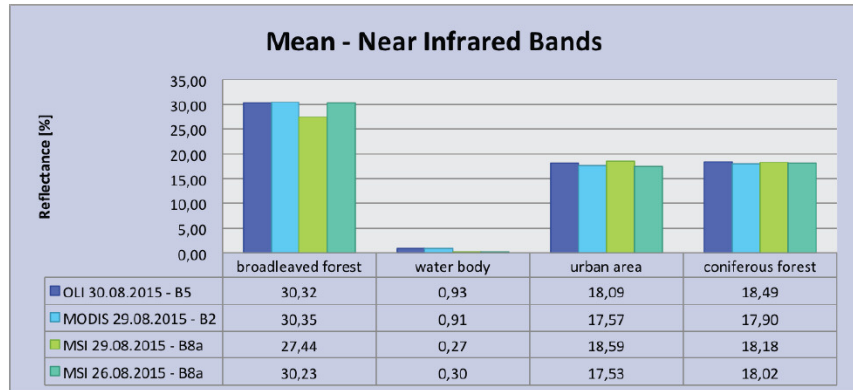


Figure 4-3: Mean reflectance - NIR band

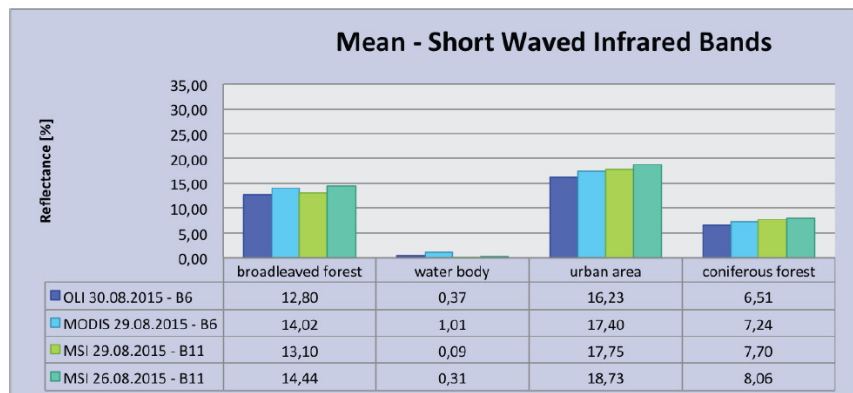


Figure 4-4: Mean reflectance - SWIR bands

These differences are probably due to directional effects as the observations from two different orbits are made with different viewing angles.

4.1.1.4 Summary and Conclusions

In general, the example spectra for coniferous forest, broad-leaved forest, water and urban area show the expected spectral agreement between reference spectra and images spectra to be compared. For the most part, atmospheric correction performed with Sen2Cor works consistent like shown in the comparison in chapter 4.1.1.3. Gascon et al. (2017) achieved in their early validation approach of the Sen2Cor processor similar results stating that the early Sentinel-2 Level-2A products show good inter-orbit reflectance comparability if there are DDV pixels present in the granule.

"The first results are very encouraging in term of image quality performance as well as in term of computing performance. Results obtained show the very good performances of the mission products both in terms of radiometry and geometry. Thanks to a robust in-flight calibration strategy, the radiometry is both accurate (<5% absolute uncertainty) and stable (<1%/year variation estimated). Cancelling seasonal effects on diffuser acquisition is the key to this performance: this involves an accurate model of the Sun-Earth distance and of the diffuser bi-directional Reflectance Function. Further progress on the latter point should lead to improved pixel response stability (i.e. Fixed Pattern Noise) in the near future. " (Gascon et al., 2017).

Nevertheless, difficulties arise, when no dark dense vegetation pixels are within the granule. Small over-correction in comparison with the AERONET sunphotometer measurements is observed by Louis et al. (2016), which may result from false aerosol parameters because Sen2Cor estimated higher aerosol optical thickness compared to the reference data. It should be noted that there is still a possibility that the reference data obtained from AERONET sunphotometer measurements can be under-corrected. The major problem is the granule wise processing of Sen2Cor, which results in granule borders within the scenes in cases of missing dark dense vegetation pixels.

Comparing the two main atmospheric correction software packages both show advantages and drawbacks and are not performing sufficiently enough to achieve a high thematic quality, content and accuracy in any subsequent information extraction process. Concerning the atmospheric correction the inter-orbit spectral stability and the consistency with other sensors show that Sen2Cor is able to achieve consistent results only if the data sets fulfil certain characteristics, e.g. presence of DDV pixels. MAJA atmospheric corrected products are not evaluated due to the fact that MAJA cannot be used in commercial projects such as HRL production, considering the licence and implementation issues.

4.1.2 Benchmarking of candidate approaches for cloud, cloud shadow and snow masking

A significant improvement of current methods for the classification/masking of clouds, cloud shadows and snow is required for enabling a fully automated generation of highly accurate masks in near-real time. Whereas current methods, such as implemented in the Sen2Cor (Louis et al., 2016b) or LEDAPS software (Home et al., 2013), classify each scene separately, improved methods are currently being developed exploiting the additional information provided by time series.

4.1.2.1 Description of Candidate Methods

SEN2COR

Sentinel-2A products are provided with different already available cloud masks depending on the product level. Within the Level-2 product, the scene classification algorithms generate a classification map based on spectral threshold tests applied to the cirrus band and band ratios like NDVI and NDSI. The scene classification map provides four different classes of clouds (thin cirrus clouds, high, medium and low probability clouds), four land cover classes (vegetation, soil/deserts, water and snow) and two extra classes for shadows (differentiating between cloud shadows and terrain shadows) (Fletcher K., 2012;

Müller-Wilm et al., 2013). Furthermore, Level-1C products are provided with spatially filtered cloud masks differentiating between opaque and cirrus clouds based on the scene classification map with 60m spatial resolution.

Apart from the scene classification map a probabilistic cloud map and a snow probability map, are produced during the processing with Sen2Cor. Within several iterations with different thresholds, the cloud probability map is updated during the Sen2Cor processing. The refined threshold values for the cloud detection algorithm are derived from LANDSAT 7 Automatic Cloud Cover Assessment. The opaque cloud detection algorithm uses the water vapour band (B1) and blue band (B2) in combination with two SWIR bands (B11, B12) to differentiate between snow and clouds. The algorithm first defines potential cloudy pixels within the red part of the spectrum through a certain threshold. Further, those pixels undergo a filtering process based on spectra thresholds, band ratios and the indices normalized difference snow index (NDSI), normalized difference vegetation index (NDVI). Pixels with values lower -0,1 in the NDSI are representing snow and are excluded as potential clouds. Vegetation pixels are excluded from the cloud map deriving information from NDVI and a NIR/Green ratio. Bare soil and water are also excluded from threshold with a blue/NIR ratio. A median filter (3x3 or 5x5) is applied on the three cloud classes to reduce false classifications occurring at border region with high contrast like river contours or shorelines (Louis et al., 2010).

Further, the cirrus band (B10) is used to detect ice high-altitude clouds, which are represented by high reflectance values in B10 and low reflectance values in B1 and B2 (Fletcher K., 2012; Müller-Wilm et al., 2013). The strength of the cloud band lies in the strong water vapour absorption within the mentioned spectral region. Thresholds are used for separating clear sky pixels from cloud pixels (Louis et al., 2010).

If a correlation of the cirrus signal in the cirrus band and the other wavelengths in the NIR region can be found, the cirrus contribution can be removed. Rudolf Richter et al. (2011) introduced an enhanced cirrus removal method for multispectral images including channels in the NIR and SWIR region as well as a water vapour band and a cirrus band. During the water vapour and surface reflectance calculation within the atmospheric correction process water vapour above cirrus clouds derived from the cirrus channel is considered, leading to more accurate assessments of the water vapour map. Hence, cirrus artefacts on the SWIR region can be avoided. As mentioned in chapter 6.1.1 radiative transfer look-up tables are used for the water vapour and reflectance retrieval. Regarding the cirrus correction further look-up tables containing cirrus transmittances for different solar and viewing conditions are used (Rudolf Richter et al., 2011).

For the snow detection, four consecutive filters are applied on B2, B3, B8 and B11 reflectance values. The first filter is based on the assumption that cloud and snow reflectances are similar in band 3. On the contrary considering clouds B11 reflectance values are very high while for snow the reflectance values are low in B11. Therefore, the NDSI is calculated and thresholds are applied. The second filter eliminates pixels from the snow mask that are characterised by high NDSI values and low reflectance values in B8. The third filter removes pixels from the mask that have high NDSI values and low reflectance values in B2. The last filter eliminates water pixels from the snow mask by excluding pixels with a high NDSI value and a low ratio between B2 and B4 (Louis et al., 2010; Fletcher K., 2012; Müller-Wilm et al., 2013).

MAJA

The CNES MUSCATE production centre and the DLR produce Sentinel-2 surface reflectance data using the MAJA processor. The CNES MUSCATE production centre product generations covers areas shown in Figure 3-1 (Donadieu and L'Helguen, 2016).

The cloud mask product computed by the MACCS software is available in 10m or 20m (CLM_R1.tif or CLM_R2.tif) resolution and made out of one band coded over 8 useful bits explained below.”

- bit 0 (1): all clouds except the thinnest and all shadows
- bit 1 (2): all clouds (except the thinnest)
- bit 2 (4): cloud shadows cast by a detected cloud
- bit 3 (8): cloud shadows cast by a cloud outside the image
- bit 4 (16): clouds detected via mono-temporal thresholds
- bit 5 (32): clouds detected via multi-temporal thresholds
- bit 6 (64): thinnest clouds
- bit 7 (128): high clouds detected by 1.38 μm " (Donadieu and L'Helguen, 2016)

The MAJA algorithm performs atmospheric correction and cloud detection in Sentinel-2 images using time series. It is based on a number of threshold tests including the cirrus band (B10), multi-temporal tests to detect clouds and the correlation of the pixel neighbourhood with previous images to avoid over detections (Donadieu and L'Helguen, 2016).

4.1.2.2 Benchmarking Criteria

VISUAL ASSESSMENT

The assessment criterion is a visual interpretation of the resulting cloud masks. In the following, some image samples will show the differences between the two processors MAJA and Sen2Cor as well as the difference between the product levels available regarding Sentinel-2 data. The assessment of the cloud, cloud shadow and snow masks is done by visual interpretation of the different products.

4.1.2.3 Implementation and Results of Benchmarking

Figure 4-5 shows the different cloud classes provided by the Level-1C and Level-2 masks. The mask quality is examined by visual inspection. Level-1C cloud mask comprises cirrus and opaque not covering the full cloud extent (omission error). Level-2 scene classification presents three different classes of opaque clouds based on probabilities (high, medium, or low). Misclassifications are observed in urban areas and dry mountainous terrain, concerning all three probability classes. The high probability cloud class is calculated with a high threshold from the cloud probability mask. It is missing some thin cirrus clouds but on the contrary, misclassifications are reduced. With higher thresholds, only the cloud centres are detected, missing cloudy pixels at the borders. The lower the probability cloud class calculated with a low threshold suffers from false detection for bright surfaces in dry environments in urban areas or on mountainous terrain. In addition, Level-1C and Level-2 products contribute thin cirrus cloud classes taking advantage of the new cirrus band B10. In the Level-1C product, the mask is already further processed to reduce misclassification and fill gaps (Müller-Wilm et al., 2013). Both masks are screened reasonably well, but some thin clouds (mostly thinner plane contrails) are missed by the detection in Sen2Cor. Although Sen2Cor cloud mask tends to over detect clouds, high, medium and low probability clouds and the cirrus are adopted and further processed, due to the fact the low probabilities cloud mask are best at detecting the actual clouds.

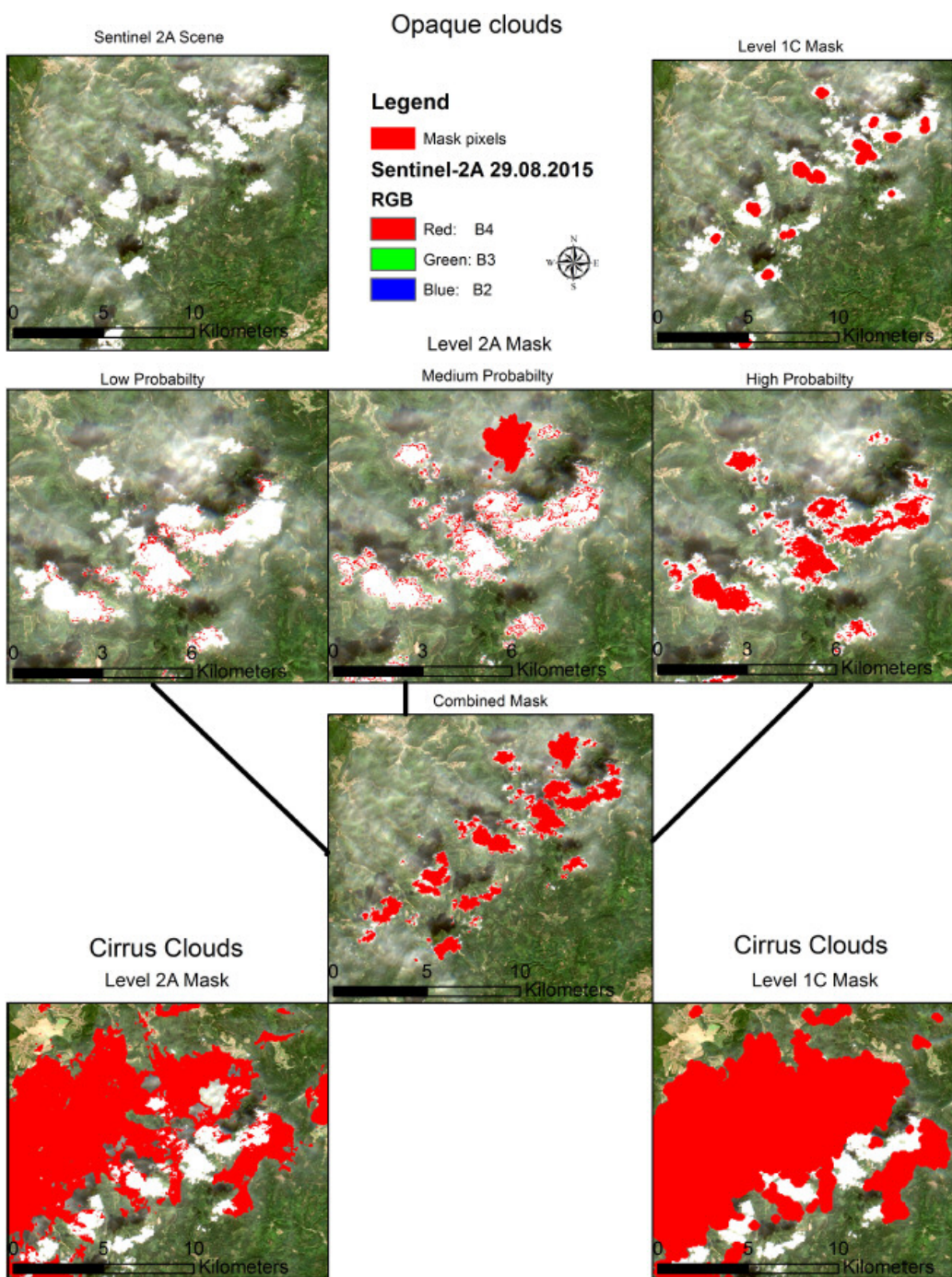


Figure 4-5: Sen2Cor cloud mask: Comparison between Level-1C and Level-2A product



Level-2A image (B4,B3,B2)



MAJA cloud mask (cloud mask in red)



Level-2A image (B4,B3,B2)



MAJA cloud mask (cloud mask in red)

Figure 4-6: MAJA cloud mask. Sentinel-2_20170705T105031_31UER; 49°41'8.69"N; 4°16'55.80"E

VISUAL ASSESSMENT COMPARISON MAJA VS SEN2COR

Sen2Cor cloud masks are based on single scenes, and provide 3 levels of cloud probability: low, medium, high, and also the cirrus mask (Louis et al., 2016b). In contrast to Sen2Cor, the MAJA algorithm uses a time-series based approach and compares pixels from previous images to assess the cloud probability (Lonjou et al., 2016).



Figure 4-7: Differences between the MAJA cloud mask (left) and the Sen2Cor cloud mask (right).

Notably, Sen2Cor tends to misclassify bright areas for clouds as shown in Figure 4-7. The example comes from a completely cloud-free image obtained above France at the beginning of May (Sentinel-2_20170705T105031_31UER). No clouds are detected within the MAJA cloud mask, while on the Sen2Cor image, urban areas, bare areas, agricultural areas and water bodies are classified as clouds. Therefore, it has been decided to use only the medium and high probability clouds within a cloud mask for further analysis and visual comparisons.



Level-2A image (B4,B3,B2)



MAJA cloud mask



Sen2Cor (Level-2A) scene classification



IMPACT Level-2A-improved Sen2Cor scene classification

Figure 4-8: Example 1: Cloud mask comparison between MAJA and Sen2Cor. Sentinel-2_20170725T105031_31UER; 49°41'8.69"N; 4°16'55.80"E



Level-2A image



MAJA cloud mask



Sen2Cor (Level-2A) scene classification



IMPACT Level-2A-improved Sen2Cor scene classification

Figure 4-9: Example 2: Cloud masks comparison between MAJA and Sen2Cor. Sentinel-2_20170705T105031_31UER; 49°41'8.69"N; 4°16'55.80"E

Figure 4-8 and Figure 4-9 show a visual comparison between the MAJA and Sen2Cor Level-2 cloud mask outputs based on a true colour image (the cloud mask are represented in red). Both methods detect large clouds but show omission and commission errors. In particular, Sen2Cor shows omission errors at the edges if the low probability cloud pixels are excluded. On the other hand, MAJA shows omission errors because it tends to underestimate small clouds and cloud shadows. Furthermore, Sen2Cor shows commission errors misclassifying bright areas for clouds and MAJA shows commission error by misclassifying forest areas for cloud shadows. Cirrus clouds are still recognised with omission errors by both. Concluding, both products still require cloud masking improvements.

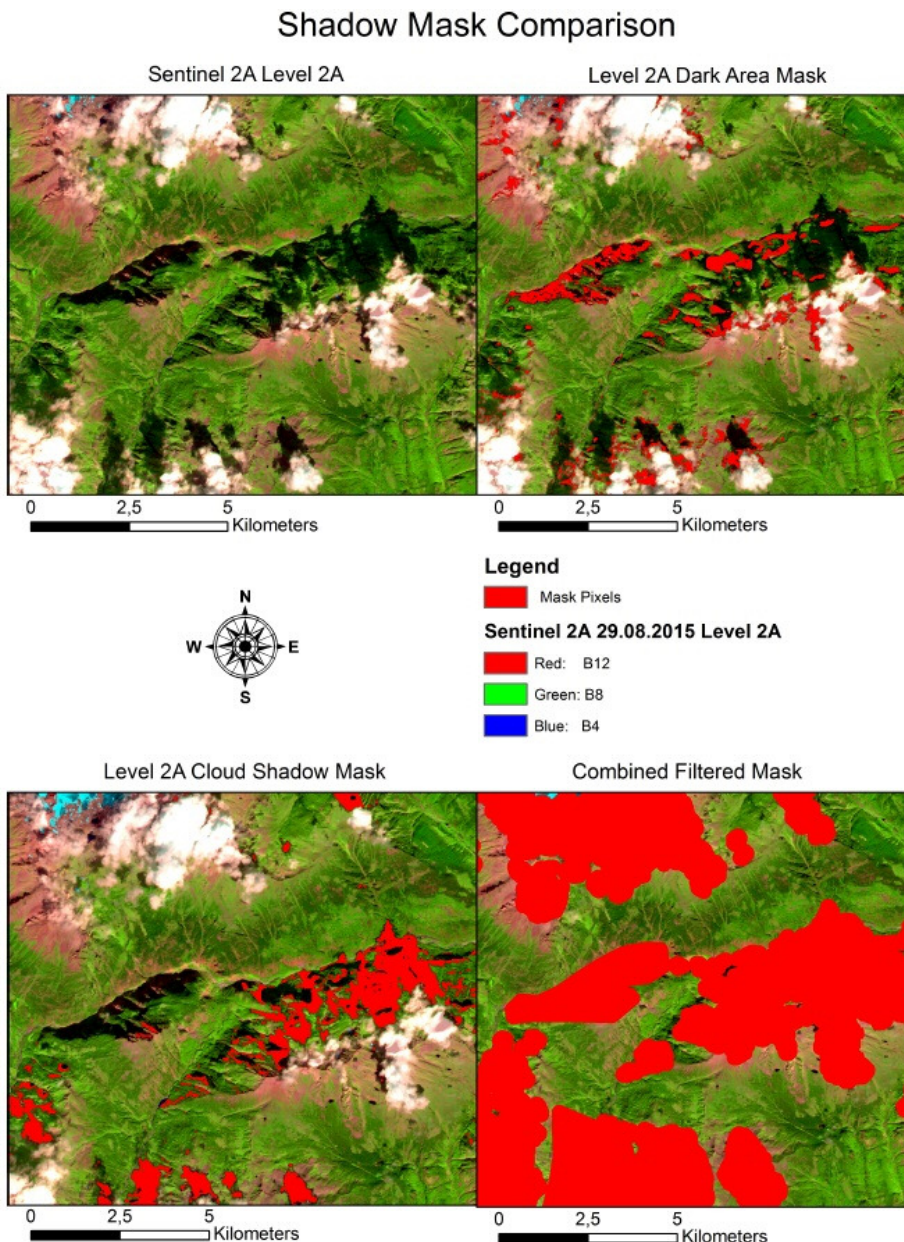


Figure 4-10: Shadow mask: Comparison between terrain and cloud shadows.

SEN2COR CLOUD SHADOW AND TERRAIN SHADOW MASK

The classes cloud and terrain shadows are only provided by the Level-2 product represented in Figure 4-10. Cloud shadows are often misclassified because they share similar spectral signatures with topographic shadows, water and wetlands (Zhu et al., 2015). The cloud and mountainous shadows in the scene classification are classified too small; therefore a buffer of 200m is applied to enlarge the shadow areas. Some water pixels with low reflectance area are masked as cloud shadow pixels due to similar reflectance values in the NIR and SWIR bands. To reduce the misclassification in the shadow mask patches with a size less than 400m (corresponding to four 10 x 10m pixels) are eliminated automatically.

In most cases, cloud and cloud shadows are located next to each other depending on the sun location and image acquisition time and the shadow size should be nearly the same size as the cloud. To reduce the cloud shadow misclassification geometric relationships between clouds and cloud shadows could be used (Jin et al., 2013).

4.1.2.4 Summary and Conclusions

Sen2Cor presents generally reasonable detection of clouds and cloud shadows excluding the low probability cloud pixels. The result can be improved by applying an adequate buffer. Still, high confusion with bright surfaces is present. Additionally, some small clouds and parts of shadows are omitted. In general, cloud omissions should be avoided, meaning bright objects should not be confused with clouds and cloud shadows should not be confused with forest areas. To avoid the commission errors the multitemporal approach used with MAJA promises better results. Regarding the usability of the cloud mask products omission errors at the edges as shown in the Sen2Cor product are preferred over misclassifications due to an easier applicable cloud mask enhancement processing chain. For example, enhancements can be achieved by applying a buffer to the estimated cloud areas.

Sen2Cor performs reasonably with the given information, the software implementation and usage is user-friendly and it is open for public usage. Considering multi-temporal information, MAJA produces better cloud masks. Nevertheless, due to the licence and implementation issues MAJA fits better for a systematic production at the ground segments, whereas Sen2Cor is simpler to implement and run operationally on the user side. Both methods still need to be improved. Sen2Cor still detects too many clouds and confuses snow and clouds. MAJA also needs some improvement due to the omission errors. With respect to MAJA being only available for non-commercial use, ECoLaSS pre-processing chains should be based on Sen2Cor for the demonstration site production.

4.1.3 Benchmarking of candidate approaches for topographic normalisation

A topographic correction is necessary if the test sites are characterized by mountainous terrain. The topography can significantly influence the radiometric properties of the signal received from the satellite (see Wulder and Franklin, 2012). This effect is caused by the different lighting angles resulting from the topography (cf. Gallaun, Schardt and Linser, 2007). The aim of a topographical correction is to compensate for the differences in reflectance intensity between the areas with varying slope, exposure and inclination and to obtain the radiation values that the sensor would have in the case of a flat surface. A large number of approaches have been developed to correct the topographic influence. In these algorithms, which are used for topographic normalization, the illumination conditions for each pixel are usually estimated by calculating the cosine of the sun incidence angle based on the solar position, slope and exposure of the pixel.

4.1.3.1 Description of Candidate Methods

Semi-empirical approaches are using Digital Elevation Models (DEMs) that provide terrain elevation, slope inclination, exposure and other information to describe surface geomorphology (Balthazar, Vanacker and Lambin, 2012). These include the Cosine correction, C-correction and Minnaert models (cf. Balthazar, Vanacker and Lambin, 2012).

TOPOGRAPHIC CORRECTION WITHIN SEN2COR SOFTWARE

The algorithm for rugged terrain integrated within the Sen2Cor package requires the existence of an appropriate Digital Elevation Model (DEM). The DEM is used to derive products like slope, aspect and terrain shadow maps. Within the software package, only two pre-existing DEMs can be used. The first one is the 90m SRTM Digital Elevation Database from CGIAR-CSI. The second supported format is the commercial 90m DTED-1 Format PlanetDEM from PlanetObserver, which must be purchased (Louis et al., 2016c).

SELF-CALIBRATING TOPONORM FROM JR-IMPACT SOFTWARE

In this approach, the Minnaert correction is iteratively applied, where the Minnaert constant k is derived land-cover specific, by a regression (see formula: 5.5). Minnaert models derive such a Minnaert constant k for each spectral band. If it has a value of 1, this means that the surface is a perfect Lambert reflector (cf. Kane et al., 2008; Hantson and Chuvieco, 2011; Vincini and Frazzi, 2003). In practice, the Minnaert constant is estimated by a linear equation (cf. Hantson and Chuvieco, 2011). There are also some methods that have changed or extended the Minnaert Model (see also: Kane et al., 2008; Sola et al., 2016).

4.1.3.2 Benchmarking Criteria

The quality of a topographic correction depends heavily on the type of land surface. Therefore, the most suitable method can change depending on the surface type (Park et al., 2017). The accuracy and resolution of the elevation model used for normalization also play an important role. If the selected resolution is too coarse, artefacts may appear in the image after the correction (see Richter, Louis and Müller-Wilm, 2012). Sola et al., 2016 have each identified different evaluation methods for evaluating the quality of a topographical correction in several studies.

VISUAL ASSESSMENT

The first indicator of the quality of the corrections is the visual evaluation of the images before and after the topographic correction (Sola et al., 2016). In-situ measurements are also possible. These are measurements on site, for a few selected points, with an optical spectroradiometer (Singh et al., 2015). However, these are associated with high time expenditure and high costs. Moreover, the performance cannot be differentiated according to different spectral bands (Park et al., 2017).

LINEAR REGRESSION AND CORRELATION COEFFICIENT

The most commonly used quantitative evaluation method is to consider the dependence between the cosine of the solar angle of incidence and the reflection values of each band. This can be measured by forming the correlation coefficient of all pixels in the image and/or by looking at the slope of linear regression. A lower dependency between the angle of incidence and reflectance would mean that the correction was successful. However, this assumption is not valid for areas where slope and exposure influence the distribution of land cover. In such areas, a certain residual correlation between the angle of incidence and reflection must be expected (cf. also there; Sola et al., 2016). Instead, however, it is also possible to view the relationship between the cosine of the angle of incidence and the reflection values of each band only for the pixels of certain land cover classes and not for the pixels of the entire image. The extent to which the variability of the reflection values within a land cover class has decreased can be calculated using the standard deviation and the coefficient of variation of the reflection. After the topographic correction, a higher homogeneity of the land cover is to be expected, as the radiometric variations caused by the topography are minimized within a class by normalization. This evaluation method is one of the most objective evaluation methods.

4.1.3.3 Implementation and Results of Benchmarking

Two methods have been compared and analysed, i.e. self-calibrating topographic normalisation from JR-IMPACT software and topographic correction within Sen2Cor software. The analysis was based on reference land cover type data on tree species and different Digital Surface Models (DSMs) as input, i.e. SRTM 90m, ALOS DSM 30m and LiDAR10m. First, the results are evaluated with visual interpretation and second statistical parameters are derived and analysed.

As input image, a Sentinel-2A atmospheric corrected image with Sen2Cor from 13.08.2015 Level-1C covering the granules 32TPT/32TQT was selected, which covers different elevation zones. The differentiation of the tree species types is analysed using separability distance measures, i.e. Jeffries Matusita (JM). Following combinations are investigated in order to assess the topographic methods and the used DEMs:

Table 4-2: Overview of the used combinations.

Image	Atm. Correction	Topo. Correction	Used DSM
o.A.	No atm. correction	No topographic correction	-
o.T.	Sen2Cor	No topographic correction	-
Impact 0.9	Sen2Cor	Impact	10m LiDAR DSM
Sen2Cor	Sen2Cor	Sen2Cor	90m SRTM
Imp.SRTM	Sen2Cor	Impact	90m SRTM
Impact 1.0	Sen2Cor	Impact	10m LiDAR DEM
ALOS DSM	Sen2Cor	Impact	30m ALOS DSM

For the comparison of the various results, it was decided to compare cosine of the sun angle with the reflectance values of each band. The correlation coefficient is calculated and the slope of the linear regression line evaluated. It is assumed that the correction is successfully applied if the interdependence of the two variables is low. However, it has to be noticed that the two parameters slope and exposition could bias the results, showing a higher correlation than expected. For the assessment of the land cover variability, the statistical measures standard deviation and coefficient of variation are used. It is assumed that the reflectance will become more homogeneous after the normalisation due to the reduction of the radiometric variation.

Preconditions are to be set before the investigations have been performed. Not all forest samples from the reference can be used for the investigations due to following reasons. Forest sites with crown coverage of less than 60% show much influence from other surface classes, e.g. bushes, grass or bare soil, and thus excluded. Secondly the classes mixed forest, fir and pine are not used due to their high spectral variability which could bias the results in the calculation. Another factor influencing the reflectance values is the age of the trees. In order to avoid a mixture of the age classes, it is necessary to split them into two separate classes: old and young.

REFERENCE AREAS

For the analysis, the reference areas are sorted out according to the above-described requirements. Altogether 138 samples were used for the analysis. Table 4-3 illustrates the number of samples for each forest type and the corresponding number of pixels.

Table 4-3: Overview of the used classes and number of samples/pixels.

Species Type	Number of Samples	Number of Pixels
Spruce old	34	1680
Spruce young	27	1476
Broadleaf old	32	1768
Broadleaf young	24	1101
Larch old	21	1033

VISUAL ASSESSMENT

In mountainous areas, the topography causes different illumination on slopes depending on their exposition. In general, reflectance values for land cover classes on north oriented slopes are lower than reflectance values on south oriented slopes. This rationale creates a 3-dimensional effect based on the dark and bright slopes, which gives a distinct spatial impression to the observer (see Figure 4-11: images o.A. and o.T. products are explained in Table 4-2: Overview of the used combinations.). Thus it is assumed that the loss of the 3D effect and an equalized illumination within a scene is an indicator for a successful topographic correction (see Figure 4-11).

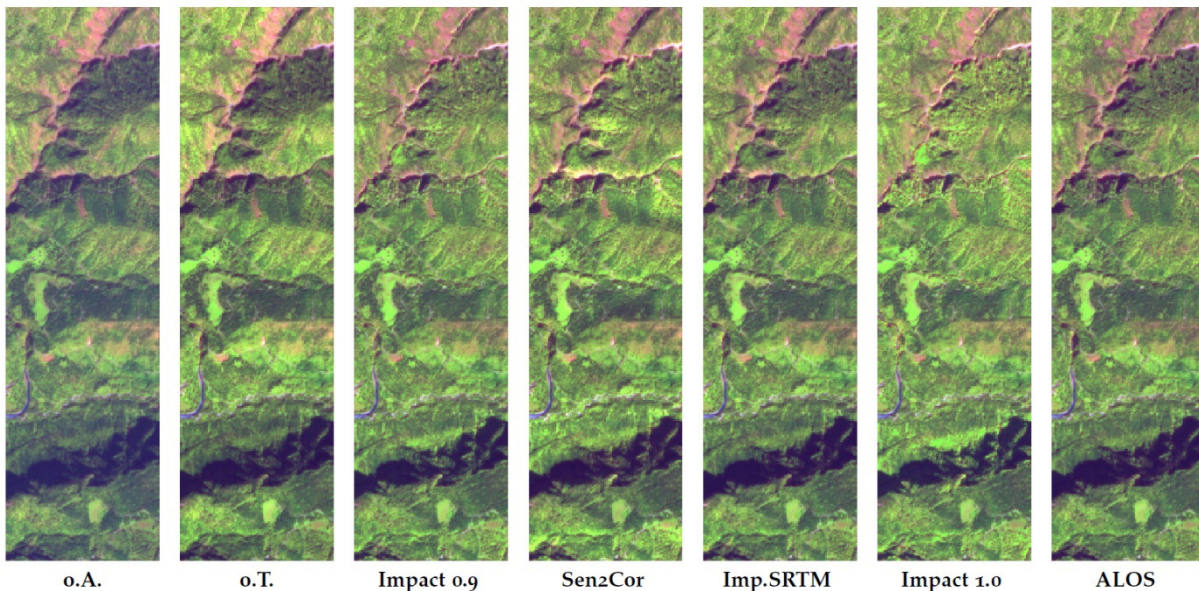


Figure 4-11: Example showing the various images before and after topographic normalisation (see also Table 1).

The relationship between the cosine of the sun angle and the image reflectance values is significant before the topographic correction. In order to analyse this relationship, it is necessary to calculate the variables such as regression line, regression coefficient and correlation coefficient.

LINEAR REGRESSION

In a first approach, the linear regression is calculated and compared within the data sets, i.e. origin data sets without topographic correction versus the in Table 4-2 listed topographic corrected images. The rationale behind this approach is based on the assumption that after the topographic correction the slope of the regression line equals 0. The relief of the terrain should not influence anymore the reflectance values within the scene. This ideal case is not fully realistically to be achieved owing to natural variation properties of forest stands on one hand and the selection of reference areas on the other hand. That means in a certain class the reference areas to be used for the calculation could be more heterogeneous than in another class. It can be stated, that after a successful topographic correction the slope has to become flat. An example is displayed in Figure 4-12.

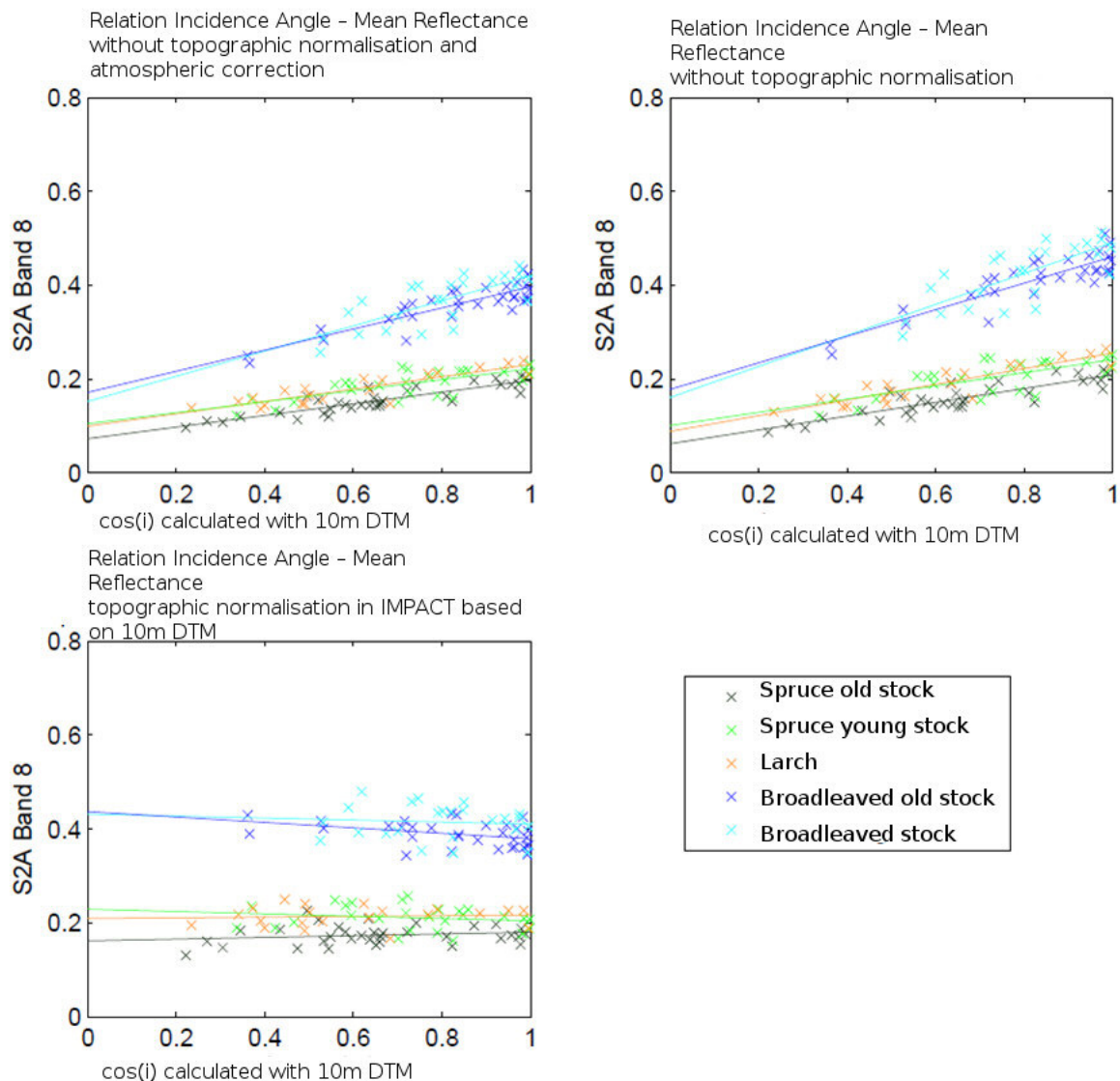


Figure 4-12: Example showing the regression line before and after topographic normalisation (on top 2 before and below diagram after correction).

In Figure 4-12 the diagrams on the top show the regression lines representing the two input scenes, without any atmospheric or topographic correction (left) and with atmospheric correction (right). The diagram on the bottom displays the regression lines after the topographic correction using IMPACT with 10m DSM. It can be observed that the reflectance of broadleaf classes or the younger tree types is higher than the coniferous classes or older stands. Two effects can also be observed after the topographic correction. The classes can be over-corrected (negative line) or under-corrected (positive line) after the topographic normalisation. In Figure 4-13 a comparison of the five image derivatives can be seen.

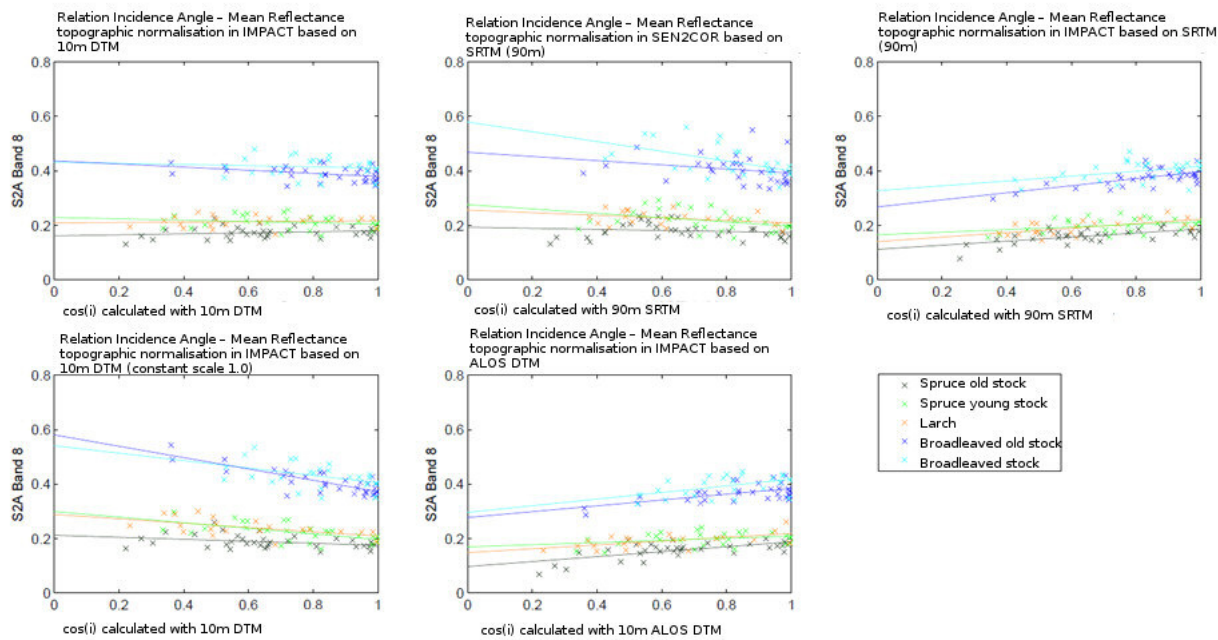


Figure 4-13: Regression lines after topographic normalisation using different software packages and DEMs.

In Figure 4-14 the slopes (beta1) of the regression line are illustrated with bar diagrams. It can be observed that for the Impact0.9 results the slopes in all bands are low. The Sen2Cor image shows higher values for the young stands and the slope is tending towards negative values. For the SRTM and ALOS images similar results with higher values can be observed and show an over-correction. This fact indicates a strong influence of the DSM. Generally, the broadleaf classes show higher negative slopes than the other classes.

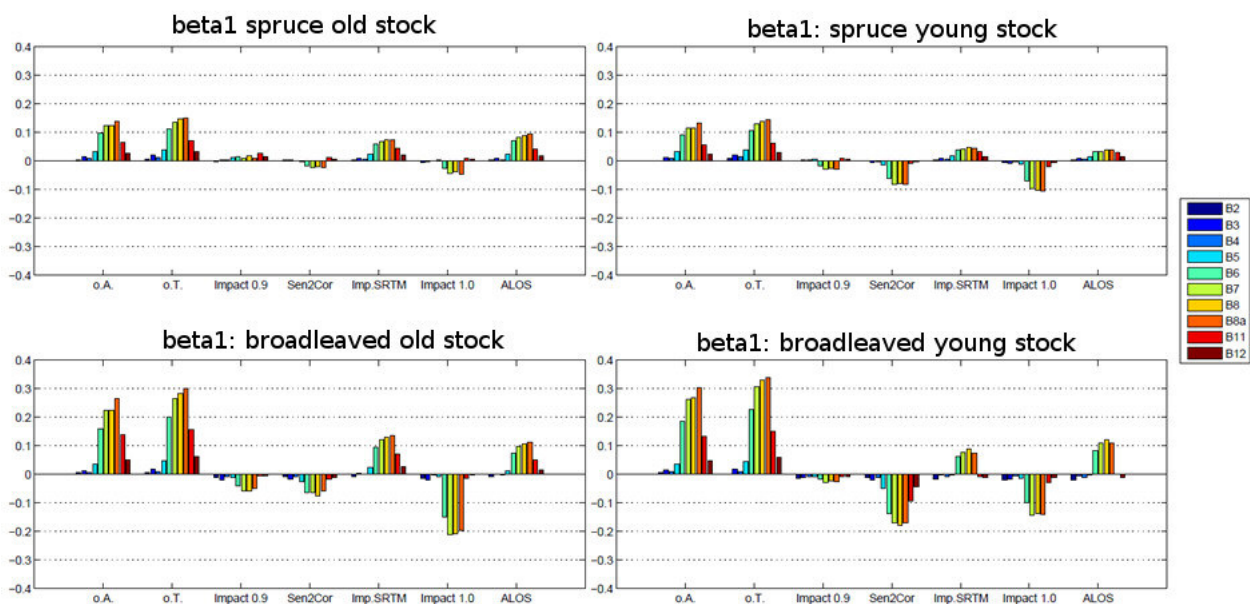


Figure 4-14: Bar Diagrams showing the slope (Beta1) of the regression line.

Another statistical value for the assessment of the analysis is the p-value which is to be used to confirm the null hypothesis or reject it. The null hypothesis is defined as the correlation between $\cos(i)$ and *reflectance values*. That means, after a successful topographic correction the null hypothesis should be rejected (p-value advances to 0, the probability of error = 5%), meaning that no topographic effect from the terrain can be observed. For the Impact0.9 image, the null hypothesis can be confirmed. For the Sen2Cor image, the null hypothesis is confirmed except for the class Broadleaf young. For this statistical parameter, the topographic correction for both images can be considered successful. For the images Imp.SRTM, ALOS and Impact1.0 the null hypothesis is rejected, meaning that the topographic correction cannot be considered as successful.

However for this investigation is also important to analyse the results using the correlation coefficient (between 0 and 1) of $\cos(i)$ and *reflectance values*. Looking at the two input images in Figure 4-15 it can be seen that both show a high correlation coefficient, which is expected because the topography is not corrected. Also for the images Imp.SRTM, ALOS and Impact1 the correlation coefficient is rather high. For the two other images Impact0.9 and Sen2Cor, the correlation coefficient is rather low, confirming again a successful correction.

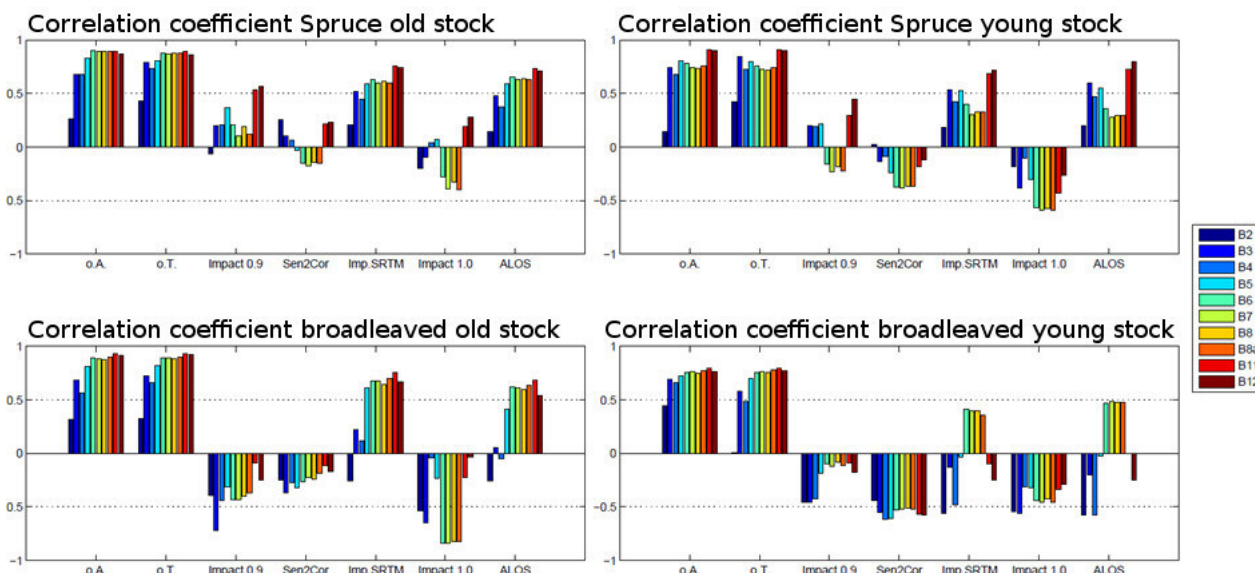


Figure 4-15: Bar Diagrams showing the correlation between $\cos(i)$ and *reflectance*.

4.1.3.4 Summary and Conclusions

Comparing the topographical correction of the Sen2Cor processor with the one of the IMPACT software (each using the 30m SRTM) different results are reached depending on evaluation method.

The visual comparison shows that after the normalisation in Sen2Cor over-corrected images are obtained, while after the normalisation in Impact a slightly under-corrected picture is obtained. The same result is reached by considering the correlation between the cosine of the incidence angle and the reflectance. The decrease of variation within a class is higher after the normalisation in IMPACT than after the correction in Sen2Cor.

Furthermore, corrections with elevation models of different spatial resolutions have been performed. With the 10m elevation model, an improvement of the correction because of the higher resolution has been reached compared to the one performed with the 90m SRTM. No improvement can be detected

with the 30m ALOS DSM. The evaluation results with the 30m ALOS and the 90m STRM elevation model are very similar. Looking at the two corrections performed in IMPACT, each with a different scaling factor of the Minnaert constant it can be seen that setting the scaling factor to "1" leads to an over-correction. With setting the factor to "0.9" better results are achieved.

One big limitation is the quality of the DEM, the current L1C DEM (SRTM 90 m) maybe not good enough and there is no possibility to use another DEM within the Sen2Cor package. The main issue with the topographic normalisation is the over-correction of south facing slopes. From the analysis, we conclude that topographic normalization should be applied in hilly to mountainous terrain for the ECoLaSS demonstration site production. The DEM with the highest spatial resolution should be used. Therefore, we would recommend using topographic normalisation tools which allow the user to define their own DEM, if only the SRTM 90m model is available Sen2Cor topographic normalisation also provides acceptable results.

4.1.4 Benchmarking of candidate approaches for Geometric consistency

Pre-processing of EO data used in time series analysis applications is one of the most crucial issues to guarantee reliable and meaningful results, especially so, when data from different sensors are used. In ECoLaSS the imperviousness, grassland, forest and agriculture applications may use various combinations of Sentinel-2, Sentinel-1 and Sentinel-3 data. Therefore, it is essential to analyse the overall data quality of the input data and the initial geometric shifts and radiometric differences between image data from the same sensor (e.g. from neighbouring orbits) and from different sensors. The results from this analysis form the basis for the pre-processing improvements applied in the ECoLaSS pre-processing workflows.

4.1.4.1 Description of Candidate Methods

SENTINEL-2 GEOMETRIC ACCURACY TESTS

Currently, Sentinel-2 data is delivered as orthorectified images only. Orthorectification at ESA is performed based on a medium resolution PlanetDEM from PlanetObserver. In mountainous areas, geometric accuracy strongly depends on the quality of the DEM and the satellite viewing angle. Since the accuracy of ESA's DEM at the ECoLaSS test sites is not known to the consortium, some geometric accuracy tests were performed in order to quantify the DEM related location errors in alpine settings. In addition to DEM related errors, we also expected to find linear location errors between Sentinel-2 images for adjacent orbits. In addition to DEM related errors, a slight yaw drift was detected for Sentinel-2A and corrected end of May 2016. Images processed before June 2016, therefore, have slightly higher geometric mislocation errors. A list of known quality issues with Sentinel-2 data is published in the Sentinel-2 data quality report (<https://sentinels.copernicus.eu/web/sentinel/missions/sentinel-2/data-quality-report>). As of summer 2017, when the first pre-processing chains were defined in the ECoLaSS project, Sentinel-2 data from neighbouring orbits were not co-registered by tie-points. In near future, images will be matched to a Sentinel-2 Global Reference image (Dechoz et al., 2015). This will significantly reduce the geometric location errors between images of overlapping orbits.

4.1.4.2 Benchmarking Criteria

SENTINEL-2 LOCATION ERRORS

Until the Sentinel-2 global reference image is available, it could be necessary for many change detection algorithms to register all Sentinel-2 images to a master reference scene in order to guarantee sub-pixel positioning accuracies. This is especially true when data from different relative orbits is used. However, since prototyping in ECoLaSS is only expected to start in 2018, the consortium will most likely demonstrate their services based on future Sentinel-2 imagery that is already co-registered to the global Sentinel-2 global reference image.

In order to estimate the effect of Sentinel-2 geometry errors on ECoLaSS products and services, we investigated the location errors in flat and mountainous terrain at one of the ECoLaSS test sites.

TEST SITE SELECTION FOR GEOMETRIC ANALYSIS

The Central test site, covering parts of Austria and Germany, was chosen to analyse the geometric quality of the input EO data. It is characterized by both topographically flat and mountainous terrain and it covers all land cover classes to be mapped in ECoLaSS – i.e. imperviousness, grassland, forest, agriculture. A mountainous test was seen as being important for the accuracy analysis since Sentinel-2 data is delivered as orthorectified image data and non-linear geolocation errors related to the underlying DEM used by ESA during orthorectification also need to be assessed.

4.1.4.3 Implementation and Results of Benchmarking

GEOMETRIC QUALITY TESTS

In order to separate the different error components (DEM related, orbit related – non-linear, linear), geometric tests were performed at the Central test site. In a first analysis, 9 Sentinel-2 granules with mostly flat terrain were matched to a Sentinel-2 master scene using a linear matching approach based on an automated point matching using areal mutual information as for cost function. The current relative offsets at the test site are on the order of 0.1-1.3 pixels, with a mean offset of 1.8m in x and 8.9m in y-direction between all Sentinel-2 images illustrated in Figure 4-16. However, maximum mean shifts between overlapping relative orbits are up to 22m in y-direction.

name	orbit	X [m]	Y [m]	#points
2015-07-31-S2	1	-0.384	9.474	844
2015-08-07-S2	2	0.087	8.087	1100
2016-02-06-S2	1	2.666	8.728	1087
2016-03-14-S2	2	-1.430	-7.938	1107
2016-03-17-S2	1	4.478	8.674	102
2016-03-27-S2	1	3.713	12.991	1026
2016-04-13-S2	2	-2.060	-9.667	1134
2016-06-22-S2	2	-2.071	5.239	987
Ref 2016-06-25-S2	1	-0.067	0.180	1134
Abs. mean		1.773	8.875	1049
Max. mean shifts		5.784	22.465	
std		2.474	8.040	93

Figure 4-16: Geometric accuracy analysis for Sentinel-2 data at a flat terrain test site

These values are similar to those expected and reported by ESA (Languille et al., 2015); “1st Sentinel-2 Validation Team Meeting” at ESA in Nov. 2016) and to findings of other studies. A recent study has analysed the absolute location error of Sentinel-2 in Austria by matching Sentinel-2 and the Geoland Basemap Orthophoto of Austria (Pandžić et al., 2016). This reference imagery was acquired with 20cm resolution and orthorectified with a 10m LiDAR DSM. The authors report a mean shift of 0.6 pixels measured by estimating the offset of line segments at a test site in Austria. At a test site in Serbia a larger mean registration error of 1.27 pixels was found (Pandžić et al., 2016).

In a second analysis, 19 Sentinel-2 granules with mostly mountainous terrain were matched to a Sentinel-2 master scene using again a linear matching approach based on an automated point matching using areal mutual information as for cost function. Results are presented in Figure 4-17. While the mean errors of 4m in x and 5.2m in y are similar to those found in topographically flat areas, maximum local non-linear shifts of more than 30m were observed in the mountainous areas. This is similar to mislocation errors described for alpine areas of Switzerland and Norway (Kääb et al., 2016). The authors report significant DEM errors that propagate into locally varying lateral offsets in the images of up to

several pixels with respect to other georeferenced data or between Sentinel-2 data from different orbits. Such a shift of up to 30m or 3 pixels makes pixel-based change detection techniques very difficult in mountainous environments. The main reason is assumed to be DEM errors in the PlanetDEM used by ESA during orthorectification. Ressl and Pfeiffer have found that the PlanetDEM has an irregular tile structure with systematic height errors in the Alps of up to 50m (1st Sentinel-2 Validation Team Meeting": [last accessed Sep 28, 2017]). The modelled geometric accuracy of Sentinel-2 data is still reported to be very high, with 95% of all errors between -3.5 and +3.5m, but significantly larger errors are expected for isolated mountain regions.

name	orbit	X [m]	Y [m]	#points
20160304	2	-3.801	9.443	745
20160307	1	-6.765	3.511	1564
20160308	2	-3.801	9.443	745
20160317	2	1.498	2.552	832
20160811	1	-6.947	8.304	1274
20160912	1	-2.521	9.090	958
20160215	2	1.670	10.882	780
20151218	1	-0.386	-2.998	1259
20151221	2	1.421	11.573	619
reference 20151228	1	0.002	0.001	1616
20160320	2	2.822	10.078	808
20160804	1	-3.265	2.269	533
20160824	1	-4.935	-2.277	809
20160827	2	-6.580	3.625	943
20160903	1	-5.204	0.212	744
20160923	1	-7.039	0.761	1255
20161013	1	-5.829	3.445	1243
20161016	2	-5.121	3.257	321
20161023	1	-7.803	6.359	1229
20161115	2	-0.509	4.327	850
Abs. mean		3.935	5.249	956.350
Max mean shifts		10.625	14.571	
std		3.416	4.454	338.377

Figure 4-17: Geometric accuracy analysis for Sentinel-2 data at a mountainous test site

It is expected that in early 2018, ESA will release its Sentinel-2 global reference image (Dechoz et al., 2015) which in principle is similar to the Landsat GLC and that all new Sentinel-2 will then be co-registered to this reference image. Most linear shifts between individual Sentinel-2 images should then be eliminated.

For analysing the non-linear errors that result from DEM errors during the orthorectification process we applied a full disparity matching at an alpine test site based on the same 20 Sentinel-2 scenes used for the linear matching tests. The full disparity matching uses a cross-correlation as cost function in image matching to derived image disparities. These disparities are then used for non-linear co-registration. Figure 4-18 shows two examples of the disparity maps. We found that in mountainous terrain, the linear component alone is not sufficient to correct the observed mislocations as both the linear and the non-linear component have approximately the same magnitude. A linear workflow will therefore not be able to account for the non-linear DEM related errors.

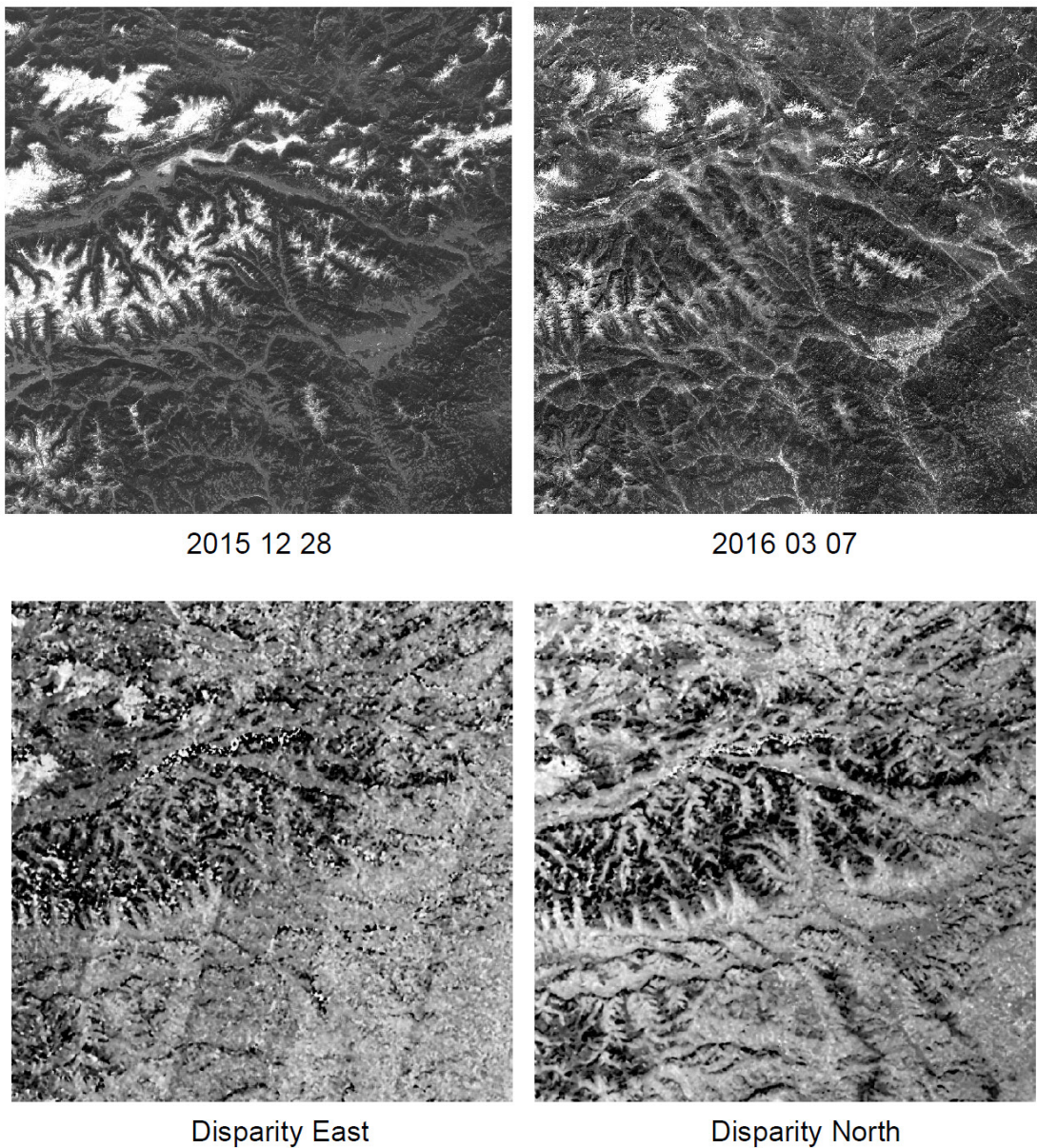


Figure 4-18: Two Sentinel-2 images from the mountainous test area and disparity images in East and North between both images

4.1.4.4 Summary and Conclusions

While full disparity matching algorithms can account for the non-linear shifts, they consume a lot of computational resources and processing time. In a pan-European approach, this would be a strong limiting factor for any update services. The final co-registered images will also show radiometric distortions in areas of large geometry shifts which can make a classification or change detection impossible in these adjusted areas. Hence, the overall benefit of geometrically adjusting Sentinel-2 imagery in mountain areas can be questioned. The best solution would be, to use a better DEM during orthorectification at ESA. Since non-orthorectified Level-1B data will not be made available to the scientific community by ESA, the ECoLaSS consortium will have to work with the available orthorectified Level-1C datasets. With a growing number of DEM related error reports, there are plans at ESA for integrating better DEMs during the orthorectification process, with Norway being a first test region. Whether and when these improvements will happen at pan-European scale is currently not known to the

consortium. If improved orthorectified Sentinel-2 data becomes available during project run-time, we will include it in the ECoLaSS processing chains. Since ECoLaSS prototyping will only start in 2018, we suggest not including a specific linear co-registration approach in the current ECoLaSS Sentinel-2 pre-processing chain. During the test phase used for algorithm development, the observed linear shifts are not so critical to require a co-registration procedure.

4.2 Benchmarking of methods for pre-processing of SAR time series

Processing methods for SAR time series in literature are focusing on a) benchmarking of existing / currently developed algorithms and tools, b) implementation of spatio-temporal noise filtering tools optimized for Sentinel-1 time series, c) enhanced automated detection and correction of atmospheric influences, d) cluster processing to reduce processing time, e) and derivation of multi-temporal metrics [AD04]. Therefore, the following sections provide methods and benchmarking thereof, focussing on the topics of radiometric calibration, speckle noise reduction and interferometric coherence estimation of SAR time series data.

4.2.1 Benchmarking of candidate approaches for radiometric calibration

As mentioned in Chapter 3.2.2, SAR intensity values can be processed to different radiometric calibration levels. These calibration levels can correct for backscatter differences related to local incidence values and thus can make data from different orbits comparable. Here, we test different processing levels for their suitability in the ECoLaSS project. Different calibration levels are calculated and tested for their performance to level backscatter values of individual land cover classes and for images of different orbits.

4.2.1.1 Description of Candidate Methods

Standard radiometric calibration levels for SAR data are beta, sigma and gamma nought. Each applies different radiometric corrections. In addition, removal of terrain effects can be applied, which is sometimes termed SAR terrain flattening.

We test the following calibration levels: Beta nought gives values per unit area in slant range geometry. Sigma nought values are per unit area in ground range, so corrected for local incidence angle. Gamma nought values are per unit area perpendicular to slant range. Flattened gamma nought is additionally corrected for local terrain effects based on a DEM (cf. Small, 2011). Gamma nought is usually used when data from different orbits are combined, since local incidence angles vary from different orbits. We use the SRTM4 DEM as elevation source.

4.2.1.2 Benchmarking Criteria

First, only a visual analysis of output results was performed. Then similarity studies were performed among land cover types at varying incidence angles and for backscatter values in overlapping images from different orbits. The testing criteria were:

REDUCTION OF TERRAIN EFFECTS

The similarity analysis of backscatter values for an identical land cover class at different local incidence values. A number of points for different land cover classes have been derived from existing land cover classifications. The spreading of values has been estimated for the forest class, each calibration level, and ranges of local incidence values. A lower spread of backscatter values is considered better for subsequent land cover information extraction.

SIMILARITY OF IMAGE BACKSCATTER VALUES FROM OVERLAPPING ORBITS IN OVERLAPPING AREAS

Image differencing of images from different orbits is applied to image data processed regarding all above mentioned calibration levels. Remaining differences are likely to be remnants of local incidence values related to either topography or orbital imaging geometry. Lower difference values between adjacent orbits are considered better for consecutive homogeneous land cover classifications.

4.2.1.3 Implementation and Results of Benchmarking

Beta, sigma and flattened gamma nought images from two overlapping orbits were calculated for an alpine test area in the Central test site. An example is given in Figure 4-19.

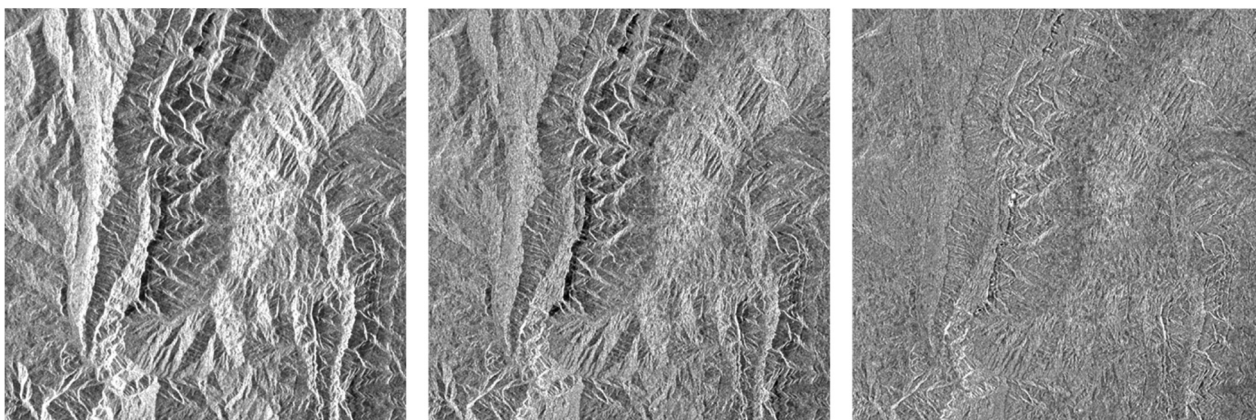


Figure 4-19: different SAR radiometric processing levels: left: beta naught (slant range geometry), middle: sigma naught (corrected for local incidence angle), right: flattened gamma naught (terrain corrections according to Small, 2011).

Difference images were calculated for overlapping areas. For grassland and forest classes which are the most common classes in alpine terrain, AOIs were selected from different local incidence angles and backscatter values were compared.

4.2.1.4 Summary and Conclusions

Beta nought images in alpine settings show strong local incidence related artefacts in backscatter values and are thus unsuitable for pan-European land cover classification. In sigma nought imagery most, but not all, terrain effects could be removed. We find the SRTM4 model is not accurate enough for a full removal of terrain effects. However, it is the only freely available DEM currently available at pan-European scale. With sigma nought processing, imagery from different orbits cannot be used jointly because backscatter values still differ strongly among the different orbits. Flattened gamma nought imagery shows best results for terrain correction and for the similarity of imagery from different orbits. When incidence angles are too steep values are still unreliable. We therefore recommend using flattened gamma nought SAR backscatter data for the ECoLaSS demo site processing if data from different orbits is combined, but to eliminate areas with large incidence angles above 70°.

4.2.2 Benchmarking of candidate approaches for speckle noise reduction

Noise reduction is an important pre-processing step for SAR imagery based land cover classification. In addition to multi-looking, which is already applied to GRD images, SAR speckle filtering can be used to reduce speckle noise in SAR imagery. Common SAR speckle filters include Lee filter, Frost filter, Kuan filter, Gamma-Map filter and multiresolution speckle filters. An overview of proved standard SAR speckle filters is provided in Lee, 1994. However, for time series of SAR data, multitemporal SAR filtering is the

most widely used procedure for noise reduction (cf. Quegan, 2000). Here, we present results from a test of different filters for their suitability for land cover classification.

4.2.2.1 Description of Candidate Methods

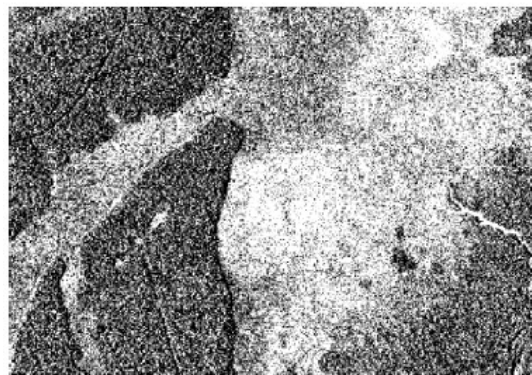
In a study on SAR filters different adaptive SAR, speckle filters were tested with respect to their suitability for land cover classification (Hoermann, 2011). In addition, a multitemporal SAR filter proposed by Quegan et al., 2000, was tested. Among the mono-temporal SAR filters the Frost-filter (Frost et al., 1981), Modified-Frost filter, Lee filter (Lee, 1980), Refined Lee filter (Lee, 1981), Kuan filter (Kuan, 1985), GammaMAP filter (Lopes et al., 1990), and a multiresolution filter (Meer et al., 1994) were compared. All filters were tested with different filter windows (3x3, 5x5, 7x7) except for the multiresolution filter which automatically adapts the window depending on local backscatter homogeneity. When working with multitemporal SAR data it is usually more efficient to use multitemporal noise filters. The multitemporal filter preserves or even enhances the separability of small targets while most mono-temporal and adaptive filters do not preserve the geometric detail of the image.

4.2.2.2 Benchmarking Criteria

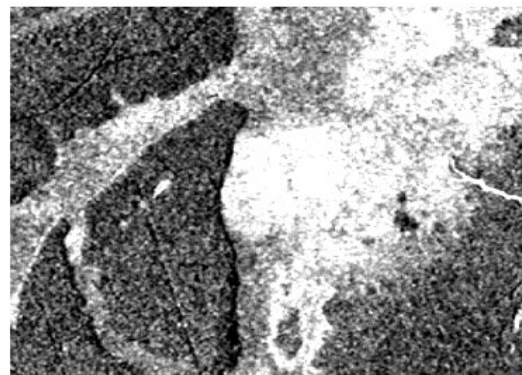
For estimating the quality of different SAR image filtering techniques both a visual qualitative analysis and a quantitative analysis have been performed. Land cover classification accuracies after filtering were compared both raster based on pixel level and by statistical cross-validation. Additional processing criteria were filtered window size (3x3, 5x5, 7x7), and processing unit (db vs. DN).

4.2.2.3 Implementation and Results of Benchmarking

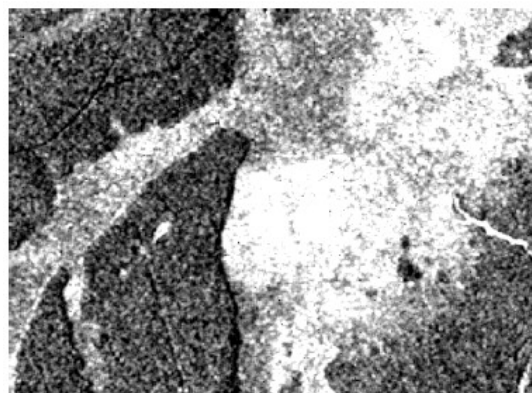
For a test area characterized by different land cover classes, images were pre-processed with different filters using JR RSG software. Most filters used here are also available in other (open-source) SAR software. The following figures (Figure 4-20; Figure 4-21; Figure 4-22) show examples of the different noise filtering results and examples of different filter windows. For larger filter windows, noise is reduced much stronger, but the image becomes blurred and does not preserve radiometric detail. Small targets are lost with large filter windows.



Ungefiltertes Bild



Frost 3x3

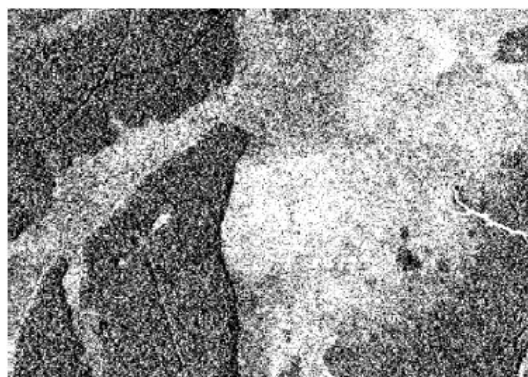


Modified Frost 3x3



Lee 3x3

Figure 4-20: examples of different adaptive SAR speckle filters



Refined Lee



Kuan 3x3

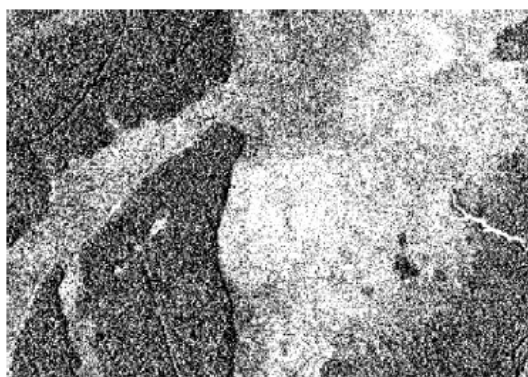


GammaMAP 3x3

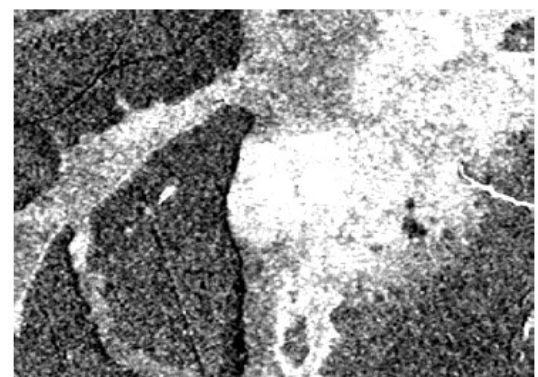


Multiresolution

Figure 4-21: examples of different adaptive SAR speckle filters.



Ungefiltertes Bild



Frost 3x3



Frost 5x5



Frost 7x7

Figure 4-22: Frost filter with different filter windows.

Six land cover classes (water bodies, wetlands, urban, forest, agriculture (vegetated), bare soil) were chosen for a simple maximum-likelihood based classification based on reference areas. Results were compared to classification results based on optical data.

The following figures (Figure 4-23, Figure 4-24, Figure 4-25) show the accuracies achieved with different filters and additional parameters (window size, a processing unit, spatial resolution). Best results were achieved with Multiresolution, Frost, and Modified-Frost filters, which have a strong smoothing effect. All filtered images show higher classification accuracies than the unfiltered image.

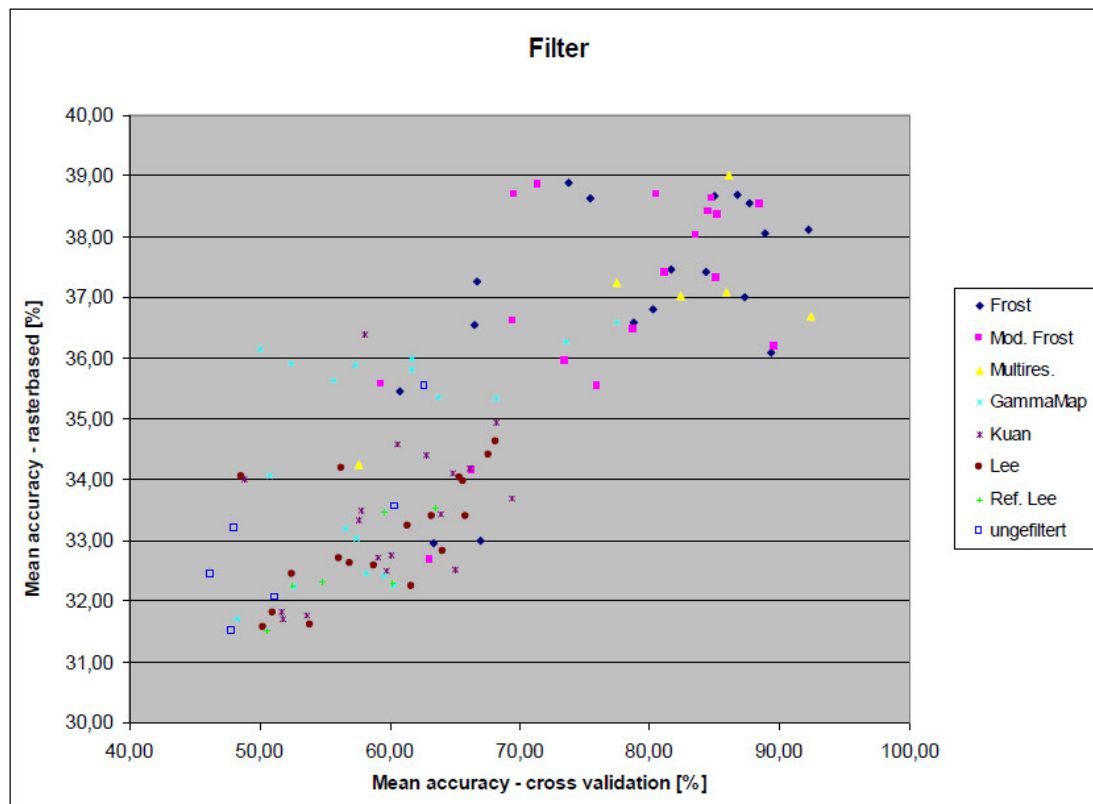


Figure 4-23: land cover classification accuracies achieved with different adaptive SAR speckle filters.

1	DN_15m_frost (3x3)	63,37
2	DN_15m_frost (5x5)	66,95
3	DN_15m_frost (7x7)	66,68
4	DN_15m_modified frost (3x3)	63,05
5	DN_15m_modified frost (5x5)	66,36
6	DN_15m_modified frost (7x7)	80,55
7	DN_15m_multiresolution	85,94
8	DN_15m_gammamap (3x3)	60,34
9	DN_15m_gammamap (5x5)	58,15
10	DN_15m_gammamap (7x7)	59,60
11	DN_15m_kuan (3x3)	65,06
12	DN_15m_kuan (5x5)	60,61
13	DN_15m_kuan (7x7)	60,12
14	DN_15m_lee (3x3)	52,53
15	DN_15m_lee (5x5)	58,87
16	DN_15m_lee (7x7)	64,13
17	DN_15m_refined lee	52,50
18	DN_15m_ungefiltert	51,25

Figure 4-24: cross-validation accuracies for land cover classification achieved with different adaptive SAR speckle filters and window sizes.

	Cross validation
Frost	78,64
Modified Frost	77,26
Multiresolution	80,32
GammaMAP	59,20
Kuan	59,95
Lee	59,34
Refined Lee	56,87
ungefiltert	52,76

Figure 4-25: Mean cross-validation accuracies achieved with different SAR speckle filters, window sizes, processing units and spatial resolutions.

Multi-temporal filtering is the most commonly used method for speckle noise reduction in multi-temporal SAR data stacks.

For a sequence of N registered multitemporal images, with intensity at position (x, y) in the kth image denoted by $I_k(x, y)$, the temporally filtered images are given by:

$$J_k(x, y) = \frac{E[I_k]}{N} \sum_{i=1}^N \frac{I_i(x, y)}{E[I_i]}$$

for $k = 1, \dots, N$, where $E[I]$ is the local mean value of pixels in a window centred at (x, y) in the image I.

(Cf. Quegan 2010; the same filter is used in ESA SNAP Sentinel-1 Toolbox)

The advantage of multi-temporal filtering is that it preserves or even enhances the level of geometric detail and increases the signal to noise ratio. Figure 4-26 shows an example of an unfiltered and a multi-temporally filtered seasonal mean image from a SAR stack covering one entire vegetation season. The

preservation of geometric detail is obvious and is beneficial for high resolution LC products and LC classes with small targets (urban built-up areas, urban vegetation).

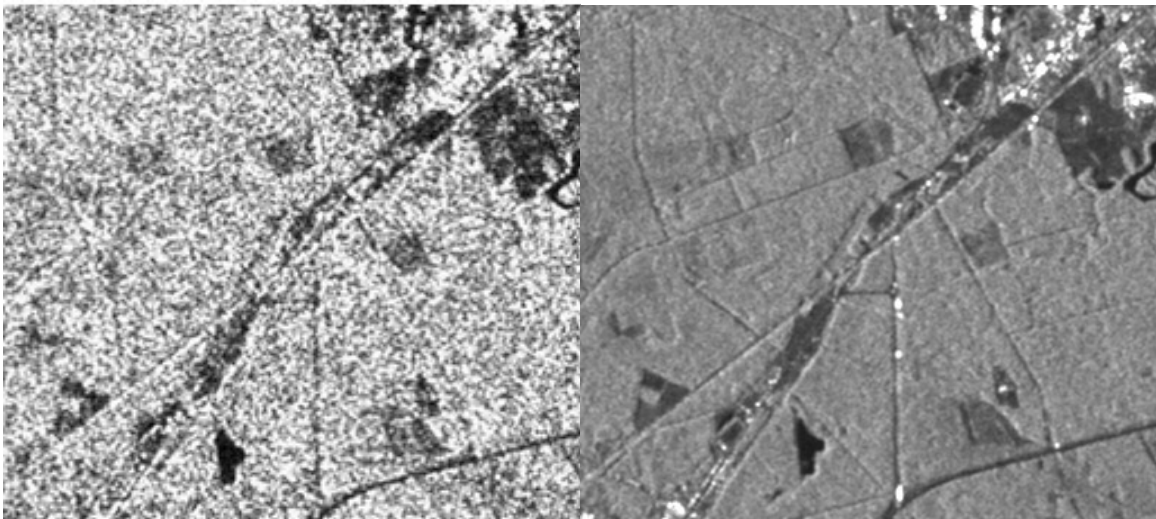


Figure 4-26: left: Single Sentinel-1 scene, unfiltered; right: Single Sentinel-1 scene filtered with MTF, 19 images, 7x7 window.

4.2.2.4 Summary and Conclusions

When working with single SAR images, adaptive speckle noise filters with strong smoothing effects, such as Frost, Modified-Frost and Multiresolution filter, usually show best results for overall land cover classification accuracies. However, geometric detail is lost due to blurring effects. When multitemporal SAR data is available multitemporal SAR filters are better suited for high resolution land cover classification with full resolution, e.g. is a 10m resolution for Sentinel-1 /Sentinel-2. Multitemporal filters, such as the one described by Quegan, preserve the radiometry while reducing noise and sharpening the image. The calculation of seasonal means further reduces noise and enhances class separability.

For ECoLaSS pre-processing, our analysis concludes that multitemporal SAR filters should be applied to pre-processed gamma nought data in DN processing unit. Multitemporal filters can be applied to the entire (or annual) image stack. Seasonal means and seasonal statistics further reduce speckle noise and should be used as input regarding SAR data classification of the HRL land cover classes. This will be analysed in WP 34 dealing with times series analysis.

4.2.3 Benchmarking of candidate approaches for interferometric coherence estimation

Interferometric coherence is a measure of decorrelation and can be used to separate different land cover classes. For vegetated areas decorrelation is very high and short-term coherence is required to map differences among vegetated areas. In this section, methods to calculate short-term coherence from Sentinel-1A and Sentinel-1B are tested, where different time windows are analysed by a simple evaluation of the best short-term coherence window. For the short term interferograms, coherent pixels are identified following the same strategy adopted in Pepe et. al. (2015) that is based on analysing the interferometric phase information within a boxcar averaging window.

4.2.3.1 Description of Candidate Methods

We calculate 6-day, 12-day and 18-day coherence products using a standard box car coherence estimation approach. The interferometric coherence is a statistical average. It requires averaging over many samples of the same distribution. A commonly used technique for this is the boxcar filter where

samples in a 3x3, 5x5 or 7x7 moving window are included in the coherence computation. The boxcar filter has the advantage of being simple to calculate, being very effective in speckle noise reduction and in preserving the mean value. Its deficiencies are a reduction of spatial resolution due to indiscriminately averaging pixels from inhomogeneous areas and thereby blurring edges and smearing point targets.

4.2.3.2 Benchmarking Criteria

The main focus is on determining reliable short-term InSAR coherence products. Those products can be derived from Sentinel-1 SLC data. In addition, different short-term coherence windows (6-day, 12-day, 18-day) are tested and analysed regarding their potential for land cover mapping.

4.2.3.3 Implementation and Results of Benchmarking

Testing was performed with Joanneum Research RSG software, more precisely the InSAR suite section. The InSAR coherence pairs were calculated for both available polarisations (VV and VH) and in two modes: First, the InSAR coherence was calculated between a master scene and all other scenes in the stack. The ideal master scene was chosen by the program without user input. A common master scene for all InSAR pairs within the same orbit is required. Thereafter, all short-term coherence pairs below a maximum temporal baseline (i.e. the difference between two dates) were calculated. Regarding the processing, 6-day and 12-day and 18-day coherence products were generated for two test sites based on Sentinel-1A and Sentinel-1B SLC imagery from March 2017-June 2017. Those two test sites are located in Central (Austria and Germany) and Belgium. Currently, the coherence estimation has been performed for an 80*80m output resolution.

Figure 4-27 shows the orthogonal baselines (the temporal and spatial differences) between the recorded scenes. The left figure shows the baselines for all six-day interval scene pairs, the right depicts the spatial and temporal distances of all scenes to the master scene. The temporal and spatial baselines indicate the scene pairs for which a coherence image was calculated. Each blue line in Figure 4-27, therefore, stands for one result image. The temporal baseline is noted in the number of days a scene is away from the master scene. For classification purposes it is reasonable to calculate the mean of multiple consecutive coherence pairs rather than a longer-term coherence.

From the images relative to the master scene a comparison of reasonable time intervals to be used in classification can be calculated.

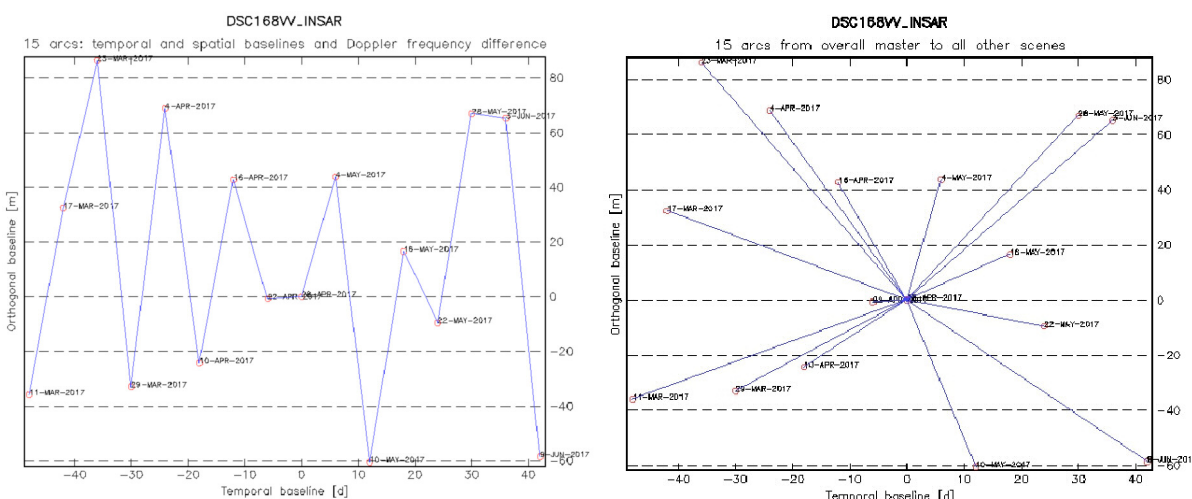


Figure 4-27: calculation of orthogonal baselines for 6-day coherence pairs (left) and for all common-master pairs (right) for Belgium test site

Example of the resulting images and their extent can be seen in Figure 4-28. Adjacent Sentinel-1 SLC products (North/South or adjacent orbit) are combined during processing to cover the entire test site area.

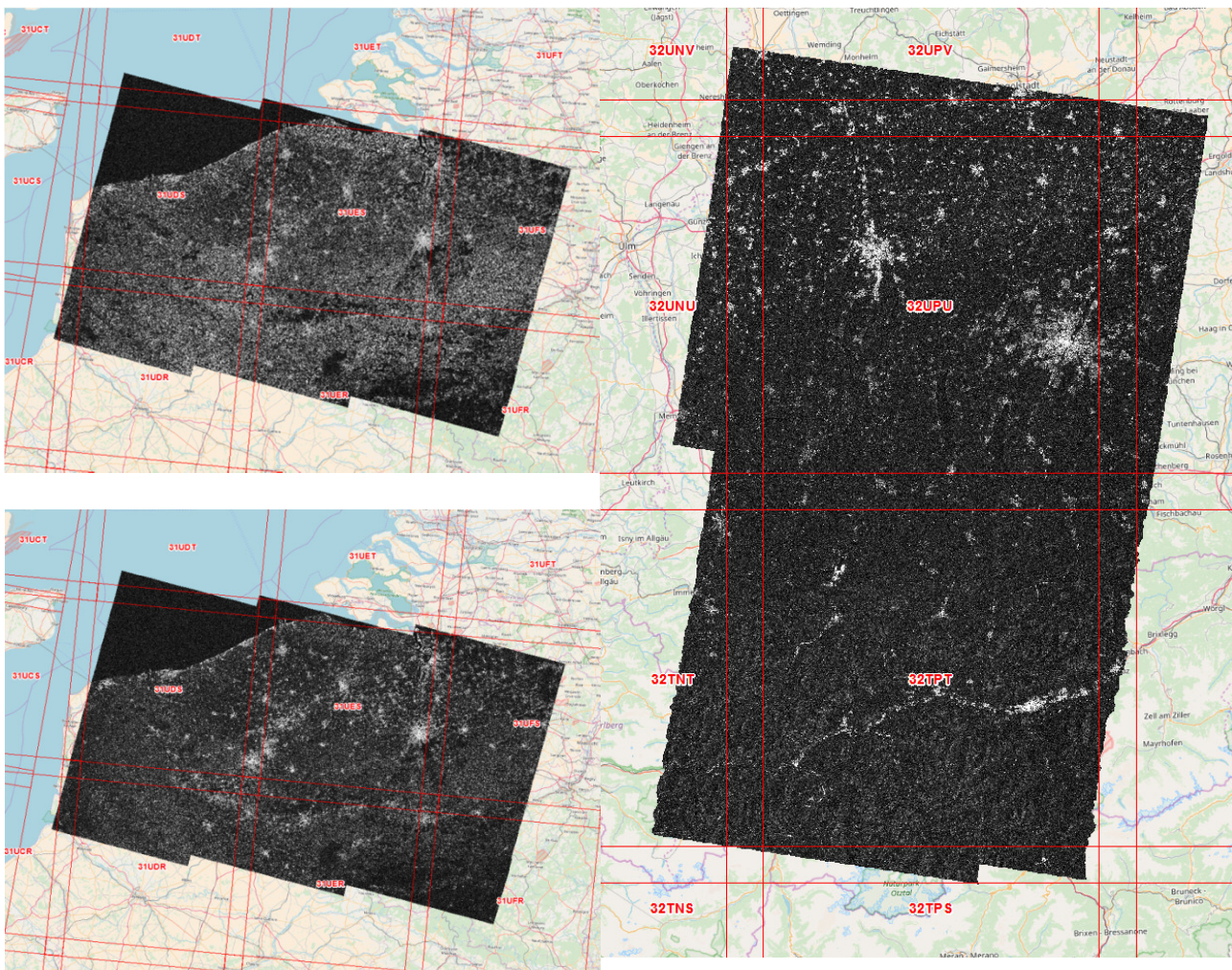


Figure 4-28: Coherence product examples from the Belgium and Central test site.

The following Figure 4-29 shows examples of 6-day, 12-day and 18-day Sentinel-1 coherence and its decorrelation over time at an urban area in the Central test site. The master scene was April 28th, 2017. The decorrelation becomes visible in the enhanced noise in the 12- and 18-day coherence images (centre and right) compared to the 6-day coherence (left). This occurs as a result of gradual changes in volume scattering of the vegetated area caused by e.g. plant growth and mowing events. Only entirely stable elements (urban built-up areas) on the surface show no or little decorrelation over long time periods. The 6-day coherence image also shows high coherence values for agricultural fields and other non-vegetated areas. In the 18-day coherence image, only the built-up areas feature high coherence values while agricultural areas are no longer distinguishable. For identifying urban areas longer coherence windows might, therefore, be more useful. For agricultural applications, short term coherence of 6-days or different images of 18-day coherence and 6-day coherence might be more useful. For other land cover classes, coherence seems rather irrelevant. Forests for example show very low coherence values with a high level of noise.

Sentinel-1: 6-day coherence

Sentinel-1: 12-day coherence

Sentinel-1: 18-day coherence

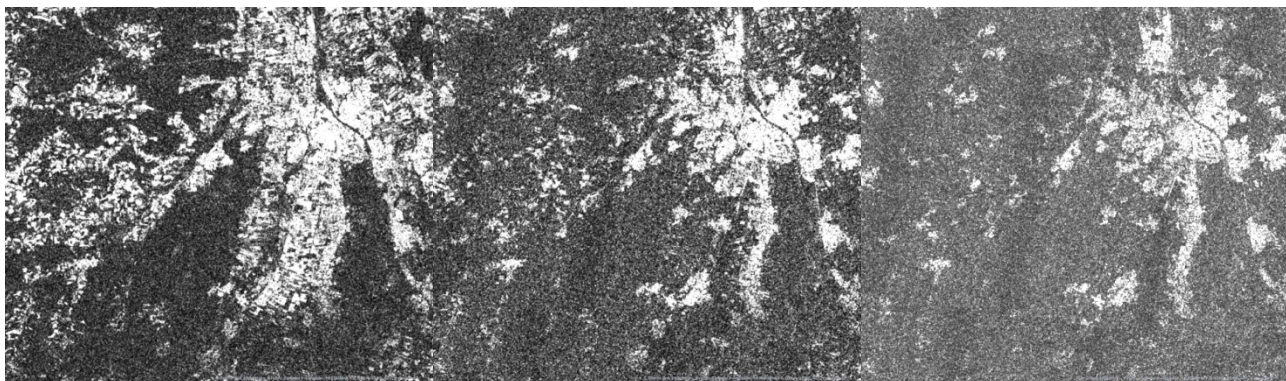


Figure 4-29: Examples for VH coherence decorrelation over time, Central test site; stack: March – June 2017 (master 28.04.2017)

4.2.3.4 Summary and Conclusions

We have shown that joining Sentinel-1A and Sentinel-1B SLC data in order to derive short-term InSAR coherence is possible using our own JR in-house software RSG. However, an analysis of available SAR software packages (see chapter 3.2.4) has shown that most do not support short-term coherence estimation directly. Additional programming effort is therefore required.

Short term coherence seems to be of interest for agricultural applications (bare field conditions) and possibly grasslands, e.g. detection of mowing events. Longer coherence time intervals could be of interest for medium resolution detection of urban built-up areas.

Whether coherence data adds any significant additional value for HR land cover classification compared to using only filtered GRD backscatter data will need to be investigated in phase two when thematic classification chains are developed. If benefits are only small, we recommend not going through the additional effort of processing SLC data and InSAR coherence. Calculating these products on the pan-European level for an entire year or more will consume a lot of time and processing power which might not be warranted. Final conclusions are expected after phase two.

5 Pre-processing of ECoLaSS test sites

5.1 Pre-processing of optical data

The main challenge requested as research need is the adaptation and up-scaling of current processing lines from local level to a continental level. Accordingly, a large volume of data should be pre-processed, to be able to produce data composites and derive calibrated and validated variables. To assess the required infrastructure, necessary to process high volume of optical Sentinel-2 data streams the Sen2Cor software which is provided by ESA has been used. The processor performs reasonably with the given input data, the software implementation and handling is user-friendly and it is open for public usage. MAJA might achieve better cloud masking results, but due to the licence and implementation issues the software cannot be used in commercial projects such as HRL production.

Following Figure 5-1 shows the general pre-processing workflow implemented by JR within the IMPACT software environment. A comparable workflow is implemented at DLR.

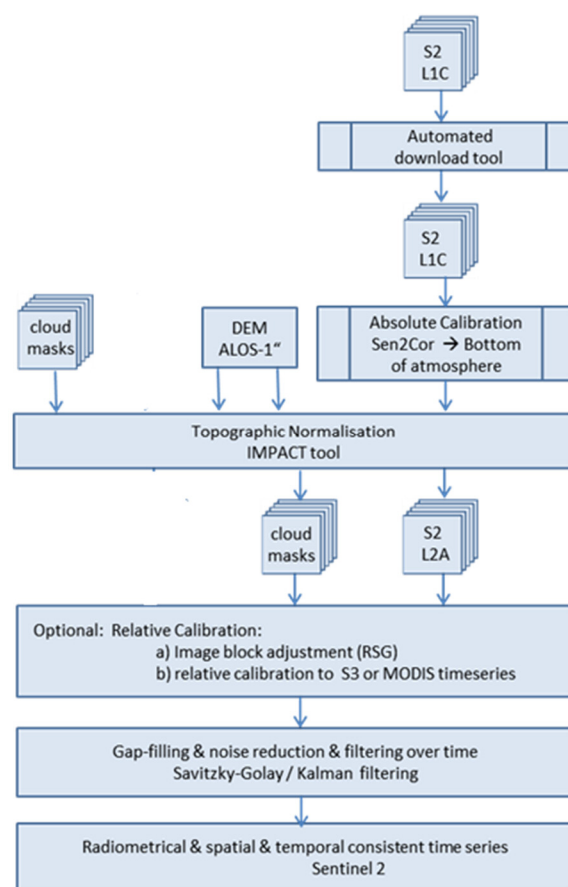


Figure 5-1: Pre-processing of optical time series - workflow

The Sentinel-2 Level-1C products are automatically downloaded from the CopHub (<https://cophub.copernicus.eu/dhus/>) and serve as input data stream for the 'Sentinel-2 Reflectance Data Processing' tool implemented by JR, which presents a combined workflow to process corrected Bottom-of-Atmosphere products. The combined workflow includes following optional pre-processing steps:

- Atmospheric correction with Sen2Cor
- Cirrus removal or terrain correction with Sen2Cor
- Images export in tif format
- Re-projection
- Solar angel map
- topographic correction with Minneart correction
- Scene classification export
- Enhanced cloud mask processing
- Valid data mask generation

The results of this processing step are comprised of atmospherically corrected imagery and supplementary data listed in Table 5-1.

Table 5-1: File suffix for processed products.

File suffix	content
.tif	GeoTIFF of Scene
.zip	output from Sen2Cor
_cld	cloud probability
_cloudmask	mask from derived clouds
_mask	scene, no-scene
_ncl	scene without clouds
_sol	solar azimuth and solar zenith in degree
_scl	scene classification

Additionally, to the previous mentioned pre-processing steps short filenames can be generated, to allow easier management and access to the time series data.

NAMING CONVENTION

The naming convention in phase 1 (see

Table 5-2) of the project follows the naming convention defined in the Sen2Cor user guide (Louis et al., 2016b). A detailed example follows:

Sentinel-2A_USER_PRD_MSIL2A_PDMC_20170224T103232_R065_V20151124T102342_20151124T102342_T32UPU_scl.tif

Sentinel-2A_USER_PRD_MSIL2A_PDMC_YYYYMMDDHHMMSS_R000_VyyyymmddThhmmss_YYYYMMDDTHHMMSS_Ttttt_Xxx.tif

Table 5-2: Naming convention Sentinel-2 in phase 1.

naming	explanation
Sentinel-2A	Mission ID
USER	flags the scene as user processed data
PRD_MSIL2A	File type for a product denotes the product level (Level-2)
YYYYMMDDHHMMSS	the data take sensing start time
R000	Relative Orbit number (R001 - R143)
VyyyymmddThhmmss_YYYYMMDDTHHMMSS	Applicability Time Period: appends the Validity Period Time fields (Start and Stop).
Ttttt:	Tile ID
Xxx	defines the output product consisting of following files

In contrast to the original product, the band order within the Geotiff Layer stack changed and is described in Table 5-3. The major change concerns B8 which is now located after the three visible bands.

Table 5-3: Band order for ECoLaSS Sentinel-2 data

ECoLaSS Stack	Original band number	
1	2	blue
2	3	green
3	4	red
4	8	NIR
5	5	Red705
6	6	Red740
7	7	Red788
8	8a	NIR
9	11	SWIR
10	12	SWIR

In Phase 2 the naming convention will change as shown below. The short names are defined to ensure better access to data and better management of the time series data. The short names ensure that all Sentinel images independent from the satellite mission can be subsumed under one naming convention. However, including the generation time within the time stamp is necessary as there are cases where several divided images within one granule are generated on the same date.

Sentinel-2_20150716T092053_34SGG.tif
Sentinel-2_20150716T092053_34SGG_xxx.tif

Sentinel-2 (is Sentinel-2 satellite system)
YYYYMMDDHHMMSS: generation time
Txxxxx: Tile Number field
xxx: defines the output product consisting of following files

RESULTING DATA

In phase 1 of ECoLaSS, approximately 893 GB Sentinel-2 Level-1C data volume was downloaded covering all the defined test sites, resulting in approximately 4 TB of data after the combined pre-processing workflow is applied. The resulting time series are organized according to Sentinel-2 granule ID as shown in Table 5-4.

Table 5-4: Test sites – resulting Sentinel-2 time series imagery

Name	Size (km ²)	Granules	Download Vol.	No. granules	Time interval (months)	Processed size GB
Central	24120	32TPT/31UPU	208	187	01.01.2016 – June 2017	977
France	24120	30TYP/31TCJ	118	135	01.01.2016 – June 2017	601
Belgium1	24120	31UFR/31UFS	170	212	01.01.2016 – June 2017	873
Belgium2	24120	31UES/31UER	117	152	01.01.2016 – June 2017	583
North	24120	33VVF /33VWF	480	165	01.08.2015 - 15.07.2017	199
Mali	24120	29PRP	114	45	01.01.2016 – June 2017	192
		29PTU	33	46	01.01.2016 – June 2017	199
S-Africa - Freestate	24120	35JMJ/35JNJ	133	178	01.01.2016 – June 2017	738

5.2 Pre-processing of SAR data

In order to design an optimized SAR pre-processing workflow for the ECoLaSS project and future Sentinel based Copernicus land cover mapping, we performed a state-of-the-art literature review on SAR pre-processing, analysis of existing SAR pre-processing software and performed a number of tests and benchmarking with pre-processed Sentinel-1 data. SAR time series are based on Level-1 products in Interferometric Wide swath (IW) mode and Level-1 Ground Range Detected (GRD). The IW mode is considered the main acquisition mode over land and satisfies the majority of service requirements. In addition to GRD backscatter products, first examples of short-term coherence products were processed based on SLC data and evaluated for optimized settings at two test sites. Tests on the usability of InSAR coherence for land cover mapping and resulting improvements are expected only in phase 2 after thematic classification chains have been developed.

As a result of above testing and benchmarking we have designed an optimized SAR pre-processing workflow for the ECoLaSS project which is presented in Figure 5-2.

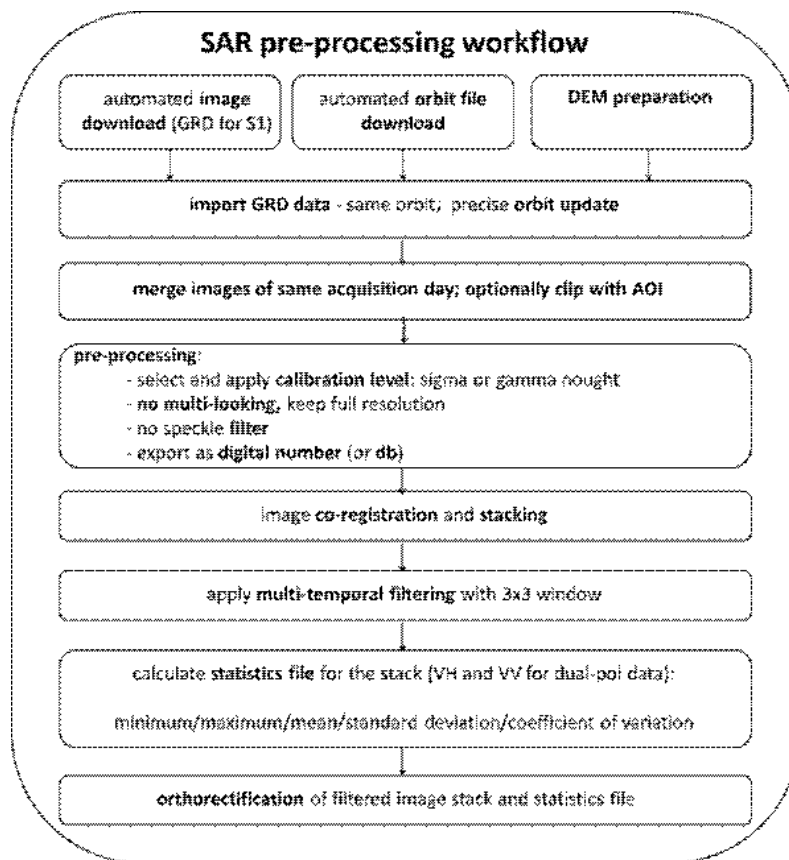


Figure 5-2: Sentinel-1 pre-processing workflow in ECoLaSS

For each Sentinel-1 orbit, the pre-processing is calculated separately as multi-temporal filtering can only be applied to images of the same orbit. In addition, a local incidence file is calculated for each orbit stack and delivered with the data. It can later be used to mask out areas with large incidence angles before classification.

SAR pre-processing steps include:

- automated SAR image download by time window,
- automated preparation of digital elevation data (SRTM4),
- automated download and update of precise orbit files,
- merge of GRD tiles from same orbit and same acquisition day,
- clip of image extent with test site,
- calculation of local incidence angle map,
- radiometric calibration,
- processing unit definition,
- radiometric terrain corrections,
- image registration in image geometry,
- adaptive image speckle filtering or multi-temporal speckle filtering,
- calculation of temporal image stack statistics (see WP34),
- orthorectification to LAEA or UTM

Table 5-5: Test sites – resulting Sentinel-1 time series imagery

SP	Name	Size (km ²)	Orbit No.	Download Vol.	No. scenes	Time interval (months)	Processed size GB
JR	Test site: Central GAMMA DN/DB; SIGMA DN/DB GAMMA DN/DB; SIGMA DN/DB	24120					
			asc117	244	201	01.01.2016 - June2017	372
			dsc168	218	199	01.01.2016 - June2017	336
JR	Test & Agri site: France	24120					
	GAMMA DN		asc30	216	66	01.01.2016 - June2017	67
	GAMMA DN		asc132	210	60	01.01.2016 - June2017	52
	GAMMA DN		dsc8	196	62	01.01.2016 - June2017	61
	GAMMA DN		dsc110	220	62	01.01.2016 - June2017	61
JR	Test & Agri site: Belgium1	24120					
	GAMMA DN		asc88	200	64	01.01.2016 - June2017	53
	GAMMA DN		asc161	199	65	01.01.2016 - June2017	55
	GAMMA DN		dsc37	225	64	01.01.2016 - June2017	58
JR	Test & Agri site: Belgium2	24120					
	GAMMA DN		dsc110	339	61	01.01.2016 - June2017	67
	GAMMA DN		asc161	see F14	64	01.01.2016 - June2017	53
DLR	Test site: North	24120					
	SIGMA DN		desc66		52	01.06.2016 - 15.07.2017	9.83
	SIGMA DN		desc168		82	01.06.2016 - 15.07.2017	21.9
	SIGMA DN		desc95		86	01.06.2016 - 15.07.2017	19.8
	SIGMA DN		asc175		83	01.06.2016 - 15.07.2017	22.6
	SIGMA DN		asc146		52	01.06.2016 - 15.07.2017	4.2
	SIGMA DN		asc102		51	01.01.2016 - 15.07.2017	11
JR	Test & Agri site: Mali	24120					
	GAMMA DN		asc45	153	45	01.01.2016 - June2017	16
	GAMMA DN		asc118	100	32	01.01.2016 - June2017	24
JR	Test & Agri site: S-Africa - Freestate	24120					
	GAMMA DN		asc116	147	41	01.01.2016 - June2017	36
				2667			1400

At the ECoLaSS test sites, a total of 1086 Sentinel-1 scenes encompassing a download volume of 2.7 TB were processed with an output data volume of 1.3 TB as shown in Table 5-5. The number and size of the imagery for the demo sites are expected to double.

6 Conclusions and Outlook

The main work of WP32 is focused in phase 1 of the ECoLaSS project, as it is a pre-requisite for work packages 33, 34 and 35, as well as for all work packages of task 4. Comprehensive testing of optical as well as SAR pre-processing methods which are relevant within the ECoLaSS project are therefore undertaken in phase 1 and pre-operational processing lines which allow pre-processing of Sentinel-1 and Sentinel-2 data streams were implemented in phase 1.

Regarding the pre-processing of Sentinel-2 optical data streams two main software packages have been compared (MAJA & Sen2Cor). In general, both software packages have advantages and drawbacks, not performing sufficiently enough to achieve a high thematic quality, content and accuracy in any subsequent information extraction process. Concerning the atmospheric correction the inter-orbit spectral stability and the consistency with other sensors show that Sen2Cor is able to achieve consistent results only if the data sets fulfil certain characteristics, e.g. presence of DDV pixels. Furthermore, both software packages produce products for cloud masking. Sen2Cor presents a generally reasonable detection of clouds and cloud shadows, but a high confusion with bright surfaces is present. To avoid the commission errors the multitemporal approach used with MAJA produces better results. In general, the cloud masks should be improved with further post-processing steps. The Sen2Cor software implementation and handling are user-friendly and it is open for public usage. MAJA might achieve better cloud masking results, but due to the licence and implementation issues the software cannot be used in commercial projects such as HRL production. We recommend that a topographic normalization should be applied in hilly to mountainous terrain for the ECoLaSS demonstration site production. The main issue with the topographic normalisation in Sen2Cor is the over-correction of south-facing slopes. The DEM with the highest spatial resolution should be used. It is therefore recommended using topographic normalisation tools which allow the user to define their own DEM. If only the SRTM 90m model is available Sen2Cor topographic normalisation also provides acceptable results.

Concerning Sentinel-1 data sets a conversion of db to DN is recommended. The standard radiometric unit of Sentinel-1 GRD data is in db. The conversion from db to DN reduces the file size by 50% and facilitates multi-temporal metric calculation from SAR image stacks. The DN based land cover classification results are slightly more accurate than db based classification results. Furthermore, we recommend using flattened gamma nought SAR backscatter data for the ECoLaSS demo site processing if data from different orbits is combined, but to eliminate areas with large incidence angles above 70°. Flattened gamma nought imagery shows best results for terrain correction and for the similarity of imagery from different orbits. When incidence angles are too steep, values are still unreliable. With sigma nought processing, imagery from different orbits cannot be used in hilly to mountainous terrain jointly because backscatter values still differ strongly among the different orbits. The SRTM4 model is not accurate enough for a full removal of terrain effects; however, it is the only freely available DEM currently available at pan-European scale. For ECoLaSS pre-processing, our analysis concludes that multi-temporal SAR filters should be applied to pre-processed gamma nought data in DN processing unit. Multi-temporal filters can be applied to the entire (or annual) image stack. Seasonal means and seasonal statistics further reduce speckle noise and should be used as input regarding SAR data classification of the HRL land cover classes. This will be analysed in WP 34 dealing with times series analysis. Whether coherence data adds any significant additional value for HR land cover classification compared to using only filtered GRD backscatter data will need to be investigated in phase two when thematic classification chains are developed. If benefits are only small, we recommend not going through the additional effort of processing SLC data and InSAR coherence. Calculating these products on the pan-European level for an entire year or more will consume a lot of time and processing power which might not be warranted. Final conclusions are expected after phase two.

It is expected that pre-processing software will be significantly improved in the near future, e.g. it is expected that atmospheric correction software such as Sen2Cor will be further developed and main issues such as related to inaccurate cloud masks are considerably improved. In phase 2 of ECoLaSS it is therefore planned to closely follow these developments, to update the current report accordingly, and to implement improvements in the pre-operational processing chains. Fusion of Sentinel-2 and Sentinel-3 time-series will be performed in phase 2, as in addition to the Sentinel-3A also the Sentinel-3B satellite imagery will be available which leads to the required temporal density of the Sentinel-3 time-series. Feedback-loops between WP32 and WP33, WP34, WP35 will guarantee continuous adaptations and improvements of the pre-processing chains to fulfil the requirements of the land cover classification and change detection workflows.

References

- Ariza, A., Ressel, C., Pfeifer, N., 2016. Evaluation of the Terrain Model Influence on the Orthorectification of Sentinel-2 Satellite Images Over Different Land Forms in Austria, in: 1st Sentinel-2 Validation Team Meeting.
- Balthazar, V., Vanacker, V., Lambin, E. F., 2012. Evaluation and parameterization of ATCOR3 topographic correction method for forest cover mapping in mountain areas. International Journal of Applied Earth Observation and Geoinformation 18, p. 436–450.
- Chen, X., Mithal, V., Vangala, S. R., Brugere, I., Boriah, S., Kumar, V., 2011. A study of time series noise reduction techniques in the context of land cover change detection. Department of Computer Science and Engineering-Technical Reports, no. TR 11-016.
- Dechoz, C., Poulain, V., Massera, S., Languille, F., Greslou, D., de Lussy, F., Gaudel, A., L'Helguen, C., Picard, C., Trémas, T., 2015. Sentinel-2 global reference image. Presented at the Proc. SPIE, p. 96430A.
- Delwart, S., Bourg, L., 2004. Radiometric calibration of MERIS. Presented at the Sensors, Systems, and Next-Generation Satellites VIII, International Society for Optics and Photonics.
- Donadieu, J., L'Helguen, C., 2016. Sentinel-2A Level-2 products description (Technical Note No. 00), PSC-NT-411-0362-CNES. CNES.
- Fletcher, K., 2012. Sentinel-2: ESA's Optical High-Resolution Mission for GMES Operational Services (European Spatial Agency SP-1322/2).
- Fougne, B., Desjardins, C., Besson, B., Bruniquel, V., Meskini, N., Nieke, J., Bouvet, M., 2016. Results from the radiometric validation of Sentinel-3 optical sensors using natural targets. Presented at the Earth Observing Systems XXI, International Society for Optics and Photonics, p. 997200.
- Frost, V., Stiles, J., Shanmugam, K. S., Holtzman, J., Smith, S., 1981. An adaptive filter for smoothing noisy radar images. Proceedings of the IEEE 69, p. 133–135.
- Gallaun, H., Schardt, M., Linser, S., 2007. Remote sensing based forest map of austria and derived environmental indicators. Proceedings of ForestSat.
- Gascon, F., Bouzinac, C., Thépaut, O., Jung, M., Francesconi, B., Louis, J., Lonjou, V., Lafrance, B., Massera, S., Gaudel-Vacaresse, A., 2017. Copernicus Sentinel-2A Calibration and Products Validation Status. Remote Sensing 9, 584.
- Gorroño, J., Fomferra, N., Peters, M., Gascon, F., Underwood, C. I., Fox, N. P., Kirches, G., Brockmann, C., 2017. A Radiometric Uncertainty Tool for the Sentinel-2 Mission. Remote Sensing 9, p. 178.
- Hagolle, O., Huc, M., Pascual, D. V., Dedieu, G., 2010. A multi-temporal method for cloud detection, applied to FORMOSAT-2, VENµS, LANDSAT and Sentinel-2 images. Remote Sensing of Environment 114, p. 1747–1755.
- Hamilton, J. D., 1994. Time series analysis. Princeton University Press Princeton.
- Hantson, S., Chuvieco, E., 2011. Evaluation of different topographic correction methods for Landsat imagery. International Journal of Applied Earth Observation and Geoinformation 13, p. 691–700.
- Harvey, A. C., 1990. Forecasting, structural time series models and the Kalman filter. Cambridge -- University Press.
- Hollstein, A., Segl, K., Guanter, L., Brell, M., Enesco, M., 2016. Ready-to-Use Methods for the Detection of Clouds, Cirrus, Snow, Shadow, Water and Clear Sky Pixels in Sentinel-2 MSI Images. Remote Sensing 8, p. 666.
- Home, O.D.H.N., List, C.D., NPP, N.P.P., Questions, D.P., Curation, D., Visualizer, S. M., Checker, L.-W., 2013. LEDAPS calibration, reflectance, atmospheric correction preprocessing code, version 2.
- Hurvich, C. M., Tsai, C.-L., 1989. Regression and time series model selection in small samples. Biometrika 76, p. 297–307.
- Inglaada, J., Giros, A., 2004. On the possibility of automatic multisensor image registration. IEEE Transactions on Geoscience and Remote Sensing 42, p. 2104–2120.
- Irish, R. R., Barker, J. L., Goward, S.N., Arvidson, T., 2006b. Characterization of the Landsat-7 ETM+ automated cloud-cover assessment (ACCA) algorithm. Photogrammetric Engineering & Remote Sensing 72, 1179–1188.

- Jin, S., Homer, C., Yang, L., Xian, G., Fry, J., Danielson, P., Townsend, P. A., 2013. Automated cloud and shadow detection and filling using two-date Landsat imagery in the USA. International Journal of Remote Sensing 34, 1540–1560.
- Kääb, A., Winsvold, S.H., Altena, B., Nuth, C., Nagler, T., Wuite, J., 2016. Glacier Remote Sensing Using Sentinel-2. Part I: Radiometric and Geometric Performance, and Application to Ice Velocity. Remote Sensing 8, p. 598.
- Kane, V. R., Gillespie, A. R., McGaughey, R., Lutz, J. A., Ceder, K., Franklin, J. F., 2008. Interpretation and topographic compensation of conifer canopy self-shadowing. Remote Sensing of Environment 112, p. 3820–3832.
- Karlsson, K.-G., Johansson, E., 2014. Multi-Sensor calibration studies of AVHRR-heritage channel radiances using the simultaneous nadir observation approach. Remote Sensing 6, p. 1845–1862.
- Kuan, D. T., Sawchuk, A. A., Strand, T. C., Chavel, P., 1985. Adaptive noise smoothing filter for images with signal-dependent noise. IEEE transactions on pattern analysis and machine intelligence p. 165–177.
- Languille, F., Déchoz, C., Gaudel, A., Greslou, D., De Lussy, F., Trémas, T., Poulain, V., 2015. Sentinel-2 geometric image quality commissioning: First results. Presented at the Proc. SPIE, p. 964306.
- Lee, J.-S., 1981. Refined filtering of image noise using local statistics. Computer graphics and image processing 15, p. 380–389.
- Lee, J.-S., 1980. Digital image enhancement and noise filtering by use of local statistics. IEEE transactions on pattern analysis and machine intelligence, p. 165–168.
- Lee, J.-S., Jurkevich, L., Dewaele, P., Wambacq, P., Oosterlinck, A., 1994. Speckle filtering of synthetic aperture radar images: A review. Remote Sensing Reviews 8, p. 313–340.
- Li, S., Ganguly, S., Dungan, J. L., Wang, W., Nemani, R. R., 2017. Sentinel-2 MSI radiometric characterization and cross-calibration with Landsat-8 OLI. Adv. Remote Sens 6, p. 147.
- Lonjou, V., Desjardins, C., Hagolle, O., Petrucci, B., Tremas, T., Dejus, M., Makarau, A., Auer, S., 2016. MACCS-ATCOR joint algorithm (MAJA). Presented at the Remote Sensing of Clouds and the Atmosphere XXI, International Society for Optics and Photonics, p. 1000107.
- Lopes, A., Nezry, E., Touzi, R., Laur, H., 1990. Maximum a posteriori speckle filtering and first order texture models in SAR images. Presented at the Geoscience and Remote Sensing Symposium, 1990. IGARSS'90.'Remote Sensing Science for the Nineties'., 10th Annual International, IEEE, p. 2409–2412.
- Louis, J., Debaecker, V., Main-Knorn, M., Bieniarz, J., Mueller-Wilm, U., Cadau, E., Gascon, F., Pflug, Bringfried, 2016a. Sentinel-2 Sen2Cor: Level-2 Processor for Users. Presented at the Proceedings Living Planet Symposium 2016, Spacebooks Online, p. 1–8.
- Louis, J., Debaecker, V., Pflug, B., Main-Knorn, M., Bieniarz, J., Mueller-Wilm, U., Cadau, E., Gascon, F., 2016c. Sentinel-2 Level-2 Processor Sen2Cor.
- Main-Knorn, M., Pflug, B., Debaecker, V., Louis, J., 2015. Calibration and validation plan for the L2a processor and products of the Sentinel-2 mission. The International Archives of Photogrammetry, Remote Sensing and Spatial Information Sciences 40, p.1249.
- Meer, P., Park, R.-H., Cho, K., 1994. Multiresolution adaptive image smoothing. CVGIP: Graphical Models and Image Processing 56, 140–148.
- Montgomery, D. C., Jennings, C. L., Kulahci, M., 2015. Introduction to time series analysis and forecasting. John Wiley & Sons.
- Moreno, Á., García-Haro, F.J., Martínez, B., Gilabert, M. A., 2014. Noise reduction and gap filling of fapar time series using an adapted local regression filter. Remote Sensing 6, 8238–8260.
- Müller-Wilm, U., Louis, J., Richter, R., Gascon, F., Nieuwpoort, M., 2013. Sentinel-2 level 2A prototype processor: Architecture, algorithms and first results. Presented at the Proceedings of the 2013 ESA Living Planet Symposium, Edinburgh, UK, p. 9–13.
- Nieke, J., Mavrocordatos, C., Donlon, C., Berruti, B., Garnier, T., Riti, J., Delclaud, Y., 2015. Ocean and Land Color Imager on Sentinel-3. Optical Payloads for Space Missions 223.

- Pandžić, M., Mihajlović, D., Pandžić, J., Pfeifer, N., 2016. Assessment Of The Geometric Quality Of Sentinel-2 Data. International Archives of the Photogrammetry, Remote Sensing & Spatial Information Sciences 41.
- Park, S.-H., Jung, H.-S., Choi, J., Jeon, S., 2017. A quantitative method to evaluate the performance of topographic correction models used to improve land cover identification. Advances in Space Research 60, p. 1488–1503.
- Pepe, A., Yang, Y., Manzo, M., & Lanari, R. (2015). Improved EMCF-SBAS processing chain based on advanced techniques for the noise-filtering and selection of small baseline multi-look DInSAR interferograms. IEEE Transactions on Geoscience and Remote Sensing, 53(8), p. 4394-4417.
- Petrucci, B., Huc, M., Feuvrier, T., Ruffel, C., Hagolle, O., Lonjou, V., Desjardins, C., 2015. MACCS: Multi-Mission Atmospheric Correction and Cloud Screening tool for high-frequency revisit data processing. Presented at the Image and Signal Processing for Remote Sensing XXI, International Society for Optics and Photonics, p. 964307.
- Pflug, B., Main-Knorn, M., Bieniarz, J., Debaecker, V., Louis, J., 2016. Early Validation of Sentinel-2 Level-2 Processor and Products. Presented at the Proceedings of ‘Living Planet Symposium 2016,’ Spacebooks Online, p. 1–6.
- Quegan, S., Le Toan, T., Yu, J. J., Ribbes, F., Flouri, N., 2000. Multitemporal ERS SAR analysis applied to forest mapping. IEEE Transactions on Geoscience and Remote Sensing 38, p. 741–753.
- Richter, R., Schläpfer, D., 2011. Atmospheric/topographic correction for airborne imagery. ATCOR-4 user guide.
- Richter, R., Schläpfer, D., Müller, A., 2006. An automatic atmospheric correction algorithm for visible/NIR imagery. International Journal of Remote Sensing 27, p. 2077–2085.
- Richter, R., Wang, X., Bachmann, M., Schläpfer, D., 2011. Correction of cirrus effects in Sentinel-2 type of imagery. International Journal of Remote Sensing 32, p. 2931–2941.
- Rouquié, B., Hagolle, O., Bréon, F.-M., Boucher, O., Desjardins, C., Rémy, S., 2017. Using Copernicus Atmosphere Monitoring Service Products to Constrain the Aerosol Type in the Atmospheric Correction Processor MAJA. Remote Sensing 9, p. 1230.
- Santer, R., 2006. Calibration Validation Requirements Consolidation.
- Schubert, A., Miranda, N., Geudtner, D., Small, D., 2017. Sentinel-1A/B Combined Product Geolocation Accuracy. Remote Sensing 9, p. 607.
- Singh, M., Mishra, V., Thakur, N., Sharma, J. D., 2015. Expansion of empirical-statistical based topographic correction algorithm for reflectance modeling on Himalayan terrain using AWIFS and MODIS sensor. Journal of the Indian Society of Remote Sensing 43, p. 379–393.
- Sola, I., González-Audicana, M., Álvarez-Mozos, J., 2016. Multi-criteria evaluation of topographic correction methods. Remote Sensing of Environment 184, p. 247–262.
- Spaans, K., Hooper, A., 2016. InSAR processing for volcano monitoring and other near-real time applications. Journal of Geophysical Research: Solid Earth 121, p. 2947–2960.
- Tamm, T., Zalite, K., Voormansik, K., Talgre, L., 2016. Relating Sentinel-1 Interferometric Coherence to Mowing Events on Grasslands. Remote Sensing 8, p. 802.
- Teillet, P., Guindon, B., Goodenough, D., 1982. On the slope-aspect correction of multispectral scanner data. Canadian Journal of Remote Sensing 8, p. 84–106.
- Touzi, R., Lopes, A., Bruniquel, J., Vachon, P.W., 1999. Coherence estimation for SAR imagery. IEEE Transactions on Geoscience and Remote Sensing 37, p. 135–149.
- Udroiu, C., Grosu, A., Popescu, R., Nicola, L., Manda, R., Savinaud, M., Bellemans, N., Bontemps, S., 2017. Sentinel-2 Agriculture Software User Manual.
- Verbesselt, J., Hyndman, R., Newnham, G., Culvenor, D., 2010. Detecting trend and seasonal changes in satellite image time series. Remote Sensing of Environment 114, p. 106–115.
- Vincini, M., Frazzi, E., 2003. Multitemporal evaluation of topographic normalization methods on deciduous forest TM data. IEEE Transactions on Geoscience and Remote Sensing 41, p. 2586–2590.
- Warner, T. A., Foody, G.M., Nellis, M. D., 2009. The SAGE handbook of remote sensing. Sage Publications.
- Wulder, M., Franklin, S. E., 2012. Remote sensing of forest environments: concepts and case studies. Springer Science & Business Media.

- Zalite, K., Voormansik, K., Praks, J., Antropov, O., Noorma, M., 2014. Towards detecting mowing of agricultural grasslands from multi-temporal COSMO-SkyMed data. Presented at the Geoscience and Remote Sensing Symposium (IGARSS), 2014 IEEE International, IEEE, p. 5076–5079.
- Zebker, H.A., Villasenor, J., 1992. Decorrelation in interferometric radar echoes. *IEEE Transactions On Geoscience and Remote Sensing* 30, 950–959.
- Zhu, Z., Wang, S., Woodcock, C. E., 2015b. Improvement and expansion of the Fmask algorithm: cloud, cloud shadow, and snow detection for Landsats 4–7, 8, and Sentinel-2 images. *Remote Sensing of Environment* 159, p. 269–277.
- Zhu, Z., Woodcock, C. E., 2012b. Object-based cloud and cloud shadow detection in Landsat imagery. *Remote Sensing of Environment* 118, p. 83–94.

Internet sources

- CNES (2018) Logiciels Gratuits: <https://logiciels.cnes.fr/en/license/57/144ESA>
- Sentinel Technical Guides (2017): <https://sentinel.esa.int/web/sentinel/sentinel-technical-guides>, (accessed 20.01.18).
- GEOS (2017): <https://eocalibration.wordpress.com/>, (accessed 23.01.18).
- MAJA processor (2017): <https://logiciels.cnes.fr/en/content/maja>, (accessed 20.01.18).
- Sen2agri Software User Manual (2017): <http://www.esa-sen2agri.org/wp-content/uploads/resources/technical-documents/Sen2-Agri-Software-User-Manual-2.4.pdf>, (accessed 25.01.18).
- VITO (2012): http://calvalportal.ceos.org/c/document_library/get_file?uuid=7aa5e7dd-ffd1-4400-8c70-f7c8c68dc168&groupId=10136, (accessed 23.01.18).
- CNES, (2018). MAJA | Logiciels Gratuits. URL <https://logiciels.cnes.fr/en/license/57/144> (accessed 25.01.18).